Thesis

Submitted in Partial Fulfillment of the Requirements for the Degree of

Doctor of Sciences in Physics

By:

Elwardi BITAM

Title:

Configurations Study of

Parabolic Trough Collectors Field for

Optimizing Heat Transfer Fluids Outlet Temperature

Specialty: Renewable Energies/Physics.

Graduated on 18 /04 / 2019

Examination Committee:

President:	BOUGOUL Saadi	Pr	University of Batna 1
Supervisors:	BENMOUSSA Hocine	Pr	University of Batna 2
	DEMAGH Yassine	Dr	University of Batna 2
Examiners :	ADOUANE Belkacem	Pr	University of Batna 1
	DJOUIMAA Sihem	Pr	University of Batna 1
	BORDJA Lyes	Dr	University of Oum El Bouaghi

The dedication of this work is firstly to my parents and my family, secondly to everyone who taught me and thirdly to my friends.

Elwardi BITAM

ACKNOWLEDGMENTS

ملخص

من بين الخيارات المتعددة لخفض سعر تقنية حوض تجميع الطاقة الشمسية ذو القطع المكافئ، تصميمات لاقط (مستقبل) جديد تم اقتراحها من طرف بعض المؤلفين لتحسين الآداءات العامة وتحقيق اعلى كفاءة حرارية للأنبوب الماص. مؤخرا، أنبوب ماص جديد تم اقتراحه من اجل التوزيع الحسن لأشعة الشمس المركزة على سطحه الخارجي بدون التأثير على عامل الاعتراض؛ الماص المقترح له شكل جيبي مقارنة بالشكل المستقيم للسابق.

اقتراح قانون حساب الموائع الديناميكية باستخدام فلوانت المبني على معادلات الاضطراب من اجل تحري تحسن مكون التحول الحراري عبر الانبوب الملتوي على شكل S المصمم جديدا للمجمع الحراري كعنصر من وحدة حوض تجميع الطاقة الشمسية ذو القطع المكافئ. نتيجة للشكل الجديد للأنبوب الماص، كثافة التوزيع الحراري على السطح الخارجي تتغير في الاتجاهين الطولي والمحيط العرضي في حين كانت تتغير فقط في اتجاه المحيط العرضي على الماص السابق. تم تحري ومقارنة السلوك الهيدروحراري للأنبوب الماص الجديد لنظام الطاقة الشمسية ذو القطع المكافئ بالنظام التقليدي باستخدام الزيت الصناعي كمائع تحويل حراري.

مصداقية النموذج تم اختبارها عن طريق مقارنة نتائج المحاكات مع المعطيات التجريبية المتوفرة عن الانابيب الجيبية للتبادلات. تحليل جريان مائع التحول الحراري عبر الانبوب الماص الجديد يبين نشأة دوامات عند التقوسات. لقد تم استنتاج انه بدون أي جهاز إضافي، انه من المتوقع ان يرتفع متوسط رقم نيوسالت من 45 ٪ الى 63 ٪، في حين يرتفع معامل الاحتكاك بأقل من 40,8 ٪، هذا يؤدي الى قيمة قصوى لمعيار تقييم الأداء في حدود 135 ٪، الفارق الأقصى في درجات الحرارة للمحيط العرضي للأنبوب الماص تهوي لأقل من 35 °م و هذا لجل مجال سرعات التدفق ويفترض ان تؤدي الى تقليص الاجهادات والحرارة الضائعة.

بالإضافة، التصميم الجديد للماص، قد يقلص حجم حوض تجميع الطاقة الشمسية ذو القطع المكافئ بنسبة 31 ٪ بحيث يبقى مردوده مكافئ لمردود الأنبوب الماص المستقيم بحجمه الأصلي.

الكلمات الافتتاحية: الماص الجيبي/الملتوي على شكل S، الاداءات الحرارية المحسنة، التوزيع الثلاثي الابعاد لكثافة التدفق الحراري، دوامة دين، تقليص الحجم.

Résumé

Parmis les différentes options pour réduire les coûts d'investissement relatifs à la technologie des concentrateurs solaires cylindro-paraboliques, l'amélioration des performances thermiques des absorbeurs solaires s'avère être une piste intéressante. De nouvelles conceptions et idées (Design) sont proposées régulièrement par les scientifics afin d'atteindre un seuil élevé de la conversion photo-thermique. Récemment, une nouvelle étude proposée une nouvelle forme pour les tubes absorbeurs afin d'homogénéiser le rayonnement solaire concentré sur sa face externe sans pour autant affecter le facteur d'interception ; l'absorbeur proposé possède une forme sinusoïdale, concept complètement différent des absorbeurs classiques avec leurs formes droites (rectilignes).

Le model de turbulence SST k–ω du code de calcul Fluent 6.3 a été utilisé dans cette étude pour mener un travail d'investigation assez détaillé sur l'amélioration potentielle qu'offrirait cet absorbeur nouvellement conçu muni d'un tube S-courbé (sinusoïdale) sur les échanges d'énergies internes. En conséquence de la nouvelle forme du tube absorbeur, la distribution de la densité de flux solaire sur la face extérieure varie dans la direction longitudinale et la direction azimutale en même temps (d'un caractère 3D); tandis qu'elle ne varie que dans la direction azimutale sur les absorbeurs classiques droits (d'un caractère 2D).

La validation du modèle, des simulations et des résultats numériques a été établie par comparaison avec des données expérimentales de la littérature disponibles pour des échangeurs de chaleur classique à tube sinusoïdal. L'analyse des écoulements de fluide à travers le nouvel tube absorbeur a démontré l'émergence de vortexes au niveau des courbures de la sinusoïde. Sur la base des résultats obtenus des simulations (validées) une étude comparative a été établie entre les deux absorbeurs (classique et nouvel) utilisant l'huile synthétique (Syltherm 800) comme fluide de travail. Il a été établi que sans aucun dispositif additionnel, le Nusselt moyen augmenterai de 45% à 63% pour le nouvel absorbeur solaire, tandis que le coefficient de frottement n'augmenterait que de 40.8%, ce qui conduit à une valeur maximale du critère d'évaluation de performance autour de 135%. La différence de température maximale (sur la face externe du tube) dans la direction azimutale (circonférence) allait diminuer au-dessous de 35 K pour pratiquement toute la plage des débits massiques, ce qui laisse croire que les contraintes thermique et les pertes de chaleur vont être réduites considérablement.

En plus de tous les points positifs énumérés ci-dessus, avec cette nouvelle génération d'absorbeurs on espère arriver à une réduction importante dans les tailles des modules CCP, jusqu'à 31% en moins dans la longueur dans des conditions précises, pour atteindre les mêmes performances qu'offriraient les absorbeurs classiques.

Mots clés : Absorbeur S-courbé/sinusoïdal, amélioration des performances thermiques, distribution 3D de la densité de flux chaleur, Vortex de Dean, réduction de taille.

Abstract

Amongst different options to drive down cost of parabolic trough collector (PTC) technology, new receiver designs have been proposed by some authors to improve overall performances and achieve higher thermal efficiency of the absorber pipe. Recently, a novel absorber tube has been proposed to homogenise the concentrated solar radiation on its outer surface without affecting the interception factor; the proposed absorber would have a sinusoidal shape with regard to the straight shape of the former.

A Computational Fluid Dynamics (CFD) based on SST k–ω turbulent model is proposed to investigate the heat transfer potential enhancement within a newly designed S-curved tube as heat collection element (HCE) of the PTC unit. As a consequence of the novel shape of the absorber pipe, the heat density distribution on the outer surface varies in both longitudinal and azimuthal directions while it is varying only in the azimuthal direction on the former. The thermo-hydraulic behavior of the novel PTC absorber pipe is investigated and compared with the conventional one, using synthetic oil as heat transfer fluid (HTF).

The validity of the model has been tested by comparing the simulation results with available experimental data for the sinusoidal pipe exchangers. The analysis of the HTF flow through the novel PTC absorber pipe showed the emergence of vortices at bends. It is established that, without any additional devices, the mean Nusselt number is expected to increase by 45% to 63%, while the friction coefficient increases by less than 40.8%, which lead to a maximum performance evaluation criteria about 135%. The maximum circumferential temperature difference of the absorber pipe decreases below 35 K for almost all the range of the mass flow rates and should result in the reduction of thermal stresses and heat losses.

In addition, with the newly absorber design, the PTC unit size could be reduced by 31%, keeping the same power of the solar plant as in the case of using full size conventional straight and smooth tube (CSST) absorber.

Keywords: S-curved/sinusoidal absorber, Enhanced thermal performances, 3D Heat flux density distribution, Dean Vortex, Size reduction.

Table of contents

Nomenclature

Roman Letters

A [m, m²]	Amplitude or area	$L[m]$	Absorber Straight length
$c_p[J/kgK]$	Specific heat	$p[Pa]$	Pressure
$D[m]$	Diameter	$Q[W]$	Mean heat transfer rate
ΔT	Temperature gradient of the absorber	$q_{sun}[Wm^{-2}]$	Direct Solar insolation
E_f	Pressure drop penalty	$q[Wm^{-2}]$	Heat flux density on the outer face of the absorber
E_{Nu}	Heat transfer performance	$q_w''[Wm^{-2}]$	Inner averaged heat flux
F_1, F_2	Blending function	$R_{curv}[m]$	Curvature radius
f	Friction factor, or focal length [m]	$S_T[Wm^{-3}]$	Energy source term
V	HTF velocity magnitude	St	Stanton number
$h[Wm^{-2}K^{-1}]$	Convective coefficient	T_{mf}	Arithmetic mean temperatures
$k[m^2s^{-2}]$	Turbulence kinetic energy	$\bar{T}[K], T^*$	Bulk and dimensionless temperature of the Fluid
$l_t[m]$	Turbulent length scale	$\bar{T}_w[K]$	Mean temperature of the absorber inner face

$\dot{m}\left[kgs^{-1}\right]$	Mass flow rate	$V_w\left[m^3\right]$	Volume of the pipe wall
Nu^*	Normalised mean Nusselt number	u_{in}	Inlet velocity
$\overline{Nu_\varphi}$	Circumferential mean Nusselt number	$V^* = V/u_{in}$	Normalised velocity
L_r	Collector aperture	$y'(z), y''(z)$	First and second derivatives of y (z)
$z_{cs}[m]$	z-coordinate of the cross-section	$z_a[m]$	Length of the absorber
PTC	Parabolic Trough Collector	SEGS	Parabolic Trough Solar Energy Generating System
CSP	Concentrating Solar Power	HCE	Heat Collection Element
CFD	Computational Fluid Dynamics	CSST	Conventional Straight and Smooth Tube
SST	Shear-Stress-Transport	HTF	Heat Transfer Fluid
UDF	User Define Function	AR	Aniti-Reflective
NUHF	Non-Uniform Heat Flux	UHF	Uniform Heat Flux
FVM	Finte Volume Method	MCRT	Monte Carlo Ray Trace

Greek Letters   **Subscripts**

α	Absorptance	a	Absorber pipe
ε	Emittance	b	Bulk

$\delta = D/2R_{curv}$	Curvature ratio	amb	Ambient
$\varphi\left[°\right]$	Azimuthal angle	cr	Critical
$\lambda\left[m, Wm^{-1}K^{-1}\right]$	Periodicity length or thermal Conductivity	cs	Cross-section
$\tau\left[\ \right],\left[Pa\right]$	Transmittance or wall shear stress	f	Film
mf	Mean fluid	g	Glass
in and out	Pipe inlet and outlet	i and o	Inner and outer faces of the absorber
w	Pipe wall	e	External
$2\theta_{sun}$	Finite size of the sun	φ_{rim}	Rim angle
$\omega\left[s^{-1}\right]$	Specific dissipation rate		

List of figures

General introduction

In modern life, the sun's rays energy can be converted and used as different thermal applications including water heating, space heating and cooling, industrial process heat and power systems.

Different technologies have been involved to serve the thermal applications, classified as concentrating and non-concentrating systems. Concentrating systems (including PTC, linear Fresnel, central receiver and parabolic dish technologies) designed mainly to produce steam; the steam is used to drive a turbine coupled with an electricity generator to produce electricity. The PTC plant is the most used concentrating technology system to convert Sun's rays to thermo-dynamic energy to produce electricity.

The PTC plant efficiency can be affected by intrinsic (controllable) parameters including the optical efficiency of the PTC, heat transfer fluid thermo-physical properties…etc. Moreover, environmental and geographical parameters.

The PTC consists of parabola (mirrors), receiver tube, thermal fluid, structure and tracking system. Although the alignment of the receiver, the parabola optical parameters, rim angle and tracking system accuracy have been studied thoroughly; in the last two decades, numerical and experimental works on the HCE have been intensified. Introducing inserts inside the receiver tube with different configurations, proposing novel selective coating material as well as developing Mont Carlo Ray-Trace (MCRT) method for better understanding the optical model are studied.

Introducing inserts inside the receiver tube enhanced the heat transfer rate mainly by improving the mixing of the heat transfer fluid with the price of increasing pressure drop considerably. However, the thermal efficiency of a receiver with inserts relatively improved compared to CSST receiver.

Recently as discussed in **chapter 1**, a novel configuration proposed by **Demagh et al. 2015 [61]** to be used as HCE in the PTC system; the proposed tube configuration has an S-curved shape and would not include any additional parts (no inserts). The literature review

shows that no study has been conducted on thermo-hydraulic behavior of an S-curved tube as a heat collector element of the PTC unit.

Objectives of this thesis

Considering the actual state-of-the-art in modelling parabolic trough solar collectors, a receiver tube with inserts is characterized by excessive pressure drop and present relatively some challenges to manufacture compared to CSST receiver. The S-curved tube may be an alternative to improve heat transfer rate by the induced secondary flow due to waviness shape and less pressure drop favorized by keeping the inside diameter smooth (no inserts).

This thesis aims at:

- Using user define function (UDF) to manifest the heat flux distribution on the outer surface of the novel S-curved tube and compare it with heat flux distribution on the outer surface of the CSST.
- Studying the fluid flow and heat transfer in the novel parabolic trough collector to quantify pressure drop and heat transfer enhancement.
- Finding a similitude relation between the novel S-curved receiver tube and the CSST receiver in terms of efficiency and size.
- Replacing the CSST HCE of the typical SEGS LS2 plant by the novel S-curved tube and studying its new configuration in order to optimizing the heat transfer fluid outlet temperature and reducing its size.

Research approach

Several research works have been conducted to study the heat transfer and fluid flow in curved pipes as a practical engineering application. Potential applications of curved geometries in industrial processes include helical coil, bend tube, serpentine tube, spiral, and twisted tubes. However, limited studies have investigated turbulent flow in longitudinally curved pipes. As cited in **chapter 2**, **Abou-Arab et al. 1991 [10]** and **Yang et al. 2002 [11]** proposed correlations for friction factor of water flowing through a sinusoidal circular pipe.

Through literature the SST k–ω turbulent model is suited for turbulent flow where high secondary flow involved, the model helps to catch fluid detachment near the wall and predicts well Dean vortices. Similar configuration to that studied by **Abou-Arab et al. 1991 [10]** is used in present study for validation purpose, the computational domain is generated and meshed by Gambit 2.2.30 by sweeping the meshed cross-section of the tube using quadrilateral elements with a structured mesh into the absorber pipe wall and an unstructured (Quad/Tri) non-uniform grids within it to insure $y^+ < 1$ condition. The transport equations solved by Fluent 6.3 using coupled method, differentiated equations solved by second order scheme and the SIMPLE algorithm is performed for solving the pressure-velocity linked equation.

Research approaches adopted in this study can be summarised in the following points:

- Validate the numerical model using correlations of Abou-Arab et al. 1991 [10] and Yang et al. 2002 [11] for laboratory scale S-curved tube.
- After validating the model, the same model is used to simulate the novel PTC S-curved tube.
- The heat flux on the outer surface of the tube calculated by UDF. The vacuumed annulus between glass and absorber considers only radiative heat flux, the glass was omitted in this study but its properties were taken into account in the optical model.
- Obtained results from CFD had been processed and treated by Excel to be presented as graphs using Origin. Therefore, the streamlines of vortices presented using Tecplot.

Thesis layout

General introduction comprises the aims, the research approach and the layout of this project.

Chapter one presents a literature review of thermal applications of solar energy, solar power plant technology, proposed receiver tubes configuration and development made in terms of selective material coating as well as developed experimental, numerical and optical models analyzing thermo-dynamic phenomena through PTC HCE.

Chapter two presents brief review on curved tubes applications, studied domain identification, numerical and optical models as well as involved mathematical equations.

Chapter three presents models validation and obtained results. In addition to their analysis and discussions.

Chapter four presents similitude relation in terms of thermal efficiency between S-curved tube with reduced size and CSST with full size.

General conclusion presents the different conclusions from this work and recommendations for continuing it on the future.

Chapter 1:Literature Review

Introduction

In this chapter, the main existing solar energy collectors for thermal applications including water heating, space heating and cooling, industrial process heat and power systems are presented. Furthermore, the power systems known by solar concentrating technology involving linear Fresnel collector, solar tower, parabolic dishes and parabolic trough are particularly discussed.

Through the brief review on existing and planned concentrating solar power (CSP) plants presented hereafter, the parabolic trough plants are the most used and sited well to be used thoroughly in the future. The parabolic trough collector considered as the backbone of the parabolic trough plant. The main elements of the parabolic trough plant are highlighted especially those forming the parabolic trough collector unit (receiver tube, structure and mirrors and thermal fluid) and thermal storage facility even if it is in some cases optional.

The parabolic trough collector have been investigated thoroughly experimentally and numerically aiming to improve its thermal and optical performances. The heat transfer fluid and parabola have had the same attention as much as the receiver tube. Nevertheless, this chapter reviews basically, subjects related to the receiver tube, involving heat transfer enhancement efforts by introducing inserts, selective coating evolution and introducing the fascinating MCRT method.

As mentioned in the general introduction, the main objective of the thesis is the investigation of the thermo-dynamic behavior of the newly designed S-curved tube, thus an exhaustive review on the existing works dealing with the receiver tube including involved modelling techniques and development through the history are discussed.

1.1. Solar energy collectors

The solar radiation energy is transformed through collectors to an internal energy carried out by the HTF. The energy of HTF can be then used directly as hot water or for other applications. Solar collectors can be classified as non-concentrating (stationary) or

concentrating (**Kalogirou 2004 [1]**). The main difference is, the stationary collectors have the same area for intercepting and for absorbing solar radiation, whereas the concentrating collectors have much higher concentration ratio up to 1500, which is basically the ratio of intercepting area to receiving area. Solar collectors available in the market are summarized in the table 1.1.

Table 1. 1 : Solar energy collectors **[1]**.

Motion	Collector type	Absorber type	Concentration ratio	Indicative temperature ratio (°C)
Stationary	Flat plate collector (FPC)	Flat	1	30-80
	Evacuated tube collector (ETC)	Flat	1	50-200
	Compound parabolic collector (CPC)	Tubular	1-5	60-240
Single-axis tracking	Linear Fresnel collector (LFC)	Tubular	10-40	60-250
	Parabolic trough collector (PTC)	Tubular	15-45	60-300
	Cylindrical trough collector (CTC)	Tubular	10-50	60-300
Two-axes tracking	Parabolic dish reflector (PDR)	Point	100-1000	100-500
	Heliostat field collector (HFC)	Point	100-1500	150-2000

1.2. Applications of solar energy

As can be seen from **(Kalogirou 2004 [1]; Jebasingh and Joselin 2016 [2])**, solar energy has wide range of applications and it offers many commodities for modern life. Typical applications of the various type of collectors include **[1]**:

- Solar water heating, which comprise thermosyphon, integrated collector storage, direct and indirect systems and air systems.
- Space heating and cooling, which comprise, space heating and service hot water, air and water systems, heat pumps and refrigeration.
- Industrial process heat, which comprise air and water Systems, steam generation systems and desalination.

- Thermal power systems, which comprise the parabolic trough, power tower and dish systems, solar furnaces, and chemistry applications.

1.3. Solar concentrating technology

Solar concentrating systems can be classified according to the shape of their principal components especially reflectors thus the way they focus the sun' rays and ultimately the whole process involved from extracting energy to its conversion to electricity or other forms. Therefore, solar concentrating technology can be subdivided into four categories as shown in the figure 1.1.

1.3.1. Parabolic troughs

The parabolic trough composed of a reflector with trough shape and a solar receiver. The reflector designed to reflect up to 90% of the intercepted sun' rays, the absorber tube with selective coating is designed to absorb maximum of radiation and limit its emitting infrared radiation. Both reflector and receiver move in tandem in single axis tracking following the sun' path form its raise to its set. Parabolic trough in most cases uses synthetic oil as heat transfer fluid. Most current concentrating solar power (CSP) plants are parabolic troughs [3].

1.3.2. Linear Fresnel reflectors

Linear Fresnel reflector has flat or slightly curved shape and fixed receiver tube placed at the center of the system. New design known as compact linear Fresnel reflectors can use two receiver tubes for each row of mirrors, thus producing the same amount of energy with reduced plant size and less cost. The linear Fresnel reflectors have less investment cost; generate direct steam easier than PTC, so exchangers and heat transfer fluids might be avoided. However, it is less efficient for electricity production and difficult to incorporate storage capacity [3].

1.3.3. Solar towers

A central receiver fixed on the top of tower, receives the sun' rays, reflected by small reflectors called heliostats thus heating the heat transfer fluid. The solar tower can reach very

high temperature and producing electricity more efficiently. The concept of solar towers is more flexible than previous systems [3].

1.3.4. Parabolic dishes

The sun' rays concentrated by the reflector onto focal point supported above the center of dish. Parabolic dishes are considered as the highest in terms of solar to electric conversion performance of any concentrating solar power systems. Compact size, no need for cooling water, parabolic dishes are well placed to compute with any solar energy system. Hundreds or thousands of parabolic dishes have to be installed to build a large-scale plant in terms of energy equivalent to other typical concentrating solar power [3].
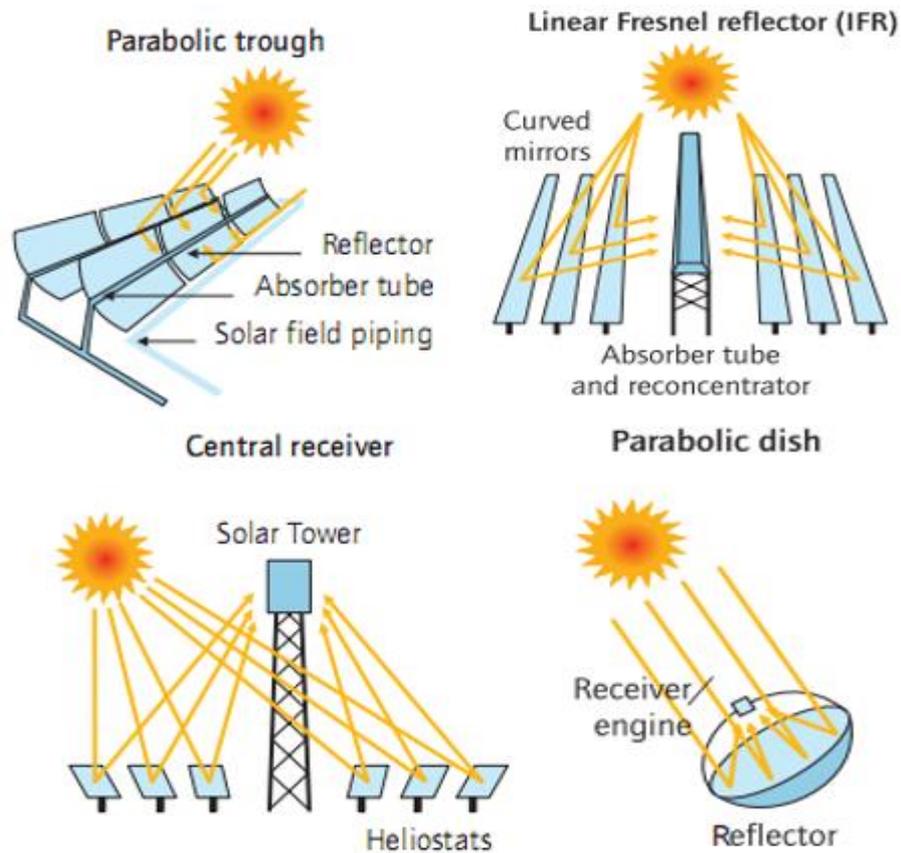
Figure 1.1 : Typical solar concentrator technologies [3].

1.4. Concentrating solar power (CSP) plants review

The first practical concentrating solar power (CSP) plant is a parabolic trough plant for powering an irrigation system, which was successfully completed by Frank Shuman in Meadi, Egypt, in 1913. It is waited until 1965, to build the first solar power plant in Sant'Ilario in Italy. The well-known nine parabolic trough Solar Energy Generating Systems (SEGS), built between 1984 and 1990 in California, USA, remain the largest solar energy generating facility in the world today, with 354 MWe of installed capacity. In Seville, Spain, the first commercial solar tower PS10 in the country with a capacity of 11 MWe, was accomplished in 2007 (**Isabel et al. 2011 [4]**).

Hank Price et al. 2002 [5] presented barriers on the way of developing concentrating solar power, they described also the efforts made for building the fantastic SEGS plants. The description of new technologies in developing and improving reflectors, receivers and power cycle have been presented thoroughly.

Until 2011, 96.3% of operational concentrating solar power are parabolic trough technology with up to 29 plants in operation and around 1220 MW$_e$ of installed power in the world (**Isabel et al. 2011 [4]).**

A review on CSP plants, the world irradiation distribution and its estimation, comparison between different CSP technology and some development in the field of CSP are presented by **Zhang et al. 2013 [6].** As during the absence of sun' irradiation, a backup system is required to ensure the continuity of delivering power to customers, the feasibility of hybridization with renewable or conventional energy has been highlighted by **Pramanik et Ravikrishna 2017 [7]**

Based on the paper of **Tomislav et al. 2012 [8],** there are about 47 parabolic trough power plant around the world with 33 in Spain, 7 in USA and 2 in Iran. Italy, Morocco, India, Egypt and Algeria has one plant for each.

Pelay el al. (2017) [9] have divided CSP plants into five groups 19 plants in operation with production began before year 2000, 24 plants in operation with production started between year 2000 and 2010, 85 plants in operation with production began after 2010, 35 plants now under construction, and 74 planned plants. The total number of these samples

reaches 237 CSP plants. They include commercial, demonstration, research and development plants.

From the historical evolution of used CSP technologies, parabolic trough collector (PTC) and solar power tower (SPT) are the most used technologies for plants in operation. Meanwhile, trends also show that there will be a higher ratio of SPT for CSP plants in project. Linear Fresnel reflector (LFR) represents the third most frequently used CSP technology. Parabolic dish collector (PDC) is a relatively young technology with no plants in activity. Nevertheless, it represents 7–9% of plants under construction and planned, making it a non-negligible technology in the future (**Pelay el al. (2017) [9]**).

A parabolic trough solar power plant is composed of solar field (PTC unit including solar receiver, parabola and structure with tracking system), thermal storage as if it is required and power block (turbine, generator, etc.). Only parts of the PTC unit are discussed in present work.

A parabolic trough collector consists of a highly reflective parabolic mirror with a solar receiver positioned at the focal line of the parabolic. The heat transfer fluid (thermal fluid) is heated by the solar energy reflected and concentrated by mirror onto the receiver tube. During high insolation, solar energy can be stored to be used during low or no insolation for steadier electricity production. The metal support structure is used to support the weight of the parabolic and the tracking mechanism as well as the wind loads.

1.4.1. Solar Receiver

The solar receiver or heat collection element (HCE) is one of the main functional units of a solar PTC. Many techniques were attempted to enhance the heat transfer potential in the tube receiver. Which, includes techniques such as half insulation receiver, cavity receivers, vacuum outer shell, inclusion of inserts (turbulators), baffles, artificially roughened sinks, selective coatings. The outer surface of the receiver tube is basically coated to improve its solar radiation absorbance and to limit its thermal radiation emittance. The receiver tube also placed inside evacuated glass envelope to reduce both convective and radiative heat loss from the tube receiver. The solar receiver is considered as a key element in the parabolic trough system, it should loss less thermal energy principally by radiation and increasing its heat

transfer to the thermal fluid. The heat transfer to the thermal fluid can be enhanced by using inserts; which improve the turbulence, creating secondary flow as well as increasing the effective heat transfer area. The inserts can be twisted tapes, coil inserts, dimples, baffles, metal foam, porous discs and corrugated tube etc. A selective coating is very important to increase the absorbance and minimize thermal radiation loss especially for relatively high working temperature, Mo-Al_2O_3, Mo–Si_3N_4, Molybdenum and Silica nitride, matt black painting, black chrome and black nickel-chrome coating can operate up to 600 °C and reaching an absorbance of 98% **(Hafez et al. 2018 [10], Kumaresan et al. 2017 [11])**.

1.4.2. Structure and mirrors

The collector structure must be robust enough to overcome different loads, the structure should be lighter for cost optimization, and challenges of manufacturing have to be carefully estimated. A number of structural concepts have been proposed such as steel framework structures with central torque tubes or double V-trusses, or fibreglass in order to achieve the cost-effectiveness balance **(Kalogirou et al. 1994 [12], Adrian et Randy 2009 [13])**.

The mirrors fixed with a rapid hardening adhesive on the steel structure support, which has an exact parabola shape; finally, the solar collector element is installed on supporting pylons. The installation and mounting of the support structure has high influence on the total plant performance. The support structure has to meet the following structural requirements (**Schweitzer et al. 2014 [14]**):

- The structure must be robust and rigid to hold the initial form of the parabola by avoiding deformations that would be caused by environmental conditions as well as temperature differences.
- Lightness is an effective parameter to reduce cost and improve flexibility of the facilities.

The most commonly reflectors in commercial solar thermal electricity are silvered-glass reflectors, the glass is a very stable material physically and chemically, the main challenge is its fragility especially thin layer, which needed back protection. The poor optical performance of the aluminum can be improved by coated and methacrylate aluminum film, which can be used as future alternative to conventional glass reflectors. A knew under development

reflectors based on silvered-polymer seem to be promising, they are more flexible, cheaper and lighter. They have better optical reflectance then methacrylate aluminum film reflectors. Therefore, silvered-glass reflectors have not yet been displaced, because it has the highest reflectance and long optical durability **(García et al. 2016 [15], Blanco et Santigosa 2017 [16])**.

1.4.3. Thermal fluid

The HTF type is imposed by the solar receiver and the thermodynamic cycle of the plant. In the meantime the HTF properties, define the type of the solar receiver to use, from recent studies, the tube geometry is the most common receiver. High thermal conductivity improves heat transfer, so introducing inserts to improve heat transfer could be avoided. Low viscosity can reduces pressure drop, so low working pressure permits the use of thin wall, thus reducing wall temperature gradient and mechanical stress, as a result long lifetime of the receiver tube and less cost. A large specific heat capacity can be an advantage for direct thermal storage. Current thermal fluids used in CSP plants: thermal oil, molten salt and water-steam can achieve thermodynamic efficiency from 35 to 42%. New molten salt, liquid metals, pressurized gases, supercritical fluids, particle suspensions are new HTFs, which are considered stable at 700 °C and more. Using knew HTFs can achieve a thermodynamic efficiency up to 50% and more (**Benoit et al. 2016 [17])**.

1.4.4. Thermal storage

The main disadvantage of solar energy is its intermittently. The stored thermal energy during sunshine periods, can be used during insufficient irradiation to reduce the dependence to conventional energy hybridization by burning fossil fuel. About 47% of the solar plants in operation integrate thermal energy storage (TES) system. There are currently three kinds of TES systems available: sensible Heat storage, latent heat storage and thermo-chemical heat storage. The type of TES system to be used, depends mainly on the cost of investment and the fluid to be stored (**Pelay el al. (2017) [9])**.

- Sensible heat storage: is currently the most commonly used technology with their limited energy density; it exists in solid form (sand, rock, mineral oil, cast iron etc.). most studied material are solid such as concrete, castable ceramics, new concrete with polypropylene fibers, and other material such as graphite; liquid such as molten salt,

solar salt, Hitec, salt with nanoparticles and other liquid like oils, liquid sodium; and gaseous materials like compressed air or steam.

- Latent heat storage: it is based on phase change material (PCM), it could be solid-liquid or solid-solid, it is known with its higher energy density but low thermal conductivity thus long charge and discharge processes. The conductivity may enhanced by some additives to PCM, like metal alloys, graphite, insertion of a metal matrix or foam as well as special design of TES system with embedded heat pipes or finned heat pipes. Inorganic and organic substances can be also used for high temperature range of 100-900°C.

- Thermochemical heat storage: it is based on reversible chemical reactions by endothermic chemical reactions and stored in chemical potential. Then stored heat recovered by the reversed exothermic reaction, sometimes by adding a catalyst. It is 10 times greater than latent storage. Metallic hydrides, carbonates system, hydroxides system, redox system, ammonia system and organic system can be used for thermo-chemical heat storage at medium or high temperatures (300–1000°C). These common materials used in thermochemical storage have low thermal conductivity, which could be improved by expended graphite matrix, aluminum foam and by adding nanoparticles like SiO_2 to improve the problem of thermal stability of thermochemical materials.

1.5. State of the art of the solar receiver as part of the PTC

During the Roman invasion against Greek in the third century B.C, there are rumors that Archimedes had used the soldiers shields or mirrors to concentrate sun' rays onto the Roman fleets, the high temperature resulted from the concentration of sun' rays, turned the Roman fleets into ashes. Many writers have dismissed these rumors. After a Greek and Roman period, Europe entered a Dark Ages. Whereas, science flourished in the North Africa where the first contributions to the theory of optics in 800 years were developed by Abu Ali al-Hasan al-Haitham (born in 965); He correctly argued that vision results from light entering the eye, not the reverse. He tackled practical problems like the origin of rainbows, binocular vision, the apparent increase in size of planets near the Earth's horizon, reflection, refraction, focusing with lenses, and the properties of spherical and parabolic mirrors [18].

The main elements of parabolic trough collector and their characterization parameters are presented in figure 1.2.
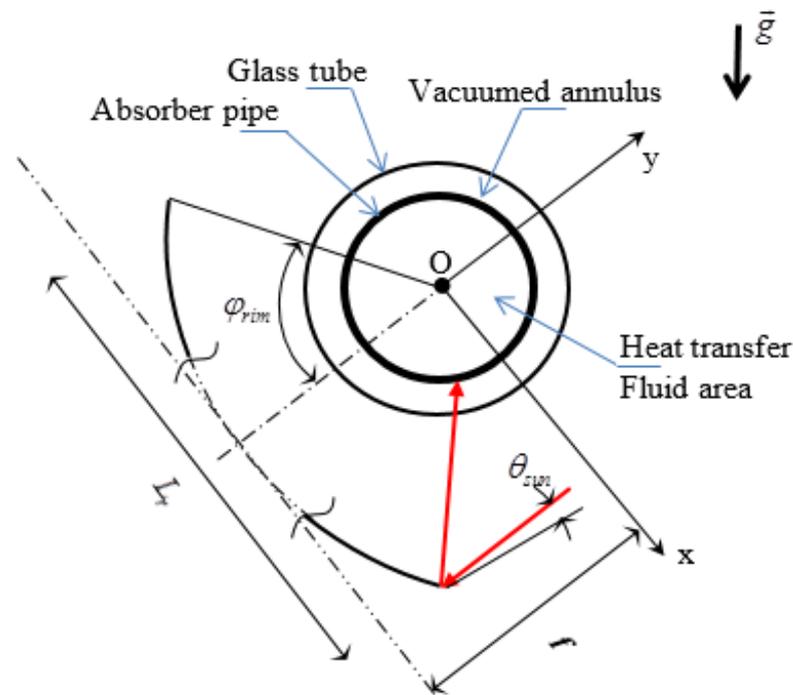
Figure 1.2: Representative cross-section of PTC.

The use of concentrating collectors for furnaces purpose date back to 1774 when the French chemist Lavoisier constructed powerful lenses to concentrate solar radiation, the furnace reached a temperature of 1750 °C using 1.32 m lens plus secondary 0.2 m lens, this temperature was the maximum achieved temperature for a century. In 1875, Mouchot made truncated cone reflector, consisted of silver-plated metal plates with diameter of 5.4 m and collecting area of 18.6 m^2, its moving part weighed 1400 Kg **(Frank 2003 [18], Kalogirou 2009 [19])**.

Abel Pifre, made a solar engine based on parabolic reflectors, which are made of small mirrors and they shaped like Mouchot' truncated cones. Steam engines operated using steam generated by concentrating solar radiation, for different applications such as driving printing machine by Mouchot 1878-1880 and powering water pumping by Eneas in 1901 using 10 m diameter focusing collector. John Ericsson, an American engineer, developed the first steam engine using solar energy systems of eight parabolic troughs, the systems used either water or air as heat transfer fluid. After, In 1912 Frank Shuman with C.V. Boys built a largest pumping

plant parabolic cylinder to focus sunlight onto a long absorbing tube, each cylinder was 62 m, the total area of used cylinders was 1200 m^2. The solar engine had an output of 37 to 45 KW continuously for a period of five hours (**[18]**, **[19]**).

The onset of World War I and II, cheaper fuel and high cost of investment in solar energy caused loss of interest in its development. Interest in solar concentrator began to rise again in the 1960s **[19]**.

The effect of distance from the focal plane on the uniform flux had been revealed by **Robert et al. 1957 [20],** the area of uniform flux decreases as the plane of interest moves away from the focal line, then it increases in size and uniformity at a distance of over two sun images from the focal plane. The plane of interest should be positioned within a distance of one-half of a sun image unit from the focal plane in order to get maximum delivered flux. For studied range of rim angles between 30° to 60°, the heat flux increases as the rim angle increases as well as for the flux distribution.

In 1961, Cobble [21], presented a theoretical concentration as a function of relative aperture (mirror aperture to focal length), he developed the optimum concentration for plate, circular cylindrical and parabolic cylinder mirror targets, he considered a parabolic cylinder mirror target with a relative aperture of 4 as an ideal target shape.

Lof et al. 1962 [22], studied experimentally and theoretically a parabolic cylindrical reflector with aluminum sheet of 12 feet length, 6.19 feet aperture, focal length 1 foot, rim angle 114°, the reflector assembly inclined at 40° with the horizontal, with a tracking system. The receiver made of standard wrought iron pipe, which were coated with a flat black paint with an absorptivity of 0.95 for diameter receivers from 1.9 to 2.375 in, except for diameter of 1.05 in where the absorptivity was 0.93. The average reflectivity of aluminized Mylar reflector surface was 0.76 at average incident angle of 20 deg. The smaller tube failed to intercept a larger portion of the radiation and resulted in 31 % loss in shape factor, in terms of heat losses, beyond operating temperature of 350 F small tube had lower loss. Reflector misalignment results in shifting and enlargement of the focal zone and consequent shape factor discrepancies, particularly with the smallest receiver. Theoretical and experimental

curves of efficiency, average intensity as well as maximum focal zone flux go through a maximum at an optimum receiver radius.

The elliptic cylinder attains a higher concentration than both the parabolic and the circular pipe targets. The optimum target geometry could reach a slightly higher absolute value for maximum concentration than other target geometries **(Lumsdaine and Cherng 1976 [23]).**

Experimental and theoretical comparative study was performed by **Singh and Cheema 1976 [24]**, They constructed and studied cylindrical reflector of parabolic cross section and a circular absorber with length 244 cm, focal length 7.62 cm and relative focal length (f / L_r) of 0.1. The reflecting surface was of buffed aluminum. The receiver assembly consisted of a copper tube coated with a thin layer of nickel oxide and enclosed in the concentric glass tube. The authors showed the performance and optimal parameters of cylindrical parabola collector. Ideal theoretical concentration ratios for flat, circular, and the parabolic cylinder mirror of **Cobble [21]** had been modified by introducing insulating factor instead of considering the surface, which does not receive the reflected sunrays as perfectly insulated. The use of aperture as a characteristic length has many advantages over the use a focal length as characteristic dimension. The performance of the absorber can be defined as a ratio of the absorber temperature to the stagnation temperature. Absorptivity to emissivity ratio and the stagnation temperature can be used as a rough guide for the selection of a coating. Finally, the performance of the collector was well predicted.

Ramsey et al. 1977 [25] studied experimentally a cylindrical parabolic trough concentrator which, is 1.2 m wide and 4.2 m long with focal line of 19.4 cm. Alzak, anodized aluminum reflector sheeting, used as reflector of the parabola with measured reflectance of 0.81. The absorber tube has an outer diameter (OD) of 2.54 cm, surrounded by a glass of 10 cm inner diameter (ID) under vacuumed annulus and the water was used as HTF. A heat pipe working at low temperature around 40 °C and two absorbers of stainless steel working at temperature of 300 °C, were used: A heat pipe painted with 3M Black Velvet with absorptance of 0.95. An absorber electroplated with bright nickel covered by Al_2O_3-MoO_x -Al_2O_3 (AMA) coating with absorptance of 0.91 and an emittance at 300°C of 0.2. The second absorber

coated with a nonselective black paint with absorptance and emittance of 0.96. The authors observed a little effect of tracking error within ±0.5 deg on the performance, beyond that the effect becomes more severe. As the operating temperature increases, the performance decreases and the heat loss increases too. The thermal loss of selective coated absorber operating at 300 °C is lower than that for the non-selective case. In the case of selectively coated absorber, the maximum efficiency obtained around solar noon is approximately 50 percent, whereas it is around 22% in the case of non-selectively coated absorber.

In the 1980s, most studies were concentrated on compound parabolic concentrator (CPC) to enhance the amount of sun' rays, which could be reflected by mirror and eventually concentrated onto the receiver tube. A comparison have been made between simple parabolic concentrator (SPC) and CPC in terms of materials use, acceptance angle and concentration ratio. SPC has an advantage in reduced materials used over CPC, but CPC has higher acceptance angle by three times. The SPC can collect most non-direct radiation with concentration ratio less than 10 (by enlarging the absorber tube to intercept defocused radiation) (**Grimmer 1979 [26]).** Newly designed reflector (CPC) by **Mcintire 1980 [27]** to eliminating gap losses between the tubular absorber and the reflector and enhancing the absorptance of the receiver**.**

The mirror-receiver tube intercept factor, absorptivity-transmissivity product of the receiver tube and cover tube, the end loss factor and receiver tube misalignment, an absorber with low emissivity coatings, glass-tube annulus evacuation and anti-reflection coating. These factors and other influence the performance of the PTC, therefore they should be identified for the design of the PTC **(Clark 1982 [28]).**

A ray-tracing technique comparison between CPC and PTC demonstrated that CPC has superior optical behavior regarding the acceptance angle and the exploitable part of the diffuse insolation **(Prapa et al. 1987 [29])**. A superior performance can be achieved with CPC incorporating inverted-Vee absorber fin rather than conventional cusp-reflector CPC design **(Norton et al. 1989 [30]).**

Grald et al. 1989 [31] studied by one-dimensional finite-difference FORTRAN 77 program the influence of mass flow rate, acceptance angle, receiver dimensions, and

material properties on the thermal efficiency. Studied tube is composed of an envelope, fluid inlet channel, porous absorber and an insulation. The porous absorber consists of several layers of etched stainless steel screen with 50 meshes per inch (20 per cm). The screen has a porosity of approximately 0.4 and is 0.12 inch (3 mm) thick.

A unified model for optics and heat transfer in line-axis concentrating solar collector were used to simulate heat transfer around the receiver tube of CPC. The combination of two-dimensional steady state finite element analysis of convective heat transfer and ray-trace techniques highlighted the effect of acceptance angle, inclination, focal line and other parameters on heat transfer of the CPC **(Eames et al. 1993 [32]).**

Dudley et al. 1994 [33] studied thermal efficiency and thermal losses of three receiver configurations with vacuumed annulus, air in the annulus and bare tube, two types of coating applied to the steel receiver tube were used cermet selective and black chrome coating. Tested module is similar to the smallest portion of complete SCA LS2 PTC used in Solar Thermal Electric Generation Systems (SEGS) with 7.5 m length and an aperture of 5 m. The LS2 presents 65% of three generations of installed collectors at the nine SEGS plants. The on-sun test performed at Sandia National Laboratories (SNL) showed that efficiency of cermet coating is better than that of black chrome. The heat loss of bare tube and air in the annulus is greater than that of vacuumed annulus, the heat loss increases considerably as fluid temperature increases.

Odeh et al. 1998 [34] studied the performance of a parabolic trough collector LS2 from SEGS plant to develop a model of thermal loss of the collector basing on correlation function. Their model showed that the thermal loss of vacuumed insulted absorber is less than that of lost vacuum and bare tube showed higher thermal loss. The authors studied the heat transfer variation with respect to the water phase (single-phase water, mixture of liquid water and steam, dry steam). The effect of the absorber temperature and the inlet temperature on heat loss had also been conducted. The heat loss when using synthetic oil as heat transfer fluid was found to be greater than when using water. The thermal stress severity might be controlled by adjusting feed water flow rate with radiation level thus; constant temperature two-phase region should cover most of the absorber tube.

The EUROTROUGH - Parabolic Trough Collector would permit the reduction of solar field cost by 14% due to the weight reduction and could be integrated in the successful SEGS plants of California. The weight of EUROTROUGH is about 14% lesser than the weight of LS-3 collector. The structural deformation of the new design is considerably less than LS-3. Therefore, the sealing against leakage during operation has been improved. The thermal annual output improved up to 20% thanks to improved absorptivity and emissivity, the applied Universal Vacuum Collector (UVAC) selective coating is designed to work at vacuum and exposed outdoor conditions, with no oxidation or oxide deposit on the glass tubes at temperature up to 400 °C. The glass to metal connection zone and the bellow connections are shielded in the way of maintaining fixed relative position in spite of the dilation of the tube during heat up **(Geyer et al. 2002 [35]).**

Cylindrical parabolic trough concentrator simulation was run by **Singh and Sulaiman 2003 [36]**, the simulation run for three different working fluid, the concentration ratio increased until a maximum theoretical value of 212, the efficiency increased until the concentration ratio reached 10 then gradually decreased by at least 53%. The balance should be achieved, the increasing in the aperture area, increases the heat loss but in the meantime decreases the optical loss.

Brooks et al. 2005 [37] constructed a parabolic trough collector, characterized by a collector of 5 m long, aperture width of 1.5 m and rim angle of 82.2°. The surface consists of stainless steel sheets covered with SA-85 film. An absorber tube of diameter 28.6 mm giving a concentration ratio of 16.7, the absorber was coated with selective coating, a glass tubing with transmittance of 0.92 and refractive index of 1.473. The annulus was sealed using temperature-resistant O-rings allowing for expansion of the inner absorber. A single vent enabled evacuation of the annulus using a vacuum pump. The water is used as heat transfer fluid at turbulence regime. The maximum temperature in this study was limited at 80 °C due to limitations in the fluid circulation system. At lower temperatures, heat loss is low and the glass adversely affects performance by reducing optical efficiency. At higher temperatures, performance is dominated by heat loss, which is prevented more effectively by the shielded receiver.

Arasu and Sornakumar 2006 [38], studied the performance of a new parabolic trough collector hot water generation system with a well-mixed hot water storage tank, the parabola with a rim angle of 90°, constructed of fiberglass, the solar reflector material is SOLARFLEX foil with reflectance of 0.974. The copper tube coated with a heat resistant black paint used as receiver tube of 1.25 m length positioned at a focal length of 0.2 m, the annular gap around the receiver ensured by a glass envelope and rubber cork seals at both ends. Temperature, solar beam radiation intensity, mass flow rate and the wind speed were measured by resistance temperature device (RTD) sensors, pyrheliometer, rotameter and vane type anemometer respectively. The efficiency depends on incident beam radiation and the useful heat gain, the storage tank temperature raised from an initial temperature of 35°C to a maximum temperature of 73.84°C as no energy withdrawn from the storage tank during the collection period of 7 hours counting from 9 A.m on April 30, 2005 in India.

Krüger et al. 2008 [39], studied experimentally Solitem PTC1800 for medium working temperature 150 to 190°C to produce steam as driving medium for the absorption chillers. The mirror shape characterized by absorber reflection method (ARM), they found according to ray tracing calculations an interception factor of 83%, the temperature, mass flow and direct normal irradiation (DNI) were measured by adequate sensors. The study revealed relatively low thermal loss and significant optical losses.

The most recent studies have concentrated on the receiver as a key element in PTC system. The heat transfer enhancement has consumed scientists theoretically and experimentally. Introducing inserts (turbulators) in receiver tubes have been studied thoroughly. The coating technique to improve optical properties of the receiver has been interesting subject. The practical technique to evaluate the heat flux around the receiver tube has been relatively achieved by MCRT.

Burkholder and Kutscher 2008 [40] performed an off-sun test of the Solel UVAC3, they developed a correlation predicting heat loss from the absorber to the ambient based on the average temperatures difference of the receiver and the ambient; the correlation is valid for ambient temperature ranges from 13 °C to 33 °C. However, developing this heat loss correlation is not the only parameter to evaluate the receiver performance. Later, in **2009** the authors **[41]** studied Schott 2008 model year PTR70 receivers performed inside the laboratory

under controlled conditions. The authors derived the emittance of the absorber from heat loss testing results and introduced it in the heat loss model correlation. Based on this correlation, improved selective coating of Schott 2008 PTR70 model improved electricity generation by 5% relative to previous PTR70s model.

1.5.1. Heat transfer enhancement in the receiver tube by introducing inserts

Reddy and Satyanarayana 2008 [42] developed 3D numerical model to evaluate the performance of the receiver tube of the solar parabolic trough concentrator (SPTC) with different configurations of porous inserts of square, triangular, trapezoidal and circular shapes. The authors used k-ε RNG turbulent model with standard wall function approach using the CFD package FLUENT. The receiver tube with trapezoidal fin showed better performance. At a Therminol VP1 flow rate of 6.4 Kg/s, the heat transfer enhancement is about 13.8% with a pressure drop of 1.7 KPa.

The numerical study of thermal analysis of solar parabolic trough with porous disc receiver showed that the introduction of porous discs in the receiver improves the heat transfer but with a price of pressure drop. The top half-porous disc receiver with an inclination of 30° permitted higher enhancement in heat transfer with 64.2% and 457 Pa as pressure drop for Reynolds number of 31845 in comparison to conventional tubular receiver (**Kumar and Reddy 2009 [43], Mwesigye et al. 2015 [44]).**

Muñoz and Abánades 2011 [45], [46] investigated numerically a possible improvement in terms of thermal efficiency of the receiver tube by introducing helical internal fins. The authors presented that the overall performance enhancement by 2% is reachable. Lower helix angle is sufficient for enough mixing with lower pressure drop unlike high helix angle, which causes excessive pressure drop. The authors believed that the cost increase of the finned collector tube could be compensated by not using absorbing coating, the glass and the glass-tube vacuum system as well as maintenance cost reduction motivated by the reduction in tube mechanical fatigue caused mainly by large temperature differences in conventional tube. After, **Huang et al. 2015 [47]** studied in addition a receiver with dimples and protrusions, they found that the performance evaluation criteria (PEC) for tube with dimples is 1.23 to 1.37, which is greater than the PEC for tubes with protrusions and helical fins. **Huang et al. 2016**

[48] presented fully-developed mixed turbulent convection in dimpled parabolic trough receiver tubes, the authors concluded that the heat transfer under non-uniform heat flux (NUHF) is larger than that under uniform heat flux (UHF), the comprehensive performance decreases as dimple depth becomes excessive.

The combination of finite volume method (FVM) and the Monte Carlo ray-trace (MCRT) method were used for numerical study on the uni-lateral milt-longitudinal vortices enhanced parabolic trough solar receiver (UMLVE-PTR) **(Cheng et al. 2012 [49])**. The authors evaluated the performance of the novel absorber tube relatively to the smooth absorber tube. The thermal loss of the novel absorber can be reduced by 12.1%. All the values of PEC of the novel absorber tube are greater than those of the conventional tube.

Wang et al. 2013 [50] studied numerically the effect of inserting metal foams in receiver tube of parabolic trough collector on the heat transfer. For a constant porosity, the ratio effects of metal foam height to the tube diameter, on the thermal performance is great. Where the ratio of 0.25 of inserted metal foam at the bottom of the tube, generated up to 10 times increase in the Nusselt relatively to the LS2 tube/SGES plant with a pressure drop of 10-20 times larger, this gave an improvement in PEC up to 3.2.

A parametric study on the heat transfer and pressure drop with and without using inserts for CO_2 and He as working fluids has been conducted. This study showed that deep protrusions could offer an overall higher performance regarding heat transfer and pressure drop compared to other configurations: internal enhancements through tube insertions of coil/wire, twisted tape and porous foams as well as enhancements through dimpling of the tubes **(Too and Benito 2013 [51]).**

An experimental study on the absorber with tape inserts had been carried out by **Waghole et al 2014 [52].**The absorber had an inside diameter of 20 mm, 1 mm thickness and 1500 mm length. The absorber heated by an electrical band heater wounded over it. The experiment conducted for Reynolds number range from 500 to 6000, showed pressure drop increase with increasing helix angle due to higher swirling flow and long residence time in the absorber. Absorber with tape inserts had an enhancement factor between 135% and 205% with constant pumping power.

Mwesigye et al. 2014 [53] evaluated numerically the thermodynamic performance of a parabolic trough receiver with centrally placed perforated plate inserts. The modified thermal efficiency of studied receiver is from 1.2 to 8% compared to conventional receiver, the temperature gradient of the receiver could be reduced by 67% and minimizing the entropy generation by up to 52.7% by improving the thermodynamic performance of the receiver.

A receiver tube of solar parabolic trough concentrator with louvered twisted-tape inserts was studied numerically by **Ghadirijafarbeigloo et al. 2014 [54]** using the RNG of k–ε turbulence model. The Soltrace code was used to determine the non-uniform wall solar heat flux. The twisted-tape is characterized by the ratio of its length to its width. The Nusselt number of louvered twisted-tape tube is higher than that of conventional receiver by 150% and twisted-tape tube by 37%. The pressure penalty in louvered twisted-tape receiver was 210% and 72% higher than that of conventional and twisted-tape receivers respectively.

A numerical study of parabolic trough receiver with nonuniform heat flux and helical screw-tape inserts by **Song et al. 2014 [55]** showed that pressure drop of tube with inserts, jumped from 4 for 0.11 Kg/s to almost 19 times for flow rate of 0.6 Kg/s in comparison to smooth tube. Whereas the heat loss reduced from 6 to only 3 times, according to the authors, this type of inserts might be not suitable for higher flow rate. The authors used characteristics and dimensions of CAMDA-PTC in their model and the heat flux on the outer surface of the receiver tube is obtained using simplified MCRT.

Chen et al. 2015 [56] studied numerically and experimentally a novel linear cavity for PTC. A comparison between cavity with and without inserted fins with glass cover and without glass cover were performed. The working temperature of the cavity could reach 570 K so it can be used for industrial drying and cooling system. The results show that the heat loss from the cavity without glass is relatively higher than that with glass and more energy transmitted to the working fluid in the cavity with glass than without glass. As more of thermal energy was transmitted from the absorbing surface to the working fluid by convective heat transfer in case of inserted fins, the temperature of absorbing surface decreased. Subsequently, less heat loss and higher thermal performance.

A detailed experimental study have been conducted by **Reddy et al. 2015 [57]**, the authors studied six configurations unshielded tubular receiver (USTR), shielded tubular receiver (STR), bottom porous disc receiver (BPDR), U-shaped bottom porous disc receiver (UBPDR), inclined bottom porous disc receiver (IBPDR) and alternative porous disc receiver (APDR). The result of efficiency for APDR of 66.26% to 69.42% corresponding flow rates of 100 L/h to 1000 L/h at 900 W/m2 is considered as the highest for studied configurations. The heating and cooling time constant for USTR at 300 L/h is the highest with 260 s, the variation of time constant for heating and cooling test is more at lower flow rates and almost equal at higher flow rates for all receiver configurations. Heat losses from the porous disc receiver are less compared to the tubular receiver.

A numerical investigation by **Chang et al. 2015 [58]** on heat transfer enhancement in solar receiver tube with twisted tapes using molten salt was carried out. The heat enhancement found to increase with the decrease in both clearance ratio (difference between the tube inner diameter and the width of twist to the tube inner diameter) and twist ratio (length of twist to its width). An enhancement of 2.9 times in Nusselt with 2.5 times pressure loss relatively to smooth tube was found for a twist ratio 2.5 and clearance ratio zero. **Mwesigye et al. 2016 [59]** studied parabolic trough receiver with detached twisted tape inserts for a wide range of Reynolds 10260 to 1353000, the simulation revealed a maximum reduction in entropy up to 58%. For twist ratio greater than 1, the thermal efficiency can reach 10%. Temperature differences of the absorber circumferential might be reduced by up to 68%.

Jaramillo et al. 2016 [60] investigated the benefit of using twisted tape inserts in the parabolic trough receiver tube for low Reynolds number. Based on the first and the second laws of thermodynamics, the thermal and exergy efficiencies have been studied. The optimal conditions to enhance the heat transfer of proposed PTC are using small flow rates 1 lpm with twist ratio (Tape pitch length to Tape width) close to 1. The enhancement of the exergy efficiency is possible only when the augmentation in entropy generation number is less than one.

1.5.2. Heat transfer enhancement in the receiver tube without introducing inserts

Demagh et al. 2015 [61] proposed a novel receiver tube to homogenize the concentrated solar radiation without affecting the interception factor; the proposed PTR tube has an S-curved shape and would not include any additional parts. The authors highlighted the 3D nature of the concentrated heat flux density distribution with regard to the 2D nature of the PTR-CSST.

PTC tube with wavy internal surface (Converging-diverging sine shape) has an efficiency improvement of 4.5% compared to conventional tube. The study of three cases shows the mean increase in heat transfer using nanoparticles, pressurized water and wavy tube by 6.34%, 4.55% and 4.25% respectively. The thermal efficiency increases with the increase in the inlet temperature **(Bellos et al. 2016 [62]).**

Restraining thermal strain of receiver tube for PTC by using asymmetric outward convex corrugated tube has been investigated numerically by **Fuqiang et al. 2016 [63], [64].** The authors presented that convex corrugated tube can be as effective as 26.8% compared to conventional tube in terms of thermal strain reduction. The overall heat transfer performance improvement of proposed tube can reach 148%.

1.5.3. Heat transfer enhancement of the receiver tube using selective coating

Concentrating solar power operates from 400 °C to 500 °C or higher, new efficient selective coating to have high solar absorptance and low thermal emittance at 500°C are required. The silicides and carbides are of interest for CSP applications, especially if an aniti-reflective (AR) layer is added to increase the absorptance and the copper metallic layer is replaced with a more temperature-stable reflective layer to improve durability. The silicon, germanium, and boron tandem absorber with AR coatings Si_3N_4/ ZrB_2 seems promising for CSP applications due to its absorptance up to 0.93 and its stability at higher temperature up to 500 °C and beyond. Adding porous SiOx AR layer could improve absorptance up to 0.98. Molybdenum (Mo-MoO_2) known as black moly could be used for CSP applications. A multiple cermet layer as tungsten or molybdenum/aluminum nitride W/AlN or Mo/AlN and selective solar-transmitting coating like a highly doped semiconductor like Fluorine-doped tin oxide

(SnO$_2$: F) as well as Textured stainless-steel can be useful at higher temperature (**Kennedy 2002 [65]**).

Cheng et al. 2013 [66] presented that solar selective absorbing using denser Mo–Al$_2$O$_3$ layer coating could improve significantly thermal stability at CSP working temperature up to 400 °C and beyond. The Mo diffuses easily into Al$_2$O$_3$ layer, which increases the degradation of the optical properties; this problem could be solved by using high temperature resistant alloy, or even ceramic, instead of the single metal Mo.

Solel Solar Systems, Ltd manufactures HCE, fabricated from stainless steel with cermet coating, such Mo-Al$_2$O$_3$ cermet has good optical properties α/ε_M (350°C) = 0.96/0.16 for 350 °C < T <500 °C in vacuum and demonstrated good thermal performance. After exposure to air at operating temperatures above 300 °C, the Mo-Al$_2$O$_3$ cermet degrades and coats the glass tube with an opaque white precipitate that gives the tube the appearance of a fluorescent light. Solel developed a new HCE product of an improved receiver tube called the Universal Vacuum Collector (UVAC). The UVAC uses a new multilayer Al$_2$O$_3$-based cermet that does not use Mo, with an improved AR coating that is quoted to have more than 97%-98% absorptance and emittance of 0.1-0.07 at 400 °C, which is stable in air and humidity at high temperatures with almost no degradation of optical parameters (**Kennedy 2002 [65]).** A preliminary simulations by HITECO project presented by **Barriga et al. 2014 [67],** have shown the use of alumina as diffusion barrier deposited on the stainless steel tube before a selective coating, the alumina will be replaced by Silicon Nitride in the future to have better performance as diffusion barrier. Then, a selective absorber coating consists: of an infrared mirror made of silver to reduce the emissivity, high metal content cermet (Cermet H), a low metal content cermet (Cermet L) and an antireflection layer made of SiO$_2$ to increase the absorptivity will be deposited on the diffusion barrier. The aim of this new selective coating is to reach an absorbance of 95.2% with reduced emittance and lifetime extending to 25 years at working temperature up to 600 °C.

based on optical simulations and precise control of layers thickness and composition, **Céspedes et al. 2014 [68]** reported on the novel Mo–Si$_3$N$_4$ based selective coating for high temperature concentrating solar power applications, the new stack composed of silver IR-mirror, double cermet absorber and on top a Si$_3$N$_4$ Anti-Reflective layer. The absorptivity and

thermal emissivity at 600 °C of 0.926 and 0.109 respectively were obtained. After cycles of annealing (heating up and cooling down), the new stack showed thermal stability above 600 °C.

A comparison by **Kasaeian et al. 2016 [69]** has been made in terms of absorptance and thermal conductivity of three coating matt black painting, the black chrome and the black nickel-chrome. The absorptance coefficient of matt black paint on the steel tube, black chrome coating and black nickel-chrome on the copper tubes under constant heat flux for the ultraviolet and visible range, the absorptance of black chrome and nickel-chrome coating were constant having absorptance of 97.4% and 98% respectively. Whereas the absorptance of the matt black paint was decreased by, increasing wavelength and it has a mean value of 91.4%. The black chrome and black nickel-chrome coatings have relatively good thermal conductivity unlike matt black paint, which has exhibited poor conductivity and it decreases as the heat flux increases.

1.5.4. Improving the numerical approach for the receiver tube using MCRT

A semi-finite formulation including the reflectivity of the reflector, the transmittance and the absorptivity of the atmosphere had been proposed by **JETER 1986 [70]**, then he supposed that the angular finite size of the sun has a uniform intensity (**JETER 1987 [71]).** The supposition of uniformity distribution through the finite size of the sun has little effect on the optical performance and it is simpler to cope with it, this supposition become the base of incoming work on the MCRT technique. The heat flux distribution on the outer surface of the receiver has been investigated using MCRT (**Cheng et al. 2010 [72], 2012 [73] and 2013 [74]),** the authors assumed specular reflectors of perfect alignment and an azimuthal distribution unchanging along the tube. **He et al. 2011 [75]** and **Hachicha et al. 2013 [76]** presented numerical simulation of a parabolic trough solar collector where they used the MCRT to compute the non-uniform heat flux on the outer surface of the absorber under the same assumptions.

Demagh et al. 2015 [61] established an UDF based on polynomial functions using built-in fitting functions of Excel and a linear interpolation method of gotten heat flux data from the MCRT free-code Tonatiuh **[77]** for conventional straight tube as HCE of the PTC unit. The

heat flux density distribution of the UDF has showed great agreement with cited MCRT models. The authors modified and adopted the UDF to be used for S-curved absorber tube as HCE of the PTC unit.

The literature review shows that no study has been conducted on thermo-hydraulic behavior of an S-curved tube as HCE of the PTC unit. The present work investigates the thermo-hydraulic performances improvement of the S-curved tube. Therefore, the thermo-hydraulic simulation of the novel S-curved tube based on the CFD software and the results of the heat flux distribution developed by **[61],** are presented.

Conclusions

This chapter has highlighted the state of the art of the receiver tube as part of the parabolic trough collector. Cited sample of papers, shows the high interest on developing the thermal performance of the receiver tube. In addition, different ideas and techniques to improve the heat transfer by introducing inserts have been highlighted, meanwhile optimizing those inserts for keeping consumed power as low as possible and improving the thermal stability of the receiver.

Most presented works are simulations on the receiver tube with inserts; they showed relatively some encouraging improvement in terms of the thermal performance but the pressure drop still worrying. The simulation of the asymmetric outward convex corrugated tube exhibited an overall heat transfer performance of 148%. In addition, the experimental study of the alternative porous disc receiver (APDR) showed 69.42% of improvement in the efficiency, these conclusions are relative to used operating conditions. Other inserts techniques showed relatively lower PEC.

The novel S-curved tube seems to have higher heat transfer rate due to induced secondary flow even without introducing inserts mainly due to its waviness shape, besides S-curved tube has relatively greater exchanging surface compared to CSST. The pressure drop would be lower as keeping the inside diameter of the receiver tube smooth in comparison to other presented inserts.

References

[1] S.A. Kalogirou, Solar thermal collectors and applications, Progress in Energy and Combustion Science 30 (2004) 231–295.

[2] V.K. Jebasingh, G.M. Joselin Herbert, A review of solar parabolic trough collector, Renewable and Sustainable Energy Reviews 54 (2016)1085–1091.

[3] Technology Roadmap Concentrating Solar Power, OECD/IEA, 2010.

[4] I.L. García, J.L. Álvarez, D. Blanco, Performance model for parabolic trough solar thermal power plants with thermal storage: Comparison to operating plant data, Solar Energy 85 (2011) 2443–2460.

[5] H. Price, E. Lüpfert, D. Kearney, E. Zarza, G. Cohen, R. Gee, R. Mahoney, Advances in Parabolic Trough Solar Power Technology, Journal of Solar Energy Engineering, 124 (2002) 109–125.

[6] H.L. Zhang, J. Baeyen, J. Degrève, G. Cacères, Concentrated solar power plants: Review and design methodology, Renewable and Sustainable Energy Reviews 22 (2013) 466–481.

[7] S. Pramanik, R.V. Ravikrishna, A review of concentrated solar power hybrid technologies, Applied Thermal Engineering, 127 (2017) 602-637.

[8] T.M. Pavlović, I.S. Radonjić, D.D. Milosavljević, L.S. Pantić, A review of concentrating solar power plants in the world and their potential use, in Serbia, Renewable and Sustainable Energy Reviews 16 (2012) 3891 – 3902.

[9] U. Pelay, L. Luo, Y. Fan, D. Stitou, M. Rood, Thermal energy storage systems for concentrated solar power plants, Renewable and Sustainable Energy Reviews 79 (2017) 82–100.

[10] A.Z. Hafez, A.M. Attia, H.S. Eltwab, A.O. ElKousy, A.A. Afifi, A.G. AbdElhamid, A.N. AbdElqader, S-E.K. Fateen, K.A. El-Metwally, A. Soliman, I.M. Ismail, Design analysis of solar parabolic trough thermal collectors, Renewable and Sustainable Energy Reviews 82 (2018) 1215–1260.

[11] G. Kumaresan, P. Sudhakar, R. Santosh, R. Velraj, Experimental and numerical studies of thermal performance enhancement in the receiver part of solar parabolic trough collectors, Renewable and Sustainable Energy Reviews 77 (2017) 1363–1374.

[12] S.A. Kalogirou, S. Lloyd, J. Ward, P. Eleftheriou, Design and Performance Characteristics of a Parabolic-Trough Solar-Collector System, Applied Energy 47 (1994) 341-354.

[13] A. Farr, R. Gee, The SkyTrough™ Parabolic Trough Solar Collector, proceedings of the ASME 2009 3rd International Conference of Energy Sustainability, San Francisco, California, USA, 2009.

[14] A. Schweitzer, W. Schiel, M. Birkle, P. Nava, K.-J. Riffelmann, A. Wohlfahrt, G. Kuhlmann, ULTIMATE TROUGH® - Fabrication, erection and commissioning of the world's largest parabolic trough collector, Energy Procedia 49 (2014) 1848 – 1857.

[15] A. García-Segura, A. Fernández-García, M.J. Ariza, F. Sutter, L. Valenzuela, Durability studies of solar reflectors: A review, Renewable and Sustainable Energy Reviews 62 (2016) 453–467.

 [16] M.J. Blanco, L.R. Santigosa, Advances in Concentrating Solar Thermal Research and Technology, Woodhead Publishing Series in Energy, 2017.

[17] H. Benoit, L. Spreafico, D. Gauthier, G. Flamant, Review of heat transfer fluids in tube receivers used in concentrating solar thermal systems: Properties and heat transfer coefficients, Renewable and Sustainable Energy Reviews 55 (2016) 298–315.

[18] F.T. Kryza, The power of light, McGraw-Hill companies, 2003.

[19] S. Kalogirou, solar energy engineering: process and system, Elsevier's Science & technology, 2009.

[20] R.E. De La Rue, Jr., E. Loh, J.L. Brenner, N.K. Hiester, Flux distribution near the focal plane, Solar Energy, 1 (1957) 94–98.

[21] M.H. Cobble, Theoretical concentrations for solar furnaces, Solar Energy 5 (1961), 61-72.

[22] G.0.G. Lof, D.A. Fester, J.A. Doffie, Energy Balances on a Parabolic Cylinder Solar Collector, Transactions of the ASME, 1962.

[23] E. Lumsdaine, J.C. Cherng, On heat exchangers used with solar concentrators, Solar Energy, 18 (1976) 157–158.

[24] P. Singh, L.S. Cheema, Performance and optimization of a cylindrical-parabola collector, Solar Energy, 18 (1975) 135–141.

[25] J.W. Ramsey, B.P. Gupta, G.R. Knowles, Experimental Evaluation of a Cylindrical Parabolic Solar Collector, Journal of Heat Transfer, 1977.

[26] D.P. Grimmer, A comparison of compound parabolic and simple parabolic concentrating solar collectors, Solar energy 22 (1979) 21–25.

[27] W.R. Mcintire, New reflector design which avoids losses through gaps between tubular absorbers and reflectors, Solar Energy 25 (1980) 215–220.

[28] J.A. Clark, An analysis of the technical and economic performance of a parabolic trough concentrator for solar industrial process heat application, Int. J. Heat Mass Transfer, 25 (1982) 1427-1438.

[29] D.E. Prapa, B. Norto, S.D. Probert, Optics of parabolic-trough, solar-energy collectors, possessing small concentration ratios, Solar Energy 39 (1987) 541–-550.

[30] B. Norton, D.E. Prapa, P.C. Eames, S.D. Probert, Measured performances of curved inverted-vee, absorber compound parabolic concentrating solar-energy collectors, Solar Energy, 43 (1989) 267–279.

[31] E.W. Grald, T.H. Kuehn, Performance analysis of a parabolic trough solar collector with a porous absorber receiver, Sol Energy, 42 (1989) 281–292.

[32] P.C. Eames, B. Norton, Validated, unified model for optics and heat transfer in line-axis concentrating solar energy collectors, Solar Energy, 50 (1993) 339–355.

[33] V. Dudley, G. Kolb, M. Sloan, D. Kearney, SEGS LS2 solar collector-test results, Tech. Report of Sandia National Laboratories SANDIA-94-1884, 1994.

[34] S.D. Odeh, G.L. Morrison, M. Behnia, Modelling of parabolic trough direct steam generation solar collectors, Solar Energy 62 (1998) 395–406.

[35] M. Geyer, E. Lüpfert, R. Osuna, A. Esteban, W. Schiel, A. Schweitzer, E. Zarza, P. Nava, J. Langenkamp, E. Mandelberg, EUROTROUGH - Parabolic trough collector developed for cost efficient solar power generation, 11th SolarPACES International Symposium on Concentrated Solar Power and Chemical Energy Technologies, Zurich, Switzerland 2002.

[36] B.S.M. Singh, F. Sulaiman, Designing a solar thermal cylindrical parabolic trough concentrator by simulation, International Rio3 Congress, World Climate and Energy Event, Rio de Janeiro, 2003.

[37] M. Brooks, T. Harms, I. Mills, DESIGN, Construction and testing of a parabolic trough solar collector for a developing country application, 2005.

[38] A.V. Arasu, S.T. Sornakumar, Performance characteristics of the solar parabolic trough collector with hot water generation system, thermal science, 10 (2006) 167–174.

[39] D. Krüger, Y. Pandian, K. Hennecke, M. Schmitz, Parabolic trough collector testing in the frame of the REACt project, Desalination 220 (2008) 612–618.

[40] F. Burkholder, C. Kutscher, Heat-loss testing of Solel's UVAC3 parabolic trough receiver. Tech report NREL/TP-550-42394. National Renewable Energy Laboratory; 2008.

[41] F. Burkholder, C. Kutscher, Heat loss testing of Schoot's 2008 PTR70 parabolic trough receiver. Tech report NREL/TP-550-45633. National Renewable Energy Laboratory; 2009.

[42] K.S. Reddy, G.V. Satyanarayana, Numerical study of porous finned receiver for solar parabolic trough concentrator. Engineering Applications of Computational Fluid Mechanics 2 (2008)172–184.

[43] K.R. Kumar, K.S. Reddy, Thermal analysis of solar parabolic trough with porous disc receiver, Appl Energy 86 (2009) 1804–1812.

[44] A. Mwesigye, T. Bello-Ochende, J.P. Meyer, Multi-objective and thermodynamic optimization of a parabolic trough receiver with perforated plate inserts, Appl Therm Eng 77 (2015) 42–56.

[45] J. Muñoz, A. Abánades, A technical note on application of internally finned tubes in solar parabolic trough absorber pipes, Sol Energy, 85 (2011) 609–612.

[46] J. Muñoz, A. Abánades, Analysis of internal helically finned tubes for parabolic trough design by CFD tools, Appl Energy 88 (2011) 4139–4149.

[47] Z. Huang, G.L. Yu, Z.Y. Li, W.Q. Tao, Numerical study on heat transfer enhancement in a receiver tube of parabolic trough solar collector with dimples, protrusions and helical fins. Energy Procedia 69 (2015) 1306–1316.

[48] Z. Huang, Z.Y. Li, G.L. Yu, W.Q. Tao, Numerical investigations on fully-developed Mixed turbulent convection in dimpled parabolic trough receiver tubes, Appl Therm Eng, 114 (2017) 1287–1299.

[49] Z.D. Cheng, Y.L. He, F.Q. Cui, Numerical study of heat transfer enhancement by Unilateral longitudinal vortex generators inside parabolic trough solar receivers, Int J Heat Mass Transf 55 (2012) 5631–5641.

[50] P. Wang, D.Y. Liu, C. Xu, Numerical study of heat transfer enhancement in the Receiver tube of direct steam generation with parabolic trough by inserting metal foams, Appl Energy 102 (2013) 449–460.

[51] Y.C. Too, R. Benito, Enhancing heat transfer in air tubular absorbers for concentrated solar thermal applications, Appl Therm Eng 50 (2013) 1076–1083.

[52] D.R. Waghole, R.M. Warkhedkar, R.K. Shrivastva, Experimental investigations on heat ransfer and friction factor of silver nano fluid in absorber/receiver of parabolic trough collector with twisted tape inserts, Energy Procedia 45 (2014) 558–567.

[53] A. Mwesigye, T. Bello-Ochende, J.P. Meyer, Heat transfer and thermodynamic Performance of a parabolic trough receiver with centrally placed perforated plate inserts, Appl Energy 136 (2014) 989–1003.

[54] S. Ghadirijafarbeigloo, A.H. Zamzamian, M. Yaghoubi, 3-D numerical simulation of heat transfer and turbulent flow in a receiver tube of solar parabolic trough Concentrator with louvered twisted-tape inserts, Energy Procedia 49 (2014)373–380.

[55] X. Song, G. Dong, F. Gao, X. Diao, L. Zheng, F. Zhou, A numerical study of parabolic trough receiver with nonuniform heat flux and helical screw-tape inserts, Energy 77 (2014) 771–782.

[56] F. Chen, M. Li, P. Zhang, X. Luo, Thermal performance of a novel linear cavity absorber or parabolic trough solar concentrator, Energy Convers Manag 90 (2015) 292–299.

[57] K.S. Reddy, K.R. Kumar, C.S. Ajay, Experimental investigation of porous disc enhanced Receiver for solar parabolic trough collector, Renew Energy 77 (2015) 308–319.

[58] C. Chang, C. Xu, Z.Y. Wu, X. Li, Q.Q. Zhang, Z.F. Wang, Heat transfer enhancement and Performance of solar thermal absorber tubes with circumferentially non-uniform heat flux, Energy Procedia 69 (2015) 320–327.

[59] A. Mwesigye, T. Bello-Ochende, J.P. Meyer, Heat transfer and entropy generation in a parabolic trough receiver with wall-detached twisted tape inserts, Int J Therm Sci 99 (2016) 238–257.

[60] O.A. Jaramillo, M. Borunda, K.M. Velazquez-Lucho, M. Robles, Parabolic trough solar Collector for low enthalpy processes: an analysis of the efficiency enhancement by Using twisted tape inserts, Renew Energy 93 (2016) 125–141.

[61] Y. Demagh, I. Bordja, Y. Kabar, H. Benmoussa, A design method of an S-curved parabolic trough collector absorber with a three dimensional heat flux density distribution, Sol Energy 122 (2015) 873 –884.

[62] E. Bellos, C. Tzivanidis, K.A. Antonopoulos, G. Gkinis, Thermal enhancement of solar Parabolic trough collectors by using nanofluid sand converging-diverging absorber Tube, Renew Energy 94 (2016) 213–222.

[63] W. Fuqiang, T. Zhexiang, G. Xiangtao, T. Jianyu, H. Huaizhi, L. Bingxi, Heat transfer Performance enhancement and thermal strain restrain of tube receiver for Parabolic trough

solar collector by using a symmetric outward convex corrugated tube, Energy 114 (2016) 275–292.

[64] W. Fuqiang, L. Qingzhi, H. Huaizhi, T. Jianyu, Parabolic trough receiver with Corrugated tube for improving heat transfer and thermal deformation characteristics, Appl Energy 164 (2016) 411–424.

[65] C. E. Kennedy, Review of mid-to high-temperature solar selective absorber materials, Technical report, NREL, Golden, Colorado, USA, 2002.

[66] J. Cheng, C. Wang, W. Wang, X. Du, Y. Liu, Y. Xue, T. Wang, B. Chen, Improvement of Thermal stability in the solar selective absorbing Mo–Al2O3 coating, Sol Energy Mat Sol Cells 109 (2013) 204–208.

[67] J. Barriga, U. Ruiz-de-Gopegui, J. Goikoetxea, B. Coto, H. Cachafeiro, Selective Coatings for new concepts of parabolic trough collectors, Energy Procedia 49 (2014) 30–39.

[68] E. Cespedes, M. Wirz, J.A. Sánchez-García, L. Alvarez-Fraga, R. Escobar-Galindo, C. Prieto, Novel Mo–Si3N4 based selective coating for high temperature concentrating solar power applications, Sol Energy Mat Sol Cells, 122 (2014) 217–225.

[69] A. Kasaeian, S. Daviran, R.D. Azarian, Optical and thermal investigation of selective Coatings for solar absorber tube, Int J Renew Energy Res, 6 (2016) 15–20.

[70] S.M. Jeter, Calculation of the concentrated flux density distribution in parabolic trough collectors by a semi finite formulation, Solar Energy, 37 (1986) 335–345.

[71] S.M. Jeter, Analytical determination of the optical performance of practical parabolic trough collectors from design data, Solar Energy, 39 (1987) 11-21.

[72] Z.D. Cheng, Y.L. He, J. Xiao, Y.B. Tao, R.J. Xu, Three-dimensional numerical study of heat transfer characteristics in the receiver tube of parabolic trough solar collector, International Communications in Heat and Mass Transfer, 37 (2010) 782–787.

[73] Z.D. Cheng, Y.L. He, F.Q. Cui, R.J. Xu, Y.B. Tao, Numerical simulation of a parabolic trough solar collector with nonuniform solar flux conditions by coupling FVM and MCRT method, Solar Energy, 86 (2012) 1770–1784.

[74] Z.D. Cheng, Y.L. He, F.Q. Cui, A new modelling method and unified code with MCRT for concentrating solar collectors and its applications, Applied Energy, 101 (2013) 686–698.

[75] Y-L. He, J. Xiao, Z-D. Cheng, Y-B. Tao, A MCRT and FVM coupled simulation method for energy conversion process in parabolic trough solar collector, Renewable Energy, 36 (2011) 976-985.

[76] A.A. Hachicha, I. Rodríguez ,R. Capdevila, A. Oliva, Heat transfer analysis and numerical simulation of a parabolic trough solar collector, Applied Energy, 111 (2013) 581–592.

[77] M.J. Blanco, A. Mutuberria, P. Garcia, R. Gastesi, V. Martin, Preliminary validation of Tonatiuh. SOLARPACES Symposium, Berlin, Germany. 2009.

Chapter 2:Numerical Models

Introduction

In this chapter, a brief review on heat transfer through longitudinally S-curved tubes including sinusoidal tubes and their advantages compared to conventional straight and smooth tube (CSST) in terms of heat transfer efficiency are presented. A schematic presentation of the the S-curved tube as well as PTC S-curved HCE, is also presented. An SST k–ω eddy viscosity/eddy diffusivity turbulent model using Fluent 6.3 is performed on the novel PTC S-curved tube with geometric characteristics similar to that of the SEGS LS2 absorber pipe **(Dudley et al. [1])**, thus involved equations are shown. Based on the assumptions that are made, the studied tube has a symmetrical view in the azimuthal direction, thus, only a half of the absorber pipe is considered in this analysis. Therefore, a non-uniform heat flux distribution on the outer surfaces of both tubes is presented **(Demagh et al. [2])**. Finally, the post processing method required to treat and present Fluent results is discussed.

2.1. The novel S-curved PTC tube specifications

In view of the practical engineering applications and since the experimental work of **Eustice [3]** on the streamline motion within curved pipes, many researchers focus on the inner heat transfer enhancement and flow characteristics. It is well known that curved pipes enhance the heat transfer not by increasing the effective surface area, but by the fact of their capability to induce a secondary flow within the mainstream. Recent and thorough review of the literature on the potential applications of curved geometries (helical coil, bend tube, serpentine tube, spiral, and twisted tubes) in industrial process have been given by **Vashisth et al. [4].** On the other hand, several numerical studies **[5-9]** have shown the enhancement of the heat transfer inside helical pipes. Besides, there are a limited number of experimental works dealing with the subject of the present study, which represent a limited class of the curved pipes known as longitudinally curved pipes with sinusoidal shapes. **Abou-Arab et al. [10]** presented an experimental study of the pressure drop in the laminar and turbulent regions for isothermal water flowing through a sinusoidal circular pipe. For a curvature ratio $(\delta = D/2R_{curv})$ ranges from $0.0111 \text{ to } 0.71$, the results of the friction factor were relatively

close to the straight pipe data. Abou-Arab and co-authors derived a correlation for the friction factor along the sinusoidal pipe involving the straight pipe friction factor $\left(f_{straight} \right)$ and the curvature ratio $\left(\delta \right)$.

In **2002**, **Yang et al. [11]** expanded the experimental studies of **Abou-Arab et al. [10]** to the heat transfer enhancements of water flowing through a sinusoidal pipe, which is placed inside a larger diameter straight pipe. Their results led to the conclusion that the heat transfer rate may be increased by up to 100% as compared with a straight pipe, while the friction coefficient increased by less than 40%. They derived also a correlation for both the friction factor and the Nusselt number along the pipe introducing a dimensionless quantity defined as $\left(\mathrm{Re} \sqrt{\delta} \right)^{2}$.

Yang et al. [12] analysed numerically the impact of the most important geometric characteristics of the wavy pipe on the heat transfer enhancement and revealed the preponderance of the pipe periodicity and amplitude, the more they are amplified the more the heat transfer rate is enhanced.

Rosaguti et al. [13, 14] presented a numerical study of the fully developed laminar flow of water inside sinusoidal channels with circular and semi-circular cross-sections. The effects of the Reynolds numbers and the amplitude to half-periodic length ratio on heat transfer enhancement and pressure drop are presented. Their results led to the conclusion that the heat transfer enhancement exceeds the relative pressure-drop penalty by factors as large as 1.5 and 1.8.

To exploit the merits cited above in the solar field, a longitudinally S-curved/sinusoidal shape of the absorber pipe is proposed to replace the conventional straight absorber located along the focal line of the PTC reflector. The absorber pipe is defined by sweeping a circular section (xy-plane) along a sinusoidal centreline, showed in Figure 2.1, and is fully characterised by a peak-to-peak amplitude $2A$ and a periodicity length λ. Extracted cross-sections showed in Figure 2.1 are perpendicular to the z-direction.
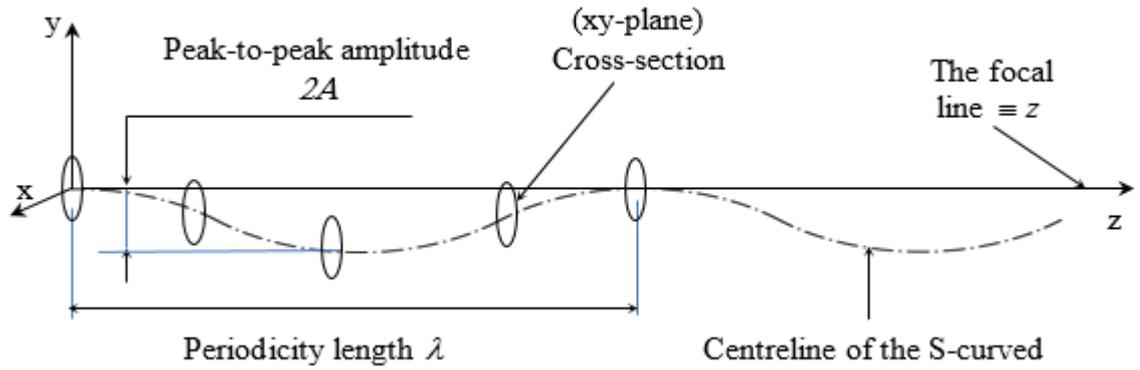
Figure 2.1 : Main characteristics of the S-curved/Sinusoidal absorber.

The equation of the centreline path function of the absorber under consideration in the present study takes the form **[2],**

$$y(z) = A \cdot \left(\cos\left((2\pi/\lambda) \cdot z \right) - 1 \right) \tag{2.1}$$

The curvature radius R_{curv} is defined by $R_{curv} = \dfrac{\left(1 + (y'(z)^2 \right)^{3/2}}{\left| y''(z) \right|}$ **[11].** Thus, differentiate the equation (2.1) with respect to z, substitute into the equation of the curvature radius, and rearrange lead to,

$$R_{curv} = \left(1 + \left(2\pi/\lambda \right)^2 A^2 \sin\left((2\pi/\lambda) \cdot z \right) \right)^{3/2} \Big/ \left(2\pi/\lambda \right)^2 A \cos\left((2\pi/\lambda) \cdot z \right) \tag{2.2}$$

R_{curv} is not constant for a sinusoidal path, but varies along the z-direction.

The y-coordinate of the cross-section centres, computed through the equation (2.1) at any location z, is y_{cs} as illustrated in Figures 2.1 and 2.2(a). Along the entire length of the absorber pipe and for each periodic segment, the coordinate y_{cs} of cross-section centres changes from $y_{cs} = 0$ to the peak-to-peak amplitude $y_{cs} = 2A$ at the middle of the periodicity length $z = \lambda/2$, and so on periodically along the length of the absorber pipe. Figure 2.2(b) shows the sectional drawing of a parabolic trough reflector with the new absorber and Figure 2.3 illustrates the 3D schematic view of S-curved/sinusoidal pipe under consideration in the current study.
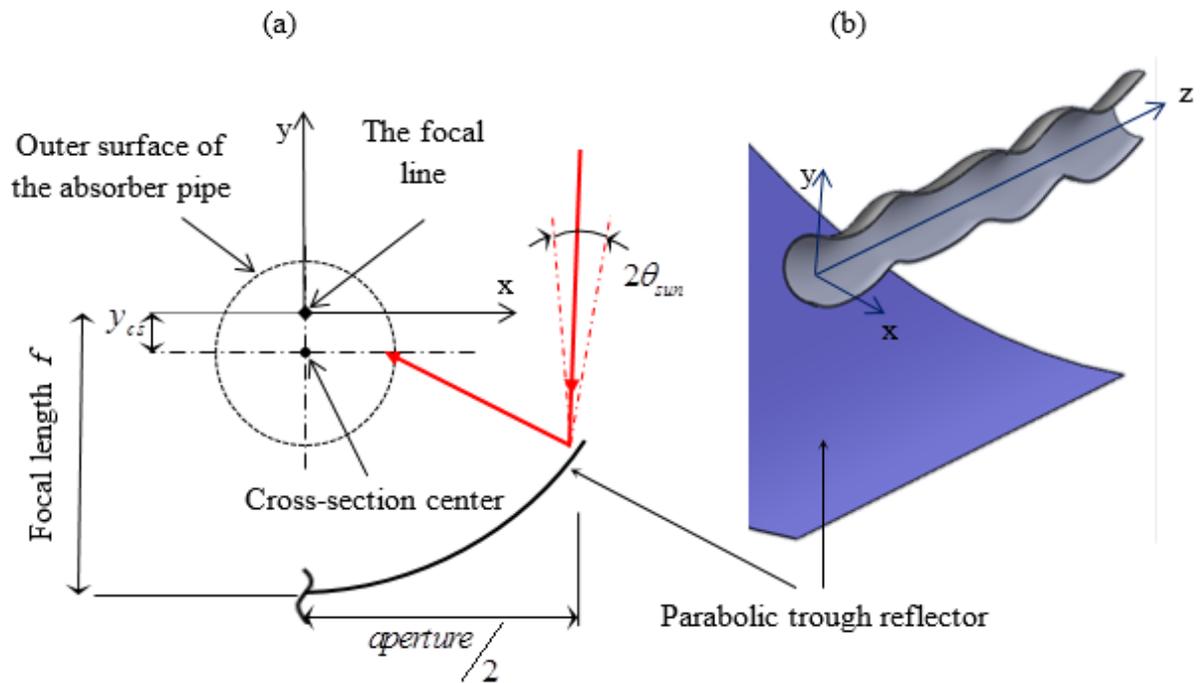
Figure 2.2 : The sinusoidal receiver tube (a) Representative cross-section. (b) Set up of the novel S-curved absorber.
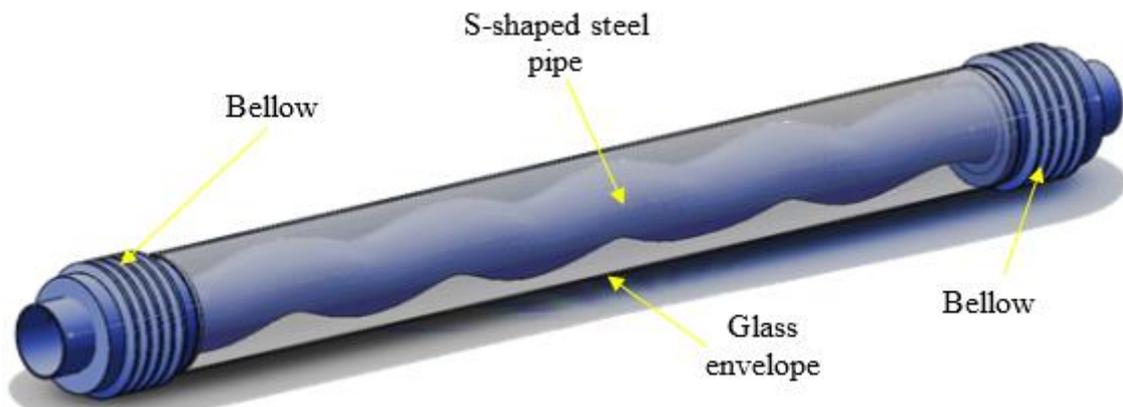
Figure 2.3 : 3D schematic view of the novel vacuumed absorber.

The novel receiver mainly includes an inner stainless steel S-curved absorber pipe with a selective coating on its outer surface (the Cermet- Black chrome in this study), an outer glass envelope with anti-reflective (AR) coatings on its both surfaces, a getter (a chemical sponge not showed in Figure 2.3) to absorb residual gases and bellows at its ends to accommodate for thermal expansion differences between steel and glass materials, which are connected with the conventional glass-to-metal seals. Similar to actual absorbers, the annulus between the absorber pipe and the glass pipe is evacuated to prevent convective heat losses, so only

radiation heat losses take place. Apart from the S-curved shape, the geometric characteristics are similar to the SEGS LS2 absorber pipe [1] and are summarised in Table 2.1 and Table 2.2.

Table 2. 1 : Geometric characteristics of the proposed S-curved/Serpentine absorber.

Component	Characteristics	Description	
Absorber pipe	D_o	Outer diameter of tube	0.070 m
	D_i	Inner diameter of tube	0.066 m
	z_a	Total length	0.975 m
	λ	Periodic length	0.195 m
	2A	Peak to peak amplitude	0.020 m
Glass envelope	D_g	Inner diameter	0.109 m

Table 2. 2 : Optical proprieties [1, 15, 16].

Component	Proprieties	Description	
Absorber Selective coatings Cermet- Black chrome for LS2	α_a	Absorptance	0.96
	ε_a	Emittance	0.14 @ 350°C
Glass envelope	α_g	Absorptance	0.02
	ε_g	Emittance	0.86
	τ_g	Transmittance	0.95

2.2. Governing equations

The most useful model of turbulence in the study of the HTF turbulent flow through helical pipes was the realizable k-ε two-equations turbulence model **(Yang and Ebadian [6-8], Lin and Ebadian [17,18], Li et al. [19], Wu et al. [20], Jayakumar et al. [21]** and **Pawar and Sunnapwar [22])**. Recently **Di Piazza and Ciofalo [23]** exploited the ANSYS CFX to achieve

numerical simulations in curved pipes. Various turbulence models were used and compared, including the standard k–ε with wall functions, the SST k–ω and a second-order RSM. The authors concluded that the SST k–ω eddy viscosity/eddy diffusivity model and the second order Reynolds Stress–ω model give comparable results for the friction coefficient *f* and the Nusselt number Nu, and the best agreement with experimental results, but they require several computational grid nodes compared to k–ε model.

As the above survey shows, the present work is based on the k–ω (SST) model by **Menter [24].** The k–ω based Shear-Stress-Transport (SST) model was designed to give highly accurate predictions of the onset and the amount of flow separation under adverse pressure gradients by the inclusion of transport effects into the formulation of the eddy-viscosity and results in a major improvement in terms of flow separation predictions.

3D incompressible steady-turbulent simulations are carried out to predict the flow fields using the CFD code (Fluent 6.3). The conservative form of the governing equations can be written in the Cartesian tensor notation as:

The mass conservation,

$$\frac{\partial u_i}{\partial x_i} = 0 \tag{2.3}$$

The momentum conservation,

$$\frac{\partial}{\partial x_j}\left(\rho u_i u_j\right) = -\frac{\partial p}{\partial x_i} + \frac{\partial}{\partial x_j}\left(\left(\mu + \mu_t\right)\left(\left(\frac{\partial u_i}{\partial x_j} + \frac{\partial u_j}{\partial x_i}\right) - \frac{2}{3}\frac{\partial u_k}{\partial x_k}\right)\right) \tag{2.4}$$

The energy conservation,

$$\frac{\partial}{\partial x_j}\left(\rho u_i c_p T\right) = \frac{\partial}{\partial x_i}\left(\left(\lambda + \frac{c_p \mu_t}{\mathrm{Pr}_t}\right)\frac{\partial T}{\partial x_i}\right) + S_T \tag{2.5}$$

Where the turbulent Prandtl number Pr_t is 0.85, and S_T represents the source term.

The viscous forces in present study are very important, so the flow is considered highly sheared, the flowing two equation of turbulent kinetic energy and dissipation rate

The Turbulent kinetic energy,

$$\frac{\partial}{\partial x_i}\left(\rho u_i k\right) = \tau_{ij}\frac{\partial u_i}{\partial x_j} - \beta^* \rho \omega k + \frac{\partial}{\partial x_j}\left(\left(\mu + \sigma_k \mu_t\right)\frac{\partial k}{\partial x_j}\right) \tag{2.6}$$

The Dissipation rate,

$$\frac{\partial}{\partial x_i}\left(\rho u_i \omega\right) = \frac{\gamma}{v_t}\tau_{ij}\frac{\partial u_i}{\partial x_j} - \beta \rho \omega^2 + \frac{\partial}{\partial x_j}\left(\left(\mu + \sigma_\omega \mu_t\right)\frac{\partial \omega}{\partial x_j}\right) + 2\left(1 - F_1\right)\rho \sigma_{\omega 2}\frac{1}{\omega}\frac{\partial k}{\partial x_j}\frac{\partial \omega}{\partial x_j} \tag{2.7}$$

Each constant of the Menter's model is computed by a blend from the corresponding constants of the $k-\varepsilon$ model and the $k-\omega$ model as: $\phi = F_1\phi_1 + \left(1 - F_1\right)\phi_2$.

Constants for this model are,

$$\sigma_{k1} = 0.85, \ \sigma_{\omega 1} = 0.5, \ \beta_1 = 0.0750, \ a_1 = 0.31, \ \beta^* = 0.09, \ \kappa = 0.41 \ , \ \gamma_1 = \beta_1 / \beta^* - \sigma_{\omega 1}\kappa^2 / \sqrt{\beta^*}$$

$$, \ \sigma_{k2} = 1, \ \sigma_{\omega 2} = 0.856, \ \beta_2 = 0.0828, \ \gamma_2 = \beta_2 / \beta^* - \sigma_{\omega 2}\kappa^2 / \sqrt{\beta^*} \ .$$

With the following definitions:

$$\tau_{ij} = \mu_t\left(\frac{\partial u_i}{\partial x_j} + \frac{\partial u_j}{\partial x_i} + \frac{2}{3}\frac{\partial u_k}{\partial x_k}\delta_{ij}\right) - \frac{2}{3}\rho \kappa \delta_{ij} \tag{2.8}$$

And $\mu_t = \dfrac{\rho a_1 \kappa}{Max\left(a_1\omega, \sqrt{2}S_t F_2\right)}$ \hfill (2.9)

Where the modulus of the mean rate-of-strain tensor S_t is defined as $S_t = \sqrt{2S_{ij}S_{ij}}$, with

$$S_{ij} = \frac{1}{2}\left(\frac{\partial u_i}{\partial x_j} + \frac{\partial u_j}{\partial x_i}\right) \tag{2.10}$$

$$F_1 = \tanh\left[\left[\min\left(\max\left(\frac{\sqrt{k}}{0.09\omega y}; \frac{500\nu}{y^2\omega}\right); \frac{4\rho\sigma_{\omega 2}k}{\Psi y^2}\right)\right]^4\right] \tag{2.11}$$

Where y is the distance to the next surface, the eddy viscosity is defined as $\nu_t = \dfrac{a_1 \kappa}{\max(a_1 \omega, \Omega F_2)}$

, Ψ is the positive portion of the cross-diffusion term of the eq. (2.11) defined by eq. (2.12),

Ω is the absolute value of the vorticity, and the blending function F_2 is given by eq.(2.13):

$$\Psi = \max\left(2\rho\sigma_{\omega 2} \frac{1}{\omega} \frac{\partial k}{\partial x_j} \frac{\partial \omega}{\partial x_j} ; 10^{-20} \right) \qquad (2.12)$$

$$F_2 = \tanh\left[\max\left(2\frac{\sqrt{k}}{0.09\omega y} ; \frac{500\nu}{y^2 \omega} \right) \right]^2 \qquad (2.13)$$

The turbulent Prandtl numbers σ_k and σ_ω, respectively, for k and ω are calculated using the

following formulas,

$$\sigma_k = \frac{1}{\dfrac{F_1}{\sigma_{k1}} + \dfrac{(1-F_1)}{\sigma_{k1}}} \qquad (2.14)$$

$$\sigma_\omega = \frac{1}{\dfrac{F_1}{\sigma_{\omega 1}} + \dfrac{(1-F_1)}{\sigma_{\omega 1}}} \qquad (2.15)$$

2.3. The source term and boundary conditions

2.3.1. The source term

Modes of heat transfer of studied domain are presented in the figure 2.4. The energy

balance at the outer surface of the pipe can be written as:

$$-\lambda_w A_o \frac{\partial T}{\partial n}\bigg|_{outer\ pipe\ \textbf{surface}} = \alpha_a \boldsymbol{q} \cdot A_o - \frac{A_o \sigma\left(T_o^4 - T_g^4\right)}{\dfrac{1}{\varepsilon_a} + \dfrac{(1-\varepsilon_g)}{\varepsilon_g}\left(\dfrac{D_o}{D_g}\right)}, \qquad (2.16)$$

n being the normal to the outer surface of the pipe A_o and σ the Stefan–Boltzmann constant.

The left hand side represents the heat flux diffusion through the absorber pipe wall.

q Being the heat flux density distribution on the outer surface of the absorber (discussed hereafter in section 2.3.2) which represents the direct solar radiations reflected by the PTC mirror, decreasing by τ_g when they cross the glass envelope and hit the absorber pipe. Thus, the first part of the right hand side represents the direct solar radiations reflected by the PTC mirror and absorbed by the selective coating of the pipe tube.

The second part of the right hand side represents the radiative heat flux between two isothermal grey and concentric pipes **(Modest [25])** that occurs between the outer surface of the absorber pipe that can reach higher temperature and the inner surface of the glass envelope as infrared radiation.

The CFD code Fluent 6.3 does not support this form of boundary condition; to overcome this problem, equation (2.16) will be subdivided into two parts **[26, 27].**

The first part takes the form: $-\lambda_w \dfrac{\partial T}{\partial n}\Big|_{outer\ pipe\ \text{surface}} = \alpha_a \cdot \boldsymbol{q}$, represents the diffusion of the concentrated heat flux $\boldsymbol{q}$ through the solid wall. The second part, accounted for heat losses, can be considered as a (negative) source term in the local (solid) energy equation. It takes the form:

$$S_T = -\frac{\sigma A_o \left(T_o^4 - T_g^4\right)}{\dfrac{1}{\varepsilon_a} + \dfrac{\left(1-\varepsilon_g\right)}{\varepsilon_g}\left(\dfrac{D_o}{D_g}\right)}\left(\frac{1}{V_w}\right) \tag{2.17}$$

$V_w = \dfrac{\pi}{4}\left(D_o^2 - D_i^2\right)\cdot z_a$ being the pipe wall volume.
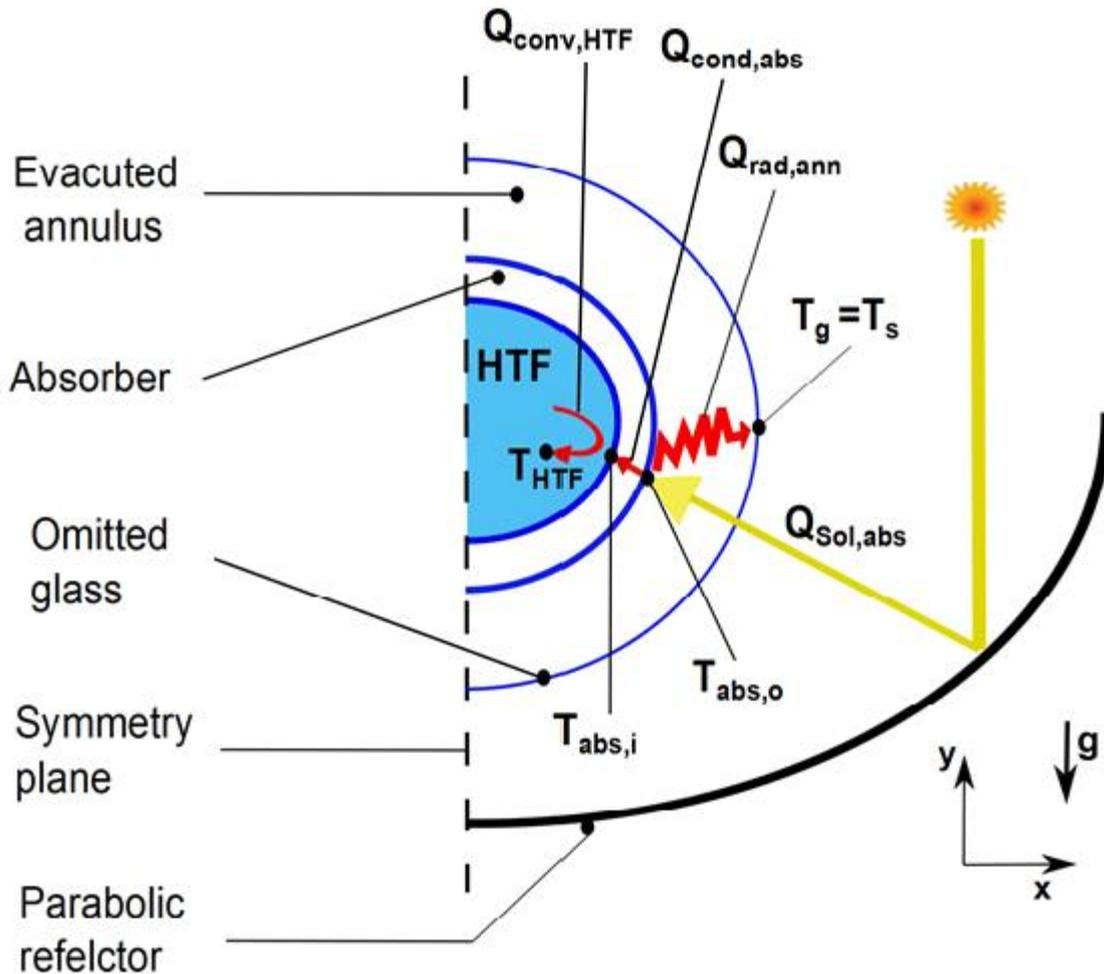
Figure 2.4: Receiver tube heat transfer models.

2.3.2. The heat flux density distribution

The specifications of the parabolic trough reflector assumed in this study **[1]** are a rim angle of 70°, an aperture width of 5 m, a focal length of 1.84 m, and a reflectance of mirrors of 0.93. The heat flux density distribution (**q**) on the outer surface of the S-curved/sinusoidal configuration of the absorber pipe was highlighted by adopting a coherent methodology described in the work of **Demagh et al. [2]**. The reconstituted **q** (3D nature) on the outer surface of the S-curved absorber pipe is shown in Figure 2.5(a) and that on the conventional straight one (2D nature) is shown in Figure 2.5(b). As a consequence of the longitudinally curved shape a better distribution of **q** is reached with the reduction of its circumferential gradient around the absorber pipe on almost the entire length. A conventional straight absorber, which possesses a straight centreline with a uniform y_{cs}, has an azimuthal *2D*

distribution of **q** unchanging along its length, which means that cross-sections whose centres are located at the similar y_{cs} have the analogous distribution of **q** regardless of the their location z on the absorber.
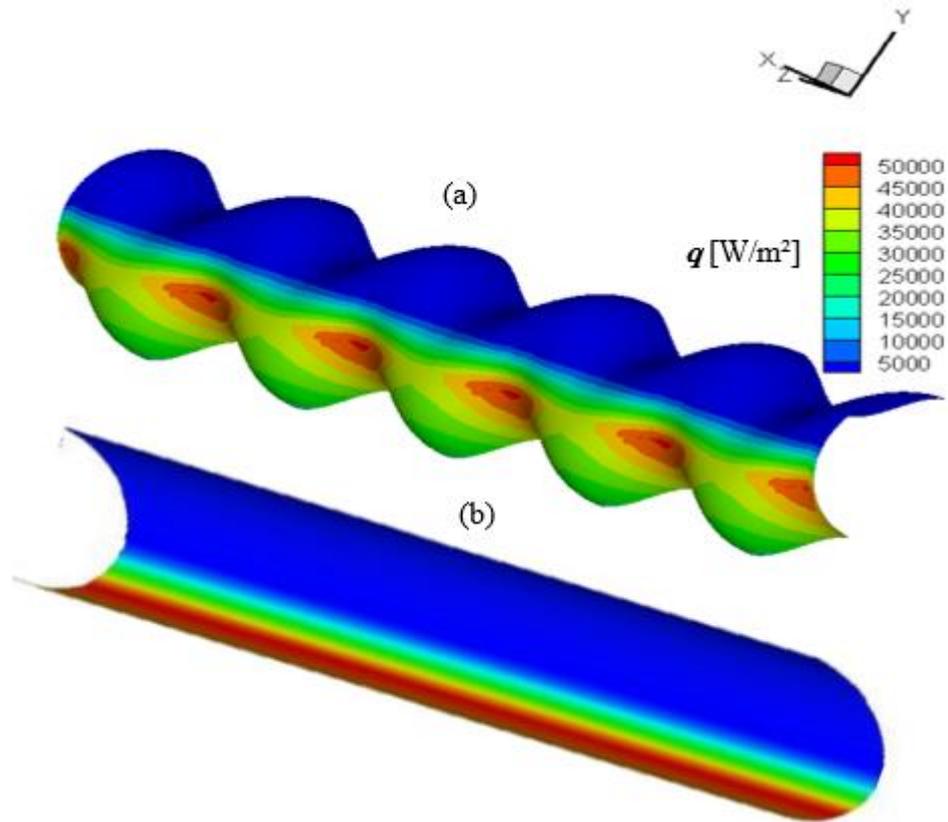
Figure 2.5 : Contours plots of the heat flux density distribution q $[Wm^{-2}]$ on the outer surface of the absorber pipe, for $q_{sun} = 933.7 \ Wm^{-2}$. (a) The novel S-curved absorber. (b) The conventional straight absorber.

As shown in Figures 2.1 and 2.2(a), as well as suggested by equation (2.1), the focal plane coincides strongly with the swept yz-plane and represents a symmetry plane. From a symmetry consideration (discussed in the subsection 2.3.3), the distribution of **q** would be displayed only on the half-pipe $(0° \leq \varphi \leq 180°)$. Moreover, the distribution of **q** is similar from a periodic segment to another along the absorber. Considering these facts, Figure 2.6(a) illustrates the heat flux density distribution (**q**) of various cross-sections of the first periodic segment; the coordinates y_{cs} and z_{cs} of the cross-section centres ranges are $0-2A$ and $\lambda-2\lambda$, respectively. The farther from $z_{cs} = \lambda \ (y_{CS} = 0)$ along the sinusoidal path until the first and bottommost bend at $z = \lambda + \lambda/2$, the more the cross-section centre moves away

from the focal line to $y_{cs} = 2A$ (see Figure 2.1), the more q is attenuated and the better it is distributed. Once the bottoms bend plane overtaken the inverse phenomenon occurs (dashed cross-section in Figure 2.6(c)) until the next bend located on the focal line at $z = 2\lambda$, and so on periodically. Cross-sections of the same colour (i.e., the same coordinate y_{cs} of the cross-section centres) in Figure 2.6(c), shown in a dashed or solid style, should have a similar distribution of q and overlap in Figure 2.6(a). Whereas for a constant y_{cs} in the case of a conventional straight absorber, Figure 2.6(b) shows a 2D character of q unchanged along the entire length. From Figures 2.6(a) and 2.6(b), the extra area exposed to the concentrated solar radiation on the novel absorber is about $30°$ larger than on the former, consequence of the wavy shape of the absorber. In fact, $30°$ concerns only the half-pipe, thus for the entire pipe the exposed area of the concentrated solar radiation should be $\simeq 60°$ larger than for the former on several locations.
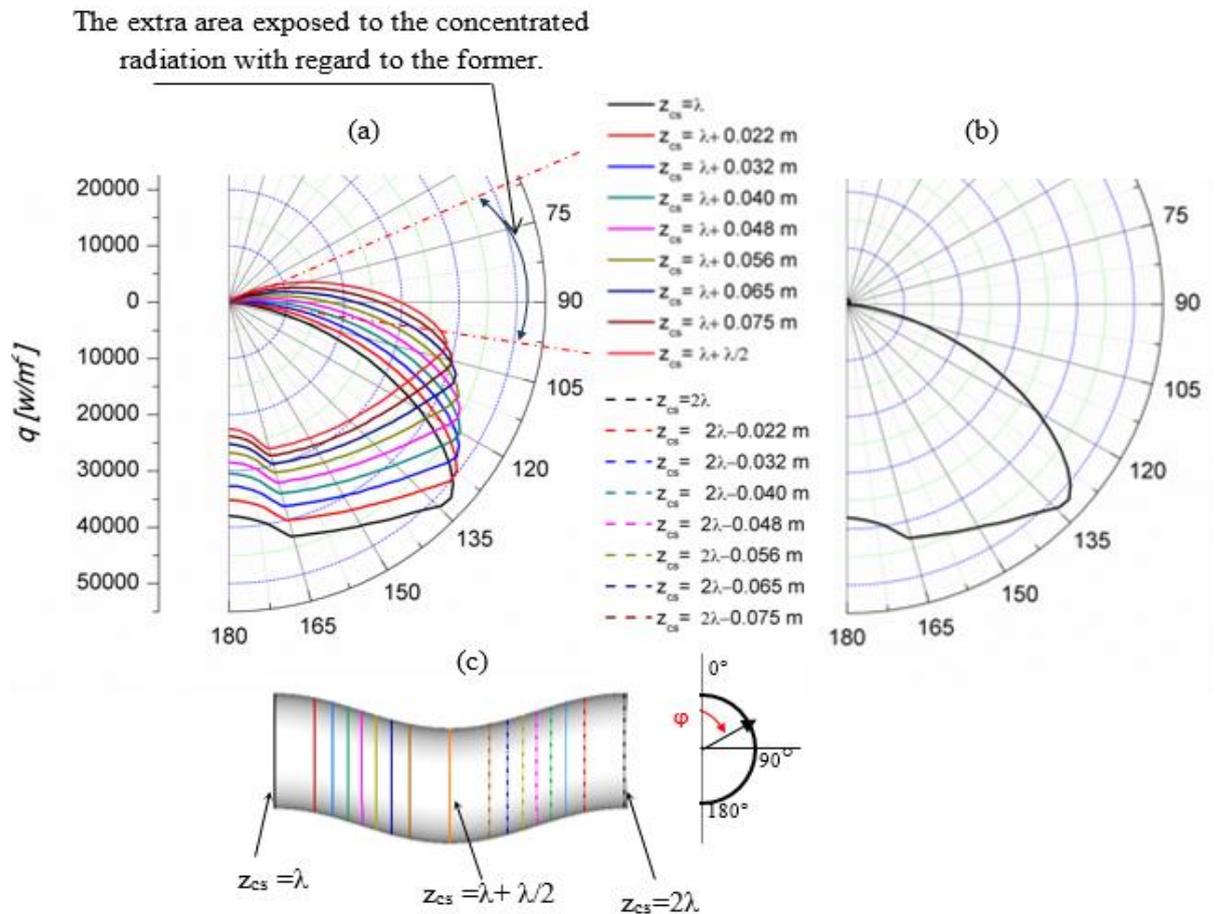

Figure 2.6 : Polar charts of q vs φ. (a) On a periodic segment of the novel S-curved pipe. (b) On the conventional straight absorber. (c) Cross-sections where the heat flux distributions (q) are extracted.

The first advantage of the novel absorber is a better distribution on a larger surface what leads to the quasi-disappearance of the band with high concentrations of *q* as encountered in the conventional PTC straight absorber (red colour in Figure 2.5(b)). Polynomial functions of *q* were created for each curve using the built-in curve fitting functions in Microsoft Excel and a linear interpolation method is used to compute the *q* for any location z between two nearby polynomial functions, corresponding to two nearby cross-sections. To be used as a heat flux boundary condition on the outer surface of the S-curved/sinusoidal absorber pipe in simulations, these polynomial functions were developed as UDF.

2.3.3. Symmetric and boundary conditions

As the equation (2.1) of the sinusoidal path is a plane function, the geometry of the conceptual S-curved/sinusoidal absorber will be symmetrical with regard to yz-plane. Besides this, it is shown in subsection 2.3.2 the symmetrical nature of the heat flux density distribution in the azimuthal direction (Figures 2.5 and 2.6). Thus, only a half of the absorber pipe will be considered in this analysis and will minimize, among others, the computational efforts.

In fact, this condition is unreal, as PTCs are line focusing reflectors that concentrate sunlight on absorber pipes along their focal lines; some kind of mechanisms are employed to track the sun (single-axis tracking or two-axis tracking). As shown in Figure 2.7 for a North-South orientation of the focal line, the symmetry condition is strongly related to the location of the outer side faces of the absorber defined by the reflected solar radiation (the red arc in Figure 2.7) relative to the direction of the gravitational field vector $\left(\vec{g} \right)$.

In such situation of single-axis tracking, where the motion is from east to west around a North–South oriented axis, for specular reflectors of perfect alignment and eliminate off-axis cosine effects. There is only one situation in which it can be assumed a symmetrical condition, at solar noon, when the y-direction and the swept plane are parallel to the gravitational field vector, case showed in Figure 2.7(b). In this study, the symmetry condition is assumed.
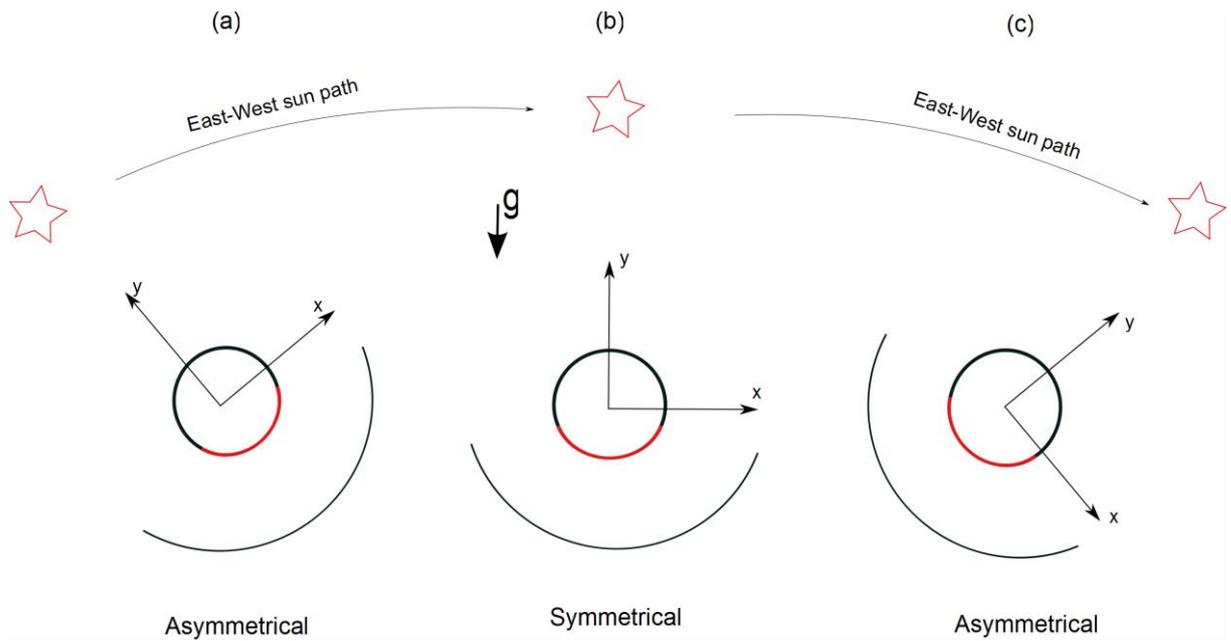
Figure 2.7 : North-South axis orientation of the trough.

The CFD code Fluent 6.3 is able to perform simulations for fully developed flow and heat transfer in periodically repeating geometry (such as the sinusoidal configurations) by means of a single periodic segment for analysis. Unfortunately, as shown in **[28],** it is not possible to use periodic boundary conditions where proprieties of the fluid are temperature-depending such for the Syltherm 800.

The specific considerations and boundary conditions accounted for in this study being:

(1) An inlet boundary condition, defined as: $\dot{m} = \dot{m}_{in}$, $T = T_{in}$, $k_{in} = \dfrac{3}{2}(u_{in} I_{in})^2$ and $\omega_{in} = k_{in}^{1/2} \big/ C_{\mu}^{1/4} l_t$, where $I_{in} = 0.16 (\text{Re}_{in})^{-1/8}$ is the turbulent intensity, $l_t = 0.07 D_i$ is the turbulent length scale and C_{μ} is an empirical constant of approximately 0.09. As the HTF proprieties are temperature-dependant, the mass flow rate (uniform at the inlet) is computed with the corresponding T_{in} .

(2) An outlet fully-developed condition.

(3) Adiabatic boundary conditions for the solid ends of the absorber pipe.

(4) The thickness of the glass envelope is considered unimportant, therefore the inner glass cover temperature is assumed even with the temperature of the sky

$$T_g = T_{sky} = T_{amb} - 8 \text{ (Forristall [29]).}$$

(5) Outer surface of the pipe coupled with the UDF of the heat flux density distribution **q**

2.4. Post processing method

The numerical results have to be processed before presentation. In the following paragraphs are discussed: The mean Nusselt number, the mean heat transfer coefficient and the Darcy (Moody) friction factor. The Reynolds number is defined as,

$$\text{Re} = \frac{\dot{m}_{in} D_i}{\mu \cdot A_{cs}} \tag{2.18}$$

The mean rate of heat transfer Q was obtained from the product of the HTF mass flow rate and the rise of the temperature, with reference to **[26, 27 and 30],** it is defined as,

$$Q = \dot{m}_{in} \left(c_{p,out} \bar{T}_{out} - c_{p,in} \bar{T}_{in} \right) \tag{2.19}$$

$c_{p,in}$ and $c_{p,out}$ are the specific heats of the HTF evaluated at $\bar{T}_{in}$ and $\bar{T}_{out}$, respectively.

$\bar{T}_{in}$ and $\bar{T}_{out}$ are mass-weighted integral temperatures computed as,

$$\bar{T} = \frac{1}{\int \rho dA} \int T \rho dA \tag{2.20}$$

dA being an elemental area of the inlet (or outlet) cross-section.

The arithmetic mean of the inlet and the outlet bulk temperatures of the HTF being T_{mf} ,

$$T_{mf} = \left(\bar{T}_{in} + \bar{T}_{out} \right) / 2 \tag{2.21}$$

The heat transfer coefficient was obtained using the wall to bulk mean temperature difference; thus the mean heat transfer coefficient and the mean Nusselt number are given by,

$$h = \frac{Q}{A_i \left(\overline{T}_w - T_{mf} \right)} \tag{2.22}$$

$$Nu = \frac{h.D_i}{\lambda} \tag{2.23}$$

λ is the HTF thermal conductivity evaluated at the film temperature $T_f = \left(\overline{T}_w + \overline{T}_{in} \right)/2$. While $\overline{T}_w$ being an area-weighted average integral temperature computed as well as the wall shear stress $\overline{\tau}_w$ on the inner wall pipe, respectively,

$$\overline{T}_w = \frac{1}{A_i} \int T_w dA \text{ and } \overline{\tau}_w = \frac{1}{A_i} \int \tau_w dA \tag{2.24}$$

dA being an elemental area of the pipe inner wall.

The Darcy (Moody) friction factor is defined as:

$$f = \frac{8\overline{\tau}_w}{\rho U_{in}^2} \tag{2.25}$$

Conclusions

This chapter presented the experimental works by **Abou-Arab et al. [10]** and **Yang et al. [11], [12]** studying friction through longitudinally curved pipes with sinusoidal shapes. The schematic and main characteristics of the S-curved sinusoidal tube and the novel PTC S-curved HCE are discussed thoroughly. The geometrical and optical characteristics of the absorber under consideration in this study have been inspired from SEGS LS2 absorber tube for scale and comparison purposes. From existing studies including **Di Piazza and Ciofalo [23]**, the k–ω based Shear-Stress-Transport (SST) model by **Menter [24]** showed great flow separation predictions, therefore it has been adopted in this study and implicated equations have been presented.

The novel PTC S-curved HCE geometry acceptance for symmetry considerations in combination with considered assumptions allow studying only half of the geometry. The UDF developed by **Demagh et al. [2]** has been presented, it showed the non-uniform heat distribution azimuthally and longitudinally, the UDF will be used in this study as boundary condition, and it is considered not depending to the thermo-dynamic parameters. In addition, the boundary conditions of the studied domain have been included. Finally, appropriate formulas and methods to post process obtained results are reported.

References

[1] V. Dudley, G. Kolb, M. Sloan, D. Kearney, SEGS LS2 solar collector-test results, Tech. Report of Sandia National Laboratories SANDIA-94-1884, 1994.

[2] Y. Demagh, I. Bordja, Y. Kabar, H. Benmoussa, A design method of an S-curved parabolic trough collector absorber with a three dimensional heat flux density distribution, Sol Energy 122 (2015) 873–884

[3] J. Eustice, Experiments of streamline motion in curved pipes, Proc. R. Soc. London A85 (1911) 119–131.

[4] S. Vashisth, V. Kumar, K. D. P. Nigam, A Review on the Potential Applications of Curved Geometries in Process Industry, Ind. Eng. Chem. Res. 47 (2008) 3291-3337.

[5] R. Yang, S.F. Chang, A Numerical study of fully developed laminar flow and heat transfer in a curved-pipe with arbitrary curvature ratio, Int. J. Heat Fluid Flow 14(2) (1993) 138-145.

[6] R. Yang, S.F. Chang, Combined free and forced convection for developed flow in curved-pipe with finite curvature ratio, Int. J. Heat Fluid Flow 15(6) (1994) 470–476.

[7] G. Yang, F. Dong, M.A. Ebadian, Laminar forced convection in a helicoidal pipe with finite pitch, Int. J Heat Mass Transfer 38 (1995) 853–62.

[8] G. Yang, M.A. Ebadian, Turbulent forced convection in a helicoidal pipe with substantial pitch, Int. J Heat Mass Transfer 39 (1996) 2015–2022.

[9] M. Di Liberto, M. Ciofalo, A study of turbulent heat transfer in curved pipes by numerical simulation, Int. J. Heat Mass Transfer 59 (2013) 112–125.

[10] T.W. Abou-Arab, T.K. Aldoss, A. Mansour, Pressure drop in alternating curved tubes, Applied Scientific Research 48 (1991) 1-9.

[11] R. Yang, F.P. Chiang, An experimental heat transfer study for periodically varying-curvature curved-pipe, Int. J. Heat Mass Transfer 45 (2002) 3199–3204.

[12] R. Yang, S.F. Chian, W. Wu, Flow and heat transfer in a curved pipe with periodically varying curvature, Int. Commun. Heat Mass Transfer 27 (2000) 133–43.

[13] N.R. Rosaguti, D.F. Fletcher, B.S. Haynes, Laminar flow and heat transfer in a periodic serpentine channel with semi-circular cross-section, Int. J. Heat Mass Transfer 49 (2006) 2912–2923.

[14] N.R. Rosaguti, D.F. Fletcher, B.S. Haynes, Low-Reynolds number heat transfer enhancement in sinusoidal channels, Chemical Engineering Science 62 (2007) 694-702.

[15] Y.L. He, J. Xiao, Z.D. Cheng, Y.B. Tao, A MCRT and FVM coupled simulation method for energy conversion process in parabolic trough solar collector, Renew Energy 36 (2011) 976–985.

[16] Z.D. Cheng, Y.L. HE, F.Q. Cui, Numerical study of heat transfer enhancement by unilateral longitudinal vortex generators inside parabolic trough solar receivers, Int. J. Heat Mass Transfer 55 (2012) 5631–5641.

[17] C.X. Lin, M.A. Ebadian, Developing turbulent convective heat transfer in helical pipes, Int. J. Heat Mass Transfer 40 (1997) 3861–3873.

[18] C.X. Lin, M.A. Ebadian, The effects of inlet turbulence on the development of fluid flow and heat transfer in a helically coiled pipe, Int. J. Heat Mass Transfer 42 (1999) 739–751.

[19] L.J. Li, C.X. Lin, M.A. Ebadian, Turbulent mixed convective heat transfer in the entrance region of a curved pipe with uniform wall temperature, Int. J. Heat Mass Transfer 41 (1998) 3793–3805.

[20] S.Y. Wu, S.J. Chen, Y.R. Li, L.J. Li, Numerical investigation of turbulent flow heat transfer and entropy generation in a helical coiled tube with larger curvature ratio, Heat Mass Transfer 45 (2009) 569–578.

[21] J.S. Jayakumar, S.M. Mahajani, J.C. Mandal, K.N. Iyer, P.K. Vijayan, CFD analysis of single-phase flows inside helically coiled tubes, Computers and Chemical Engineering 34 (2010) 430–446.

[22] S.S. Pawar, V.K. Sunnapwar, Experimental and CFD investigation of convective heat transfer in helically coiled tube heat exchangers, Chemical engineering research and design 92 (2014) 2294–2312.

[23] I. Di Piazza, M. Ciofalo, Numerical prediction of turbulent flow and heat transfer in helically coiled pipes, Int. J. Therm. Sci. 49 (2010) 653–663.

[24] F.R. Menter, Two-equation eddy-viscosity turbulence models for engineering applications, AIAA J. 32 (1994) 269–289.

[25] M.F. Modest, Radiative heat transfer, 2nd Ed., New York Academic Press; 2003.

[26] W.Q. Tao, Numerical Heat Transfer, 2nd Ed., Xi'an Jiaotong University Press, Xi'an, 2001.

[27] Z.D. Cheng, Y.L. He, F.Q. Cui, R.J. Xu, Y.B. Tao, Numerical simulation of a parabolic trough solar collector with nonuniform solar flux conditions by coupling FVM and MCRT method, Solar Energy 86 (2012) 1770–1784.

[28] ANSYS CFX Release 11 User Manual

[29] R. Forristall, Heat transfer analysis and modeling of a parabolic trough solar receiver implemented in engineering equation solver, National Renewable Energy Laboratory, 2003.

[30] Y.B. Tao, Y.L. He, Numerical study on coupled fluid flow and heat transfer process in parabolic trough solar collector tube, Solar Energy 84 (2010) 1863–1872.

Chapter 3:Models validation, Results and Discussions

Introduction

Syltherm 800 is used as the silicone HTF. Thermodynamic and transport properties of the HTF are temperature-dependent and are summarised in Table 3.1 over the temperatures range 373.15 - 673.15 K [1]. Piecewise linear functions composed of straight-line sections are used to compute HTF proprieties at various temperatures.

Over the Reynolds number range, the flow is assumed as turbulent fully developed; the length of the computational domain equals $z_a = 975\ mm$, which includes five periodic segments, the rest of the geometric characteristics are summarised in Tables 2.1 and 2.2. The stainless-steel was used as the material for the PTC absorber pipe with a thermal conductivity of $\lambda_w = 54\ Wm^{-1}K^{-1}$ [2].

The correlations by **Abou-Arab et al. [3]** and **Yang et al. [4]** for friction, and **Rogers and Mayhew [5]** for Nusselt will be used to check the consistency of obtained friction and Nusselt by comparison as varying the mesh density and the distance y+.

The results of friction and Nusselt vs Reynolds, contours of streamlines and temperature distribution, effect of varying the inlet temperature and mass flow rate and other graphs will be plotted and interpreted.

The circumferential temperature changes, local Nusselt and normalised Nusselt will be also presented and commented.

3.1. Grid independence tests and validation of the numerical models

The commercial code Fluent 6.3 was used to carry out all simulations. The code employs a coupled technique, which solves at the same time all the transport equations in the solid and the fluid domains. The computational domain is generated by Gambit 2.2.30 and showed in Figure 3.1. It was meshed using tetrahedral elements with a structured mesh into the absorber pipe wall and an unstructured (tetra/mixed) non-uniform grids within it. The

magnification of the wall to fluid edge is shown in Figure 3.1 (detail A). During the meshing process, more nodes are placed inside the viscous sub-layer to capture the high resolution of gradients in the near wall region and to ensure the satisfaction of the $y^+ < 1$ requirement at the first grid point close to the wall. The generated computational mesh totalises about 2.3 to 3.6 million elements refined into the boundary layer zone. A second order scheme was used to solve the finite difference equations. The SIMPLE algorithm is used for solving the pressure-velocity linked equation. The convergence criteria were set less than 10^{-4} for all variables except for the energy equation where the value of 10^{-6} was adopted.

To validate the numerical results, a comparison with experimental correlations of the literature was performed. **Abou-Arab et al. [3]** and **Yang et al. [4]** studied similar configurations, longitudinally sinusoidal pipes. Main characteristics of the laboratory scale pipe considered in the present study for validation purpose are: an inner diameter $D_i = 8\ mm$, a peak-to-peak amplitude $2A = 47\ mm$, a periodicity length $\lambda = 306.5\ mm$ and a total straight length equals $z_a = 919.5\ mm$.
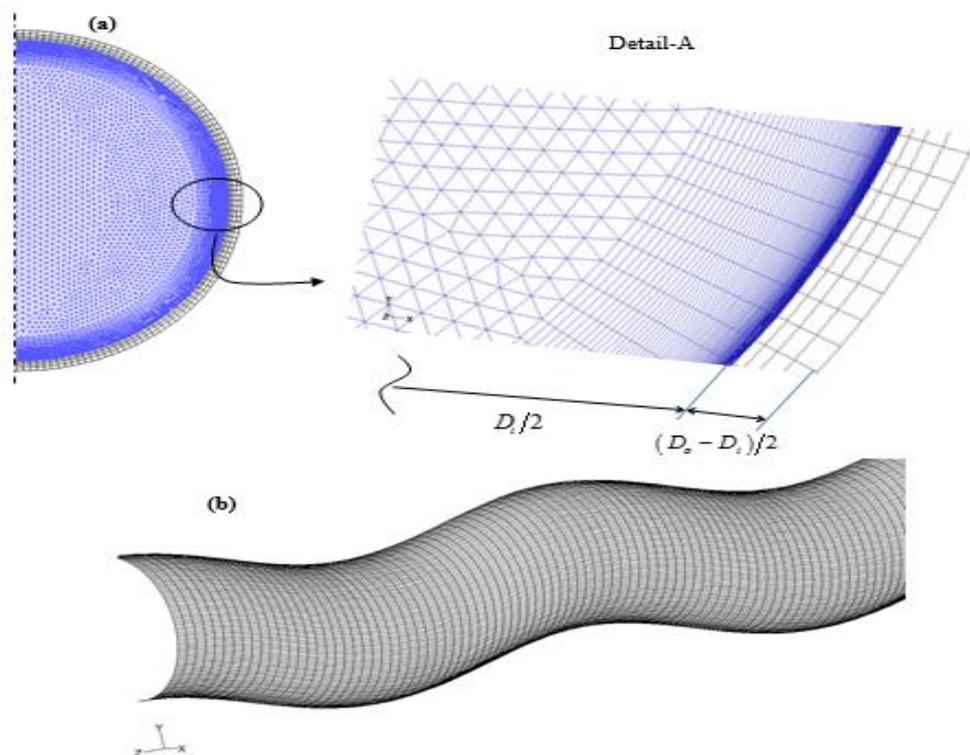

Figure 3.1 : Typical meshing generated by GAMBIT 2.2.30. (a) The cross-section view and (b) portion of the inner wall meshing.

The water is used as the HTF; its thermodynamic and transport properties are temperature-dependent and are summarised in Table 3.1 over the temperature range 305-320 K **[6]**. Piecewise linear functions composed of straight-line sections are used to calculate the HTF proprieties at various temperatures.

Table 3. 1 : HTF properties **[1, 6]**

Water				
	<u>305 K</u>	<u>310 K</u>	<u>315 K</u>	<u>320 K</u>
Density (kg/m3)	995.025	993.05	991.08	989.12
Dynamic viscosity (Pa.s)	769×10^{-6}	695×10^{-6}	631×10^{-6}	577×10^{-6}
Thermal conductivity (W/m.K)	0.620	0.628	0.634	0.640
Specific heat (J/kgK)	4,178	4,178	4,179	4,180
Syltherm 800				
	<u>400 K</u>	<u>500 K</u>	<u>600 K</u>	<u>650 K</u>
Density (kg/m3)	840	746	638	578
Dynamic viscosity (Pa.s)	2164×10^{-6}	816×10^{-6}	386×10^{-6}	283×10^{-6}
Thermal conductivity (W/m.K)	0.1148	0.0958	0.077	0.0678
Specific heat (J/kgK)	1791.64	1964.47	2135.3	2218.65

Noticed firstly by **Eustice [7]** in 1911, the critical Reynolds number for the laminar to turbulent transition in curved pipe is a function of the curvature ratio δ defined as the ratio of pipe radius and the curvature radius, $\delta = {D_{in}}\big/{2 \cdot R_{cur}}$. The critical Reynolds number reported in Table 3.2 may be determined using equations from **[8, 9]**. Thus, over the Reynolds number range $1.8 \times 10^4 - 5.5 \times 10^4$ the flow is assumed turbulent fully developed. The inlet temperature being $T_{in} = 310\,K$.

Table 3. 2 : Critical Reynolds number.

		$\mathrm{Re}_{cr} = 2100\left(1+12\sqrt{\delta}\right)$ Srinivasan et al. [8]	$\mathrm{Re}_{cr} = 2000\left(1+13.2\delta^{0.6}\right)$ Ito [9]
Laboratory scale configuration	$\delta = 0.0395035$	7,108	5,798
Actual scale configuration	$\delta = 0.3426135$	16,850	15,883

The correlation of the Darcy friction factor f by **Abou-Arab et al. [3]** takes the form:

$$\begin{cases} f = f_{straight} + 0.0005\delta^{0.5} \\ 0.0111 \le \delta \le 0.71 \end{cases}$$
(3.1)

And by **Yang et al. [4]**,

$$\begin{cases} f = 1.69\,\mathrm{Re}^{-0.318}\,\delta^{0.329} \\ 2.1\times10^{6} \le \left(\mathrm{Re}^{2}\,\delta\right) \le 5.5\times10^{7}, \\ \quad 0.05 \le \delta \le 0.096 \end{cases}$$
(3.2)

As the curvature radius R_{cur} varies along the flow path (equation (2.2)) the expression of δ would be rather complex. To by-pass this fact, **Abou-Arab et al. [3]** fixed the curvature radius at the peak of the sinusoidal curve where it is the minimum possible. Therefore, for $z = \frac{\lambda}{2}$ the minimum curvature radius of the pipe centreline would be $R_{curv}^{\min imum} = \frac{\lambda^{2}}{4\pi^{2}A}$, the corresponding curvature ratio would be $\delta = \frac{D_{i}}{2 \cdot R_{cur}^{\min imum}}$ and should admit a unique value for every sinusoidal shape.

For comparative purposes, the smooth pipes Darcy (Moody) friction factor is given by **Petukhov's** correlation [6] as,

$$f_{straight} = \left(0.790 \cdot Ln(\mathrm{Re}) - 1.64\right)^{-2}$$
(3.3)

Table 3.3 summarises a sample of the grid independency tests that have been conducted, the solution was considered mesh independent when the change in the mean Nusselt number (equation (2.23)) and the friction factor (equation (2.25)) were less than 1.5%. From the Table 3.3, it is found that results for the global grid of 3,297,000 cells were not

affected by the refinement and represents the optimised grid. % differences represent the changes for the friction factor f from simulations. Instead of checking the grid in a comprehensive manner, each subdomain, fluid or solid, was inspected separately in the global grid; moreover, the mesh in each direction is treated independently.

Table 3. 3 : Grid independency checking.

Global grid	f	Nu	% f	% Nu
2,300,000	0,026455	174,25576		
2,437,600	0,026032	173,47160	-1.6%	-0.45
2,910,119	0,024887	177,63492	-4.4%	2.4
3,256,400	0.02526	178,61192	1.5%	0.55

Figure 3.2 presents a comparison between numerical calculations of the friction factor and experimental correlations (equations 3.1 and 3.2) and shows an excellent agreement with the experimental correlation by **Abou-Arab et al. [3]**, with a maximum relative error less than 3.9%. However, with a maximum error less than 11.8%, the correlation by **Yang et al. [4]** remains valid; over prediction remain tolerable for most engineering applications. It was also reported in Figure 3.2 a comparison between the mean Nusselt number of the present study and the experimental correlation by **Rogers and Mayhew [5]** (equation 3.4) developed for coils. Indeed, as declared by **Vashisth [10]**, the heat-transfer characteristics in serpentine configurations need to be further explored; through seen papers, there is only a single correlation of the turbulent mean Nusselt number developed by **Yang et al. [4]** for serpentine pipe and especially for sinusoidal curved-pipe. However, this correlation has not been validated or used by other scientific work for the simple reason it brings unimaginable values for the Nusselt number, e.g. for Re = 22500 we get Nu = 9074.87, much overestimated. Otherwise, for a computational domain composed of a single turn curved pipe (with a pitch zero), the numerical results of the Nusselt numbers by **Lin and Ebadian [11, 12]** and **Li et al. [13]** were validated with experimental correlation (equation 3.4) from **Rogers and Mayhew**

[5] based on water flowing through a heated curved tube. The numerical results of the present study showed good agreement, with a maximum relative error of 5.2%.

$$Nu = 0.023 \cdot \text{Re}^{0.85} \cdot \text{Pr}^{0.4} \cdot \delta^{0.1}$$ (3.4)

Where proprieties of the HTF are estimated at T_{mf}

It is important to specify that the curvature ratio δ, used in equations 3.1 and 3.2, was obtained following two distinct ways:

i) Using the computed minimum curvature radius $R_{curv}^{\min imum} \simeq 101.26\ mm$, thus the value of $\delta = 0.0395$ was utilized in the correlation (3.1) by **Abou-Arab et al. [3]**.

ii) Using an average value of $\delta = 0.05$ in equation (3.2). This value corresponds to the lower limit of the curvature ratio range in [4] which, from the experimental configuration of **[4]**, corresponds to: a curvature $\kappa = \frac{2\pi}{\lambda} = 2.05\ mm^{-1}$ (the periodicity length being $\lambda = 306.5\ mm$), an amplitude of $23.5\ mm$ and an inner pipe diameter of $D_i = 8\ mm$. The use of $R_{curv}^{\min imum}$ in equation (3.2) provided larger errors.
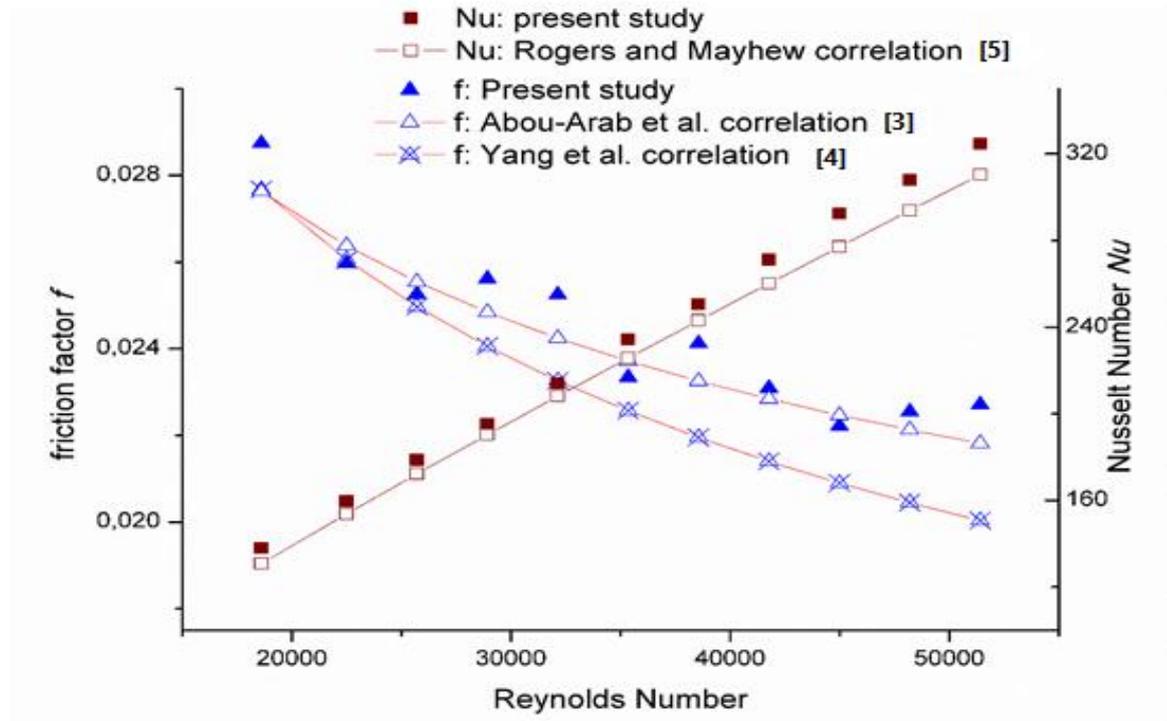

Figure 3.2 : Validation of the simulation results for a laboratory scale sinusoidal pipe.

3.2. The average Nusselt number and the friction factor

To recreate actual operating conditions of PTC plants, the Syltherm 800 inlet temperature ranges from $450\,K$ to $600\,K$, the direct solar insolation being $q_{sun} = 933.7\,Wm^{-2}$ and the ambient temperature equals to *298.15* K. For a comparison purposes, the mean Nusselt number for a smooth and straight pipe is estimated by **Gnielinski's** correlation **[6]**. It is defined as,

$$\begin{cases} Nu_{straight} = \left. \left(f_{straight}/8 \right) \left(\mathrm{Re} - 1000 \right) \mathrm{Pr} \middle/ \left(1 + 12.7 \left(f_{straight}/8 \right)^{1/2} \left(\mathrm{Pr}^{2/3} - 1 \right) \right) \right. \\ 0.5 \le \mathrm{Pr} \le 2000, \ 3.10^3 \le \mathrm{Re} \le 5.10^6 \end{cases} \quad (3.5)$$

Where $f_{straight}$ is estimated by Petukhov's correlation, equation (3.3).

Figure 3.3 illustrates the variation of the mean Nusselt number (Nu) and the mean friction factor (*f*) against the Reynolds number, which corresponds to the HTF mass flow rate range $2.0 - 9.5\,kgs^{-1}$. The inlet HTF temperature, the mean Prandtl number being $T_{in} = 450\,K$, $\mathrm{Pr} = 26.5$, respectively, and the Reynolds number range $2.5 \times 10^4 - 12.3 \times 10^4$.
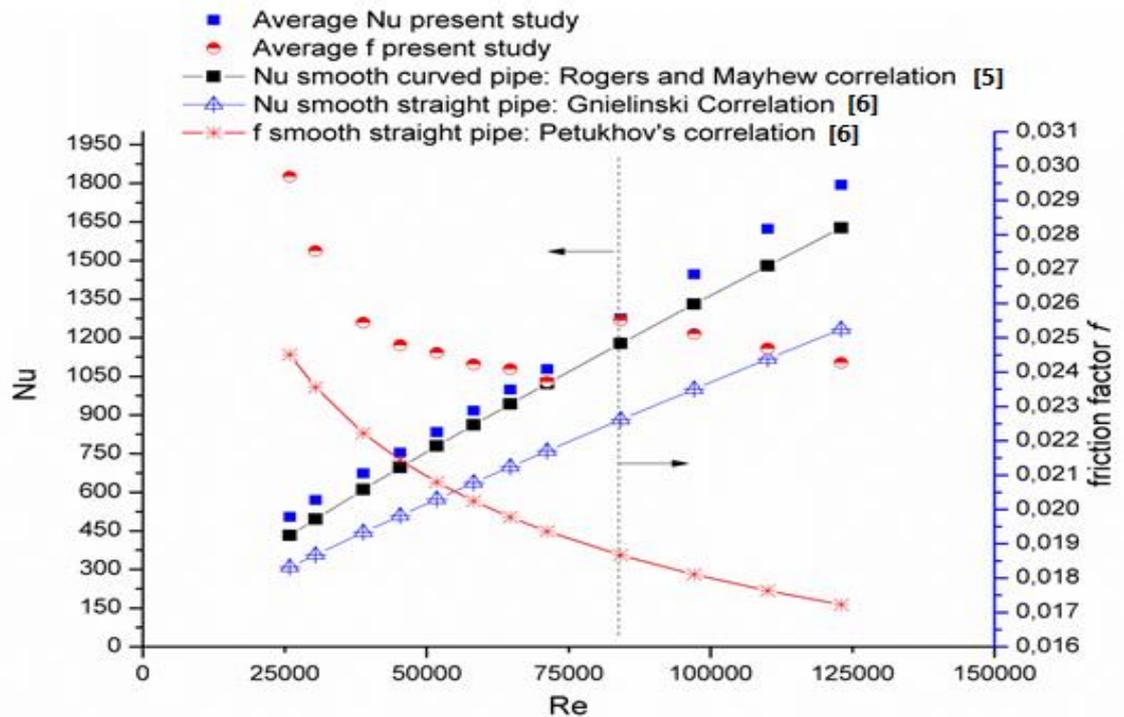

Figure 3.3 : Nu and *f* vs. the flow regime Reynolds number for $T_{in} = 450\,K$ and $q_{sun} = 933.7 Wm^{-2}$.

It is obvious that the mean Nusselt number of the S-curved absorber is higher than that of the conventional straight absorber obtained by Gnielinski's correlation, the mean Nusselt number of the S-curved absorber is improved by up to 63% as compared with the conventional straight. In addition, as expected, the enhancement of the heat transfer rate is accompanied by an increase in the friction factor, by less than 40.8%. On the other side, the comparison with the most cited correlation (equation (3.4)) by **Rogers and Mayhew [5]** shown a maximum deviation of 15%, and remains always reliable with regard to the disparities in Prandlt numbers of the original study where the authors had used water as HTF; the under prediction remains tolerable for most engineering applications, especially as the correlation was established for a fully developed flow.

3.3. Flow behavior

It is well known that curved configurations induce a secondary flow within the mainstream. Also named Dean Vortex, the induced secondary flow is due to the imbalance between the pressure force and centrifugal force generated by bends of the pipe. The secondary streaming significantly enhances the heat transfer rate and its existence has been established numerically by **Rosaguti et al. [15]** in a fully developed laminar flow within a single sinusoidal module. Figure 3.4 shows flow features at topmost and bottommost bends of the S-curved pipe for the flow regime $\mathrm{Re} \simeq 12.3 \times 10^4 \left(\dot{m}_{in} = 9.5 \ kgs^{-1}, T_{in} = 450 \ K \right)$ where corresponding xy-planes are created in the computational domain. A main cell of the reversed flow is observed in the xy-plane at the first bend; due to the symmetry of the configuration (subsection 2.3.3), only one-half of the circular cross-section was displayed. Actually, by displaying the entire circular cross-section, two symmetric reversed cells at $z = \lambda/2$, which are known as the twin Dean Vortices are observed. The symmetry with regard to the swept plane was also reported by **Yang et al. [14]** and **Rosaguti et al. [15]**. At this location, the centroid of the vortex is located near the wall; the vortex cell occupies almost all the area of the half cross-section and has a clockwise rotation. As the longitudinal location of the bend cross-section moves forwards, the intensity of the vortex increases. In all the remaining cross-sections two co-rotated vortices are present, with the upper one enlarging until it occupied the half-area and equalize the lower one. The rotating direction of the cell reverses periodically, depending

on the streaming direction, upward or downward and the reversed centrifugal force. Also, by focusing on the two last bends preceding the outlet at $\left(z=4\lambda\right)$ and $\left(z=4\lambda+\dfrac{\lambda}{2}\right)$, the similarities of the vortex cells are obvious; considering an established flow condition at the pipe outlet, the similarity is justified.

Figure 3.4 : Streamlines at xy-planes of various bends along the S-curved/sinusoidal pipe for $\dot{m}_{in}=9.5\,kgs^{-1}\left(\mathrm{Re}=12.3\times10^{4}\right)$ and $T_{in}=450\,K$. The pipe wall was omitted.

Figure 3.5 presents flow behavior through the third periodic segment $\left(2\lambda\leq z\leq3\lambda\right)$. Outside the bends the streaming is regular without any vortices as reported in Figures 3.5 (a), 3.5(b) and 3.5(c) for various HTF inlet temperatures and the same mass flow rate; such results were also observed in laminar flows as reported by **Rosaguti et al. [15]**. On the contrary, the analysis of Figure 3.5(d) reveals the existence of vortices outside bend xy-planes, and that so, they are more likely at bend xy-planes as seen previously. From Figure 3.5(d) vortices are stronger in bends then weaken as they move away from bends until almost disappear in the vicinity of the location $z=2\lambda+\dfrac{\lambda}{4}$.
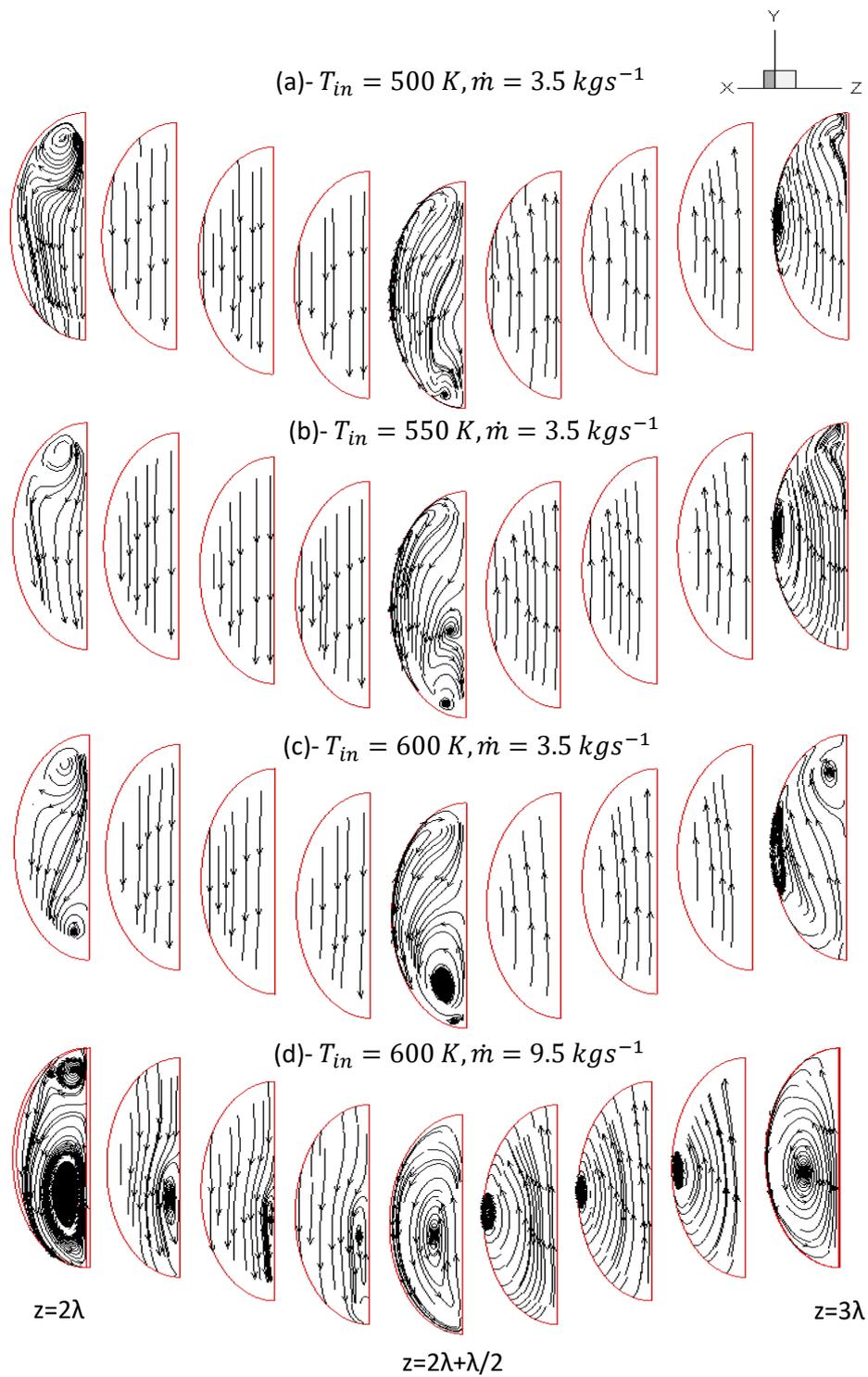
(a)- $T_{in} = 500\ K, \dot{m} = 3.5\ kgs^{-1}$

(b)- $T_{in} = 550\ K, \dot{m} = 3.5\ kgs^{-1}$

(c)- $T_{in} = 600\ K, \dot{m} = 3.5\ kgs^{-1}$

(d)- $T_{in} = 600\ K, \dot{m} = 9.5\ kgs^{-1}$

z=2λ   z=3λ

z=2λ+λ/2

Figure 3.5 : 2D-3D transition of vortices. (a) $T_{in} = 500\ K$ and $\dot{m}_{in} = 3.5\ kgs^{-1}$, which corresponds to $\mathrm{Re} \simeq 82.7 \times 10^3$, (b) $\mathrm{Re} \simeq 112.3 \times 10^3$, (c) $\mathrm{Re} \simeq 175 \times 10^3$ and (d) $\mathrm{Re} = 474.8 \times 10^3$. Only the second periodic segment was shown $\left(2\lambda \leq z \leq 3\lambda\right)$ and the pipe wall was omitted.

Actually, all these phenomena are related to the sinusoidal shape of the pipe. As suggested by the equation (2.2), the minimum R_{curv} is observed at bends $\left(z = i\,{\lambda}/{2}\;,\, i = 0,1,2,3....\right)$ and tends to infinity at $\left(z = i\,{\lambda}/{2} + {\lambda}/{4},\, i = 0,1,2,3....\right)$, which is illustrated in Figure 3.6. The curvature radius ranges from $R_{curv}^{\min imum}$ up to $R_{curv} \to \infty$ (straight shape) which correspond to the curvature ratio range $0 \leq \delta \leq {D_i}/{2R_{curv}^{\min imum}}$, where $\delta = 0$ corresponds to a straight pipe. The secondary flow develops in the cross-section of curved pipes due to the imbalance between the pressure and centrifugal forces, as long as the effect of the centrifugal force is strong. Besides, when the curvature radius raises the centrifugal force decreases and its effect would be weak to create a vortex; vortices are more likely to be generated at bend cross-sections than the other cross-sections. The higher the HTF inlet temperature increases, the more the Reynolds number grows; the centrifugal force becomes gradually more significant outside bends up to unbalance the pressure force and thus vortices are created outside the xy-plane of bends; such situation is achieved in the case of the Figure 3.5 (d) where vortices are 3D, the flow within the S-curved/sinusoidal pipe behaves like within the helically coiled pipe.
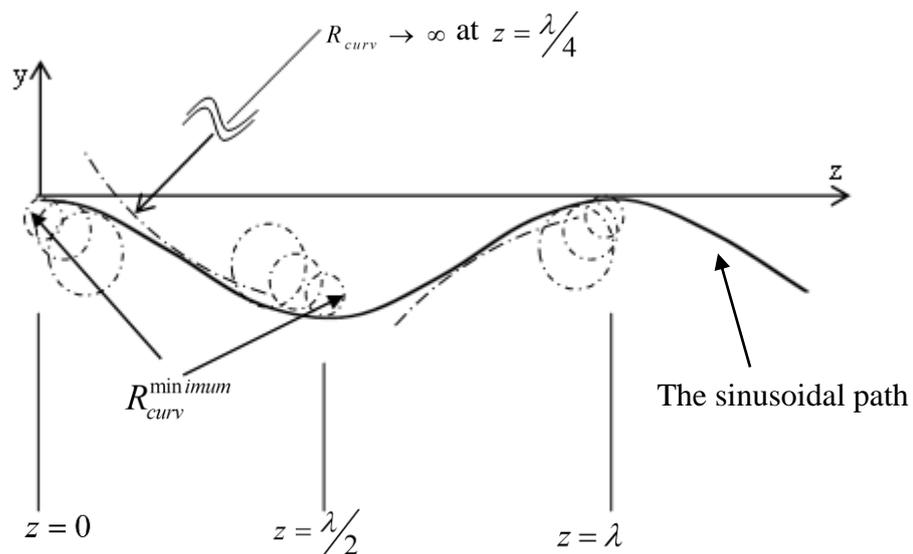

Figure 3.6 : The sinusoidal nature of the curvature radius

The flow behavior changes with Reynolds numbers is shown in Figure 3.7 at the bend xy-plane located at $z = 2\lambda + \lambda/2$. It can be seen the generation of new vortex in the vicinity of the wall which intensifies and shifts away from the wall at $Re \simeq 84160$. The emerging vortex represents a supplementary pressure drop penalty at this flow regime, which explain the sudden increase of the friction factor observed at $Re = 84160$ (see Figure 3.3). Besides, why the Nusselt number does not also show a disturbance at this flow rate? Vortex generation induces considerable fluid mixing near the surface and promotes large temperature gradient adjacent to the solid surface, and significantly increasing the heat transfer (h) and Nu. In addition, it is clear that cannot mix the liquid infinitely or still mix which is well mixed prior, and this encourages the most detailed investigations on the solid vortex generator shapes/arrangements through the various equipment looking for an optimal configuration. Now, it is logic to say that the effects of the newly generated vortex on the Nusselt number are weak at this flow regime because their effects are negligible on the mixing of the fluid, and the fact that the fluid has been already well mixed previously by the foregoing vortices.
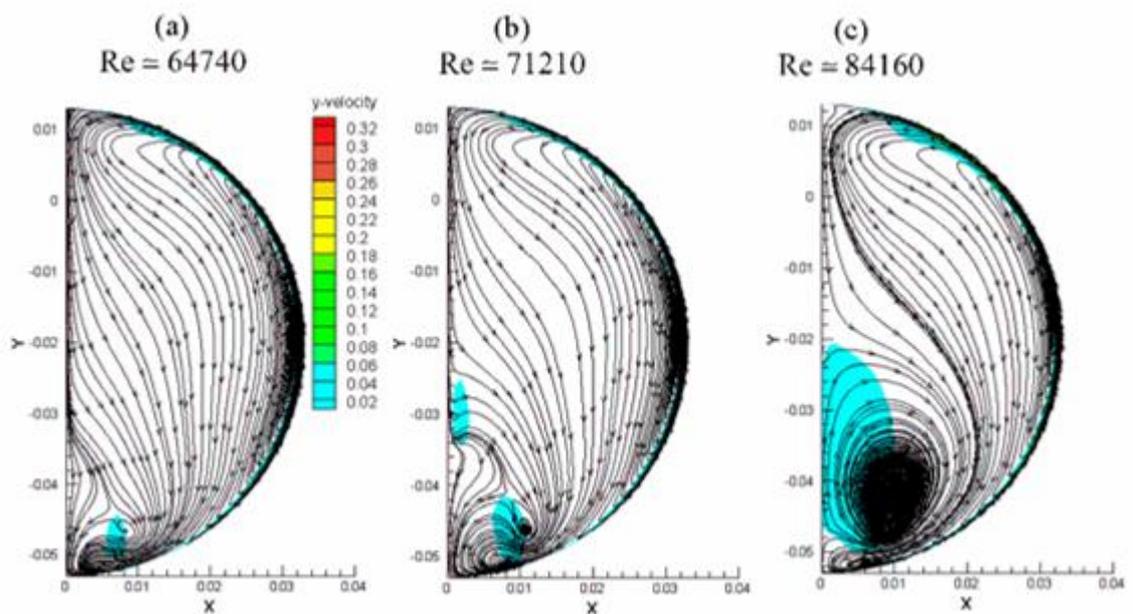

Figure 3.7 : Plots highlighting the emergence of a new vortex at $z = 2\lambda + \lambda/2$, $T_{in} = 450K$. (a) $Re \simeq 64740$, (b) $Re \simeq 71210$ and (c) $Re \simeq 84160$ which correspond, respectively, to the mass flow rates $\dot{m} = 5\ kgs^{-1}$, $\dot{m} = 5.5\ kgs^{-1}$ and $\dot{m} = 6.5\ kgs^{-1}$. Coloured zones represent the positive y-velocity contours. The pipe wall was omitted.

Figure 3.8 shows the trend of the HTF velocity magnitude V in various locations along the S-curved/sinusoidal absorber and for various mass flow rates. For better presentation, the velocity magnitude was normalised by the corresponding HTF inlet velocity as $V^* = V / u_{in}$.

From Figure 3.8, as the flow develops, the amplitudes of the velocity magnitude are attenuated; the maximum and the minimum values are reached in the vicinity of the bottommost and uppermost bends, respectively, as a result of the flow downward (acceleration) or upward (deceleration) within the S-curved pipe. The attenuation of the velocity magnitude along the streaming is certainly due to the vortices intensifications, as discussed previously. However, the peaks of the velocity are not located exactly at bends, as the figure shows, but right before.
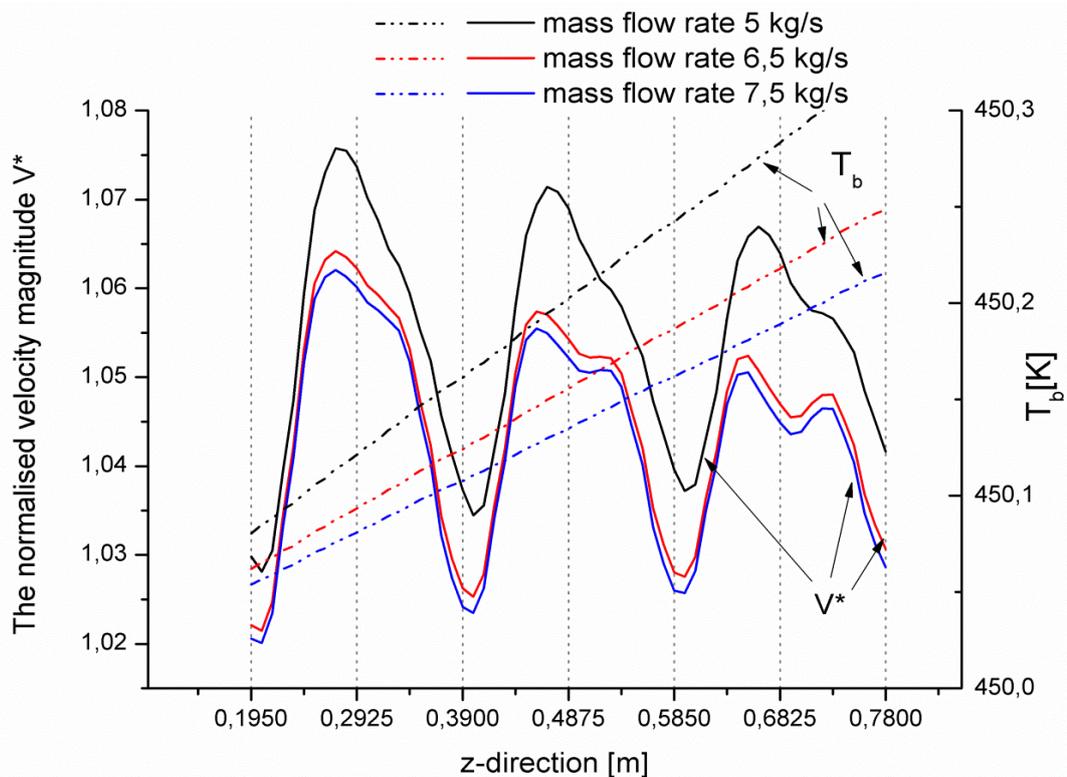

Figure 3.8 : The normalised velocity magnitudes V^* and the bulk temperatures along the absorber, for various mass flow rates at $T_{in} = 450\ K$, which correspond respectively to $\mathrm{Re} \simeq 65000$, $\mathrm{Re} \simeq 85000$ and $\mathrm{Re} \simeq 97000$.

For a pipe without vortex cells, the highest velocities (at the lowest half of the tube) would be at bends, but the appearance of the vortices in bends opposes the free streaming, the velocity magnitudes at bend xy-planes are lower (at the highest half of the tube). Besides,

it was noticed a swelling in the deceleration branch of curves that grows along the pipe. It seems that wiggles occur only in the deceleration branches and remain absent for the rest. Considering a periodic segment, the HTF absorbs much more energy from the pipe wall in the deceleration branches, as its velocity decreases. By means of this phenomenon, the HTF bulk temperature grows rapidly in deceleration branches than in acceleration branches, in Figure 3.8 the increase in temperature is not perfectly linear. Now, as the Syltherm 800 is temperature-dependent proprieties, the higher the HTF bulk temperature (see Figure 3.8), the more the HTF density decreases, the more the velocity at these regions rises to satisfy the conservation of the mass, and thus, wiggles occur.

The effects of the HTF inlet temperature on both the mean Nusselt number and the mean friction factor are shown in Figure 3.9. Due to a significant change in the properties of the HTF as the temperature increases, the Reynolds number increases also significantly for a constant mass flow rate. Thus, when the mass flow rate changes from $2\ kgs^{-1}$ to $9.5\ kgs^{-1}$, the Reynolds number varies from 2.5×10^{4} to 12.3×10^{4} at $T_{in}=450\ K$ and from 17.5×10^{4} to 47.5×10^{4} at $T_{in}=600\ K$.
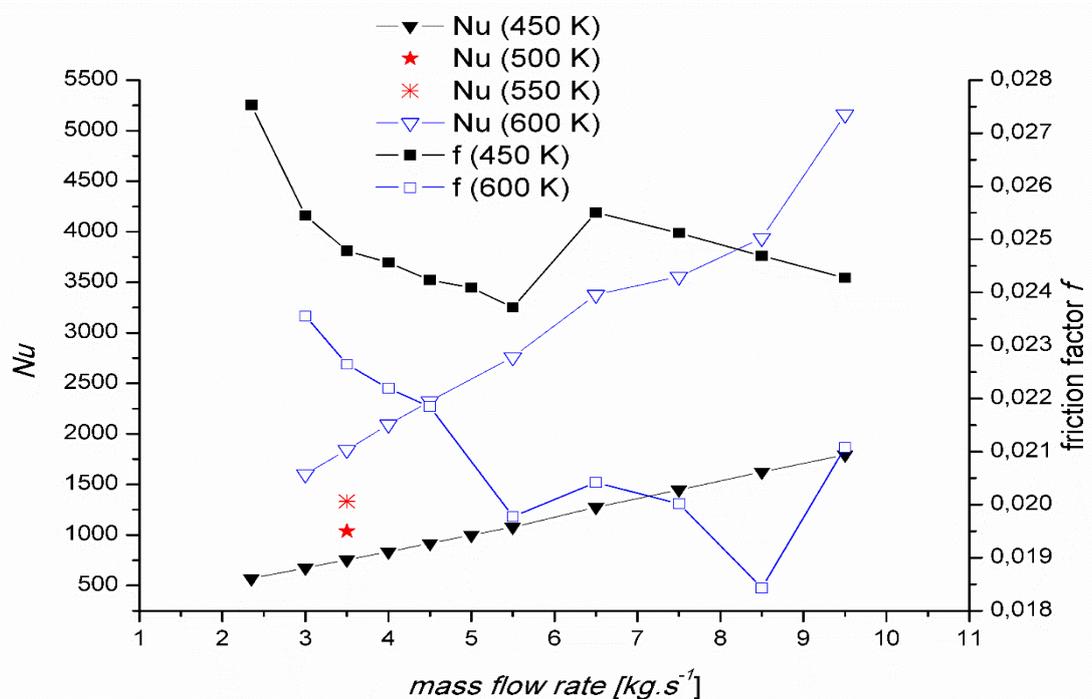

Figure 3.9 : Changes in the Nusselt number and the Friction factor for different HTF inlet temperature, against the mass flow rate.

Consequence of previous explanations and for better presentation of results for various HTF inlet temperatures, curves have been reported in Figure 3.9 against mass flow rates. The curve of the friction factor f admits a serrated shape, which is explained by the emergence of new vortices as discussed previously. However, the mean Nusselt number curve corresponding to $T_{in} = 600\ K$ seems to react to this phenomenon unlike for $T_{in} = 450K$ where it remains uniformly growing without any streaks.

Due to the improvement of the inner heat transfer and the better distribution of the external heat flux, contour plots of Figure 3.10 show the decrease of the azimuthal temperature difference between the highest and lowest temperatures of the wall of the absorber pipe. In practice, the tolerable azimuthal temperature difference in the absorber pipe operating shall be less than 50 K. For an inlet HTF temperature of $450\ K$ and a mass flow rate of $\dot{m} = 5.5\ kgs^{-1}$ corresponding to $\text{Re} = 71200$, the maximum temperature difference is about $35\ K$, the more the flow regime increases the more the temperature difference decreases below $35\ K$.

The trend of the azimuthal temperature difference in the pipe wall against the flow regime is shown in Figure 3.11. It is obvious that when the Reynolds number rises the temperature difference decreases as a consequence of the increase of the Nusselt number.

The comparison with results reported from the study of **Fuqiang et al. [16]** on a corrugated pipe PTC absorber was also reported in Figure 3.11. Although the inlet HTF temperatures are different for the two cases, $300\ K$ (Therminol D12) for **[16]** and $450\ \text{K}$ (Syltherm 800) for the present study, the gap between the curves is obvious, especially at high Reynolds numbers; for $\text{Re} \simeq 70,000$ it reaches approximately $15\ K$ and could increase if similar inlet temperatures (and similar HTF) are considered. In addition, Figure 3.11 showed the trend of the heat transfer rate Q against the Reynolds number. The increase of the heat transfer rate does not seem to be asymptotic as reported in **[16]** and remains much more significant in the present study than **[16]**, up to 1.5 times larger.
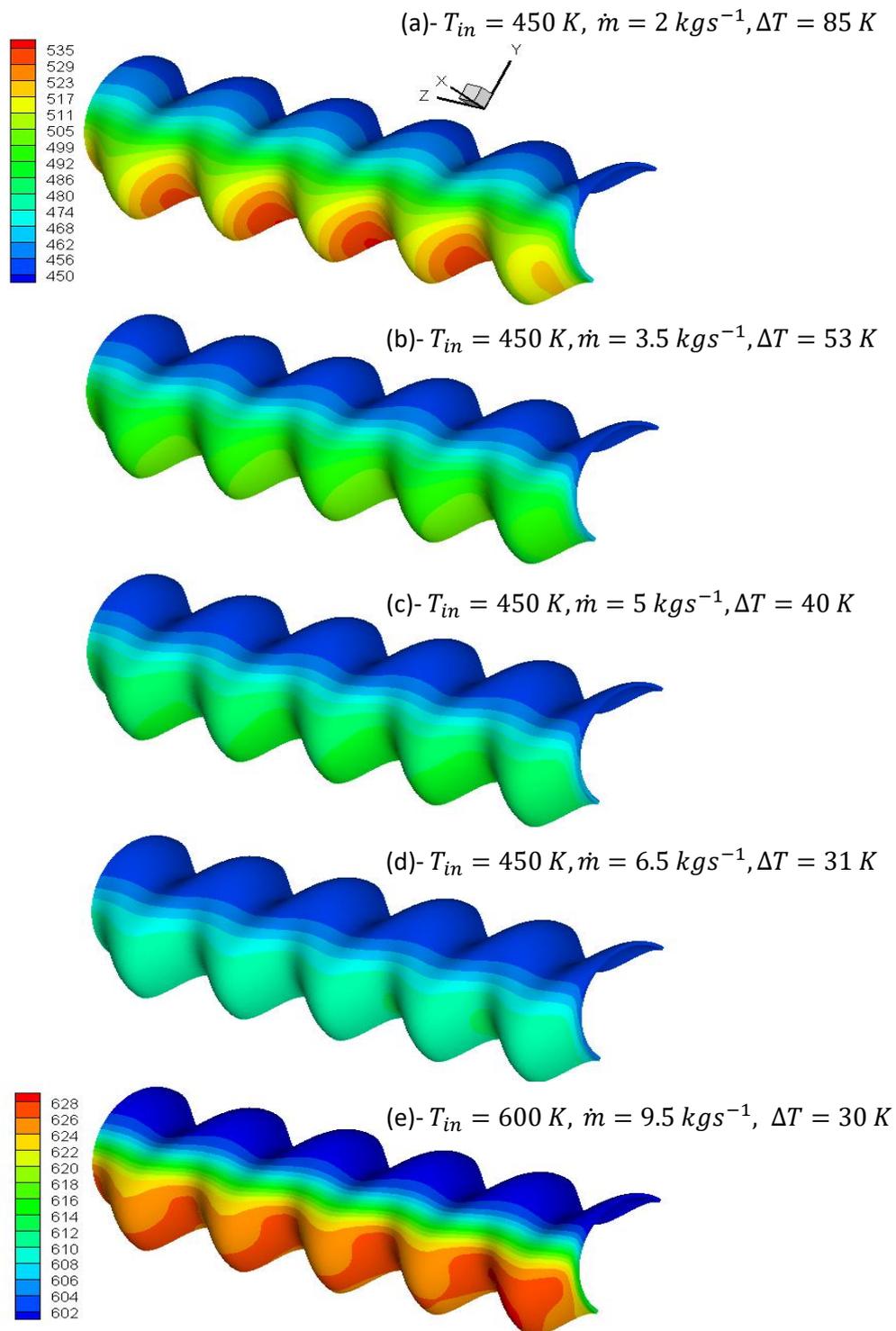
Figure 3.10 : The contour plots of the pipe-wall temperature for two inlet temperatures (450K and 600K) and various mass flow rates.
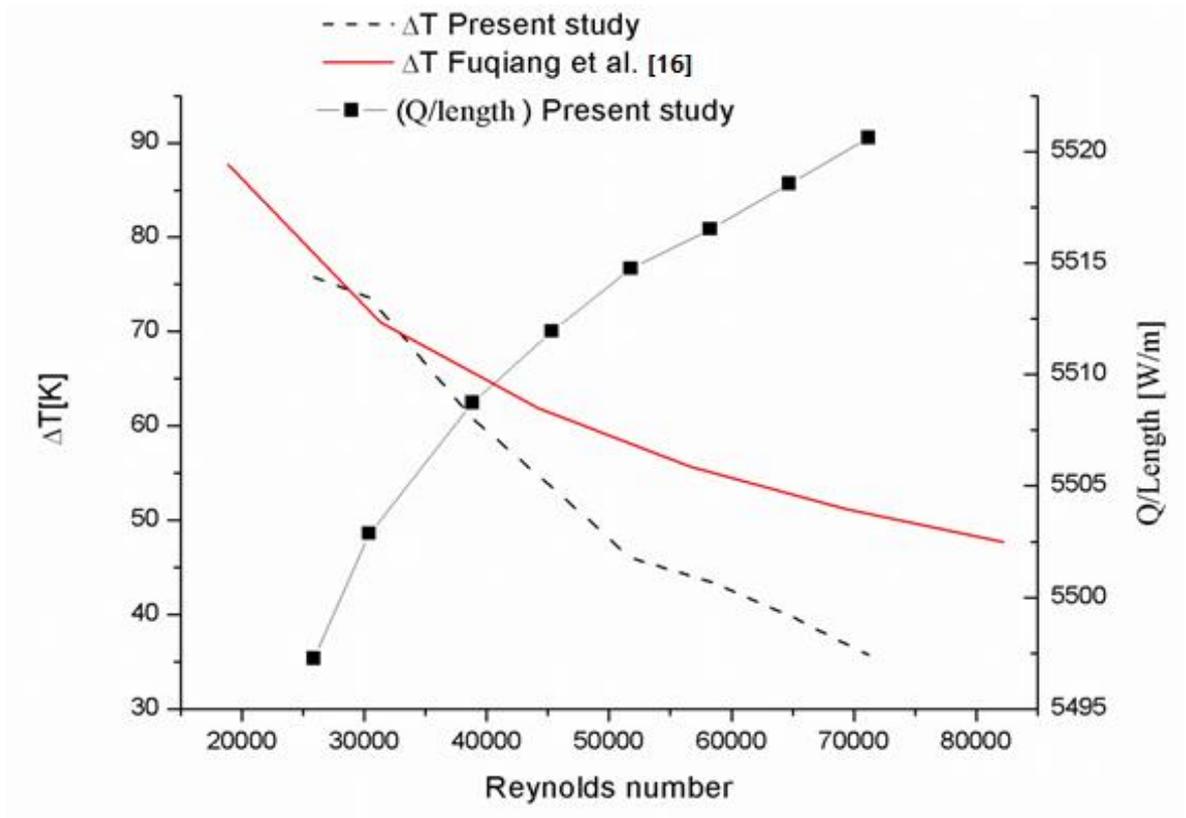
Figure 3.11 : The circumferential temperature gradient and the mean heat transfer rate per meter against Reynolds number

3.4. The local Nusselt Number

Firstly, planes are created at desired z locations in the computational domain, corresponding to the bend locations. Since the HTF properties are temperature-dependent, the bulk fluid temperature $\bar{T}_b$ at a cross-section is evaluated using equation (2.20). All the inner wall node temperatures around the circumference of cross-sections are also extracted. Using these data, local Nusselt numbers in the azimuthal direction are computed using the equation,

$$Nu_\varphi = \frac{D_i}{\lambda} \frac{q_w''}{\left(T_w - \bar{T}_b\right)} \tag{3.6}$$

T_w being the inner wall local temperature (no averaging), λ being the fluid thermal conductivity estimated at the film temperature $T_f = \left(T_w + \bar{T}_b\right)/2$ and $q_w'' = -\lambda \frac{\partial T}{\partial n}\Big|_{at\ the\ inner\ wall}$ being the inner wall local heat flux.

Figure 3.12 gives the variation of the local Nusselt number Nu_φ around the circumference of the various cross-sections of bends assuming $T_{in} = 450\,K$ and $\dot{m} = 5\,kgs^{-1}\,(\text{Re} \simeq 65000)$. Such curves resulted from combination of complex dynamic and thermal phenomena; for a better discussion of these curves, Figure 3.13 and 3.14 will be used to strengthen these explanations. Figure 3.13 displays the flow behaviors at the same conditions as in Figure 3.12 and at the same cross-sections. In addition, the contour plots of the HTF velocity, the pipe inner-wall temperature and the HTF temperature are presented respectively, in Figure 3.14(a), 3.14(b) and 3.14(c). Solid lines in Figure 3.12 characterise almost uniform rate of heat transfer around the azimuthal direction in the uppermost bends. From Figure 3.13(a), the main cells rotate clockwise; cold fluid particles in the upper region of bends (see Figure 3.14(c)) are forced by the vortex to move against the pipe wall towards the lower region and gain energy. Thus, from $\varphi = 0°$ to $\varphi = 180°$ the temperature of fluid particles increases in the same way that the inner wall temperature (see Figure 3.14(b)) and leads to almost uniform dimensionless temperature gradient $\partial T^* / \partial n^*$; $T^* = (T - T_w) / (\bar{T}_b - T_w)$ being the dimensionless temperature and n^* being the dimensionless normal direction of the inner wall. The local Nusselt number defined as $Nu_\varphi = \partial T^* / \partial n^*$ will be almost uniform at uppermost bends. Nevertheless, at the upper region, up to $\varphi = 15°$, the Nu_φ decreases rapidly due the decreased velocity magnitude in this zone (see Figure 3.14(a)) and increases again on the symmetry plane. These intensifications at the vicinity of the symmetry plane can be explained by the fact that when the hot fluid particles are transported by the streaming from the lower side regions towards the upper ones, throughout the central zone of the pipe, they cede energy to fluid particles less hot. By reaching the top side, the fluid particles temperature will approximates the wall temperature, where the wall is not heated by the concentrated solar radiations; the local Nusselt number increases. The phenomenon is intensified as the second vortex cell emerges (see Figure 3.13(a)) at the upper region of the uppermost bends.

A similar shape of the local Nusselt number was obtained by **Di Liberto and Ciofalo [17]** for a finite segment of a horizontal toroidal pipe and assuming turbulent fully developed conditions, the Nusselt number decreases continuously from the outside wall, reaching the

lowest value on the internal wall at the swept plane, and does not increase again near the swept plane, as it is noticed in the current configuration.

The secondary vortices in the bend xy-planes (see Figure 3.13) are mainly due to the periodic change in the bend orientation, what leads to a periodically reversed centrifugal force and generates additional vortices, in contrast of helical (or toroidal) coils where the direction of the centrifugal forces, with regard to the flow direction, remains unchanged and the flow future is unperturbed.
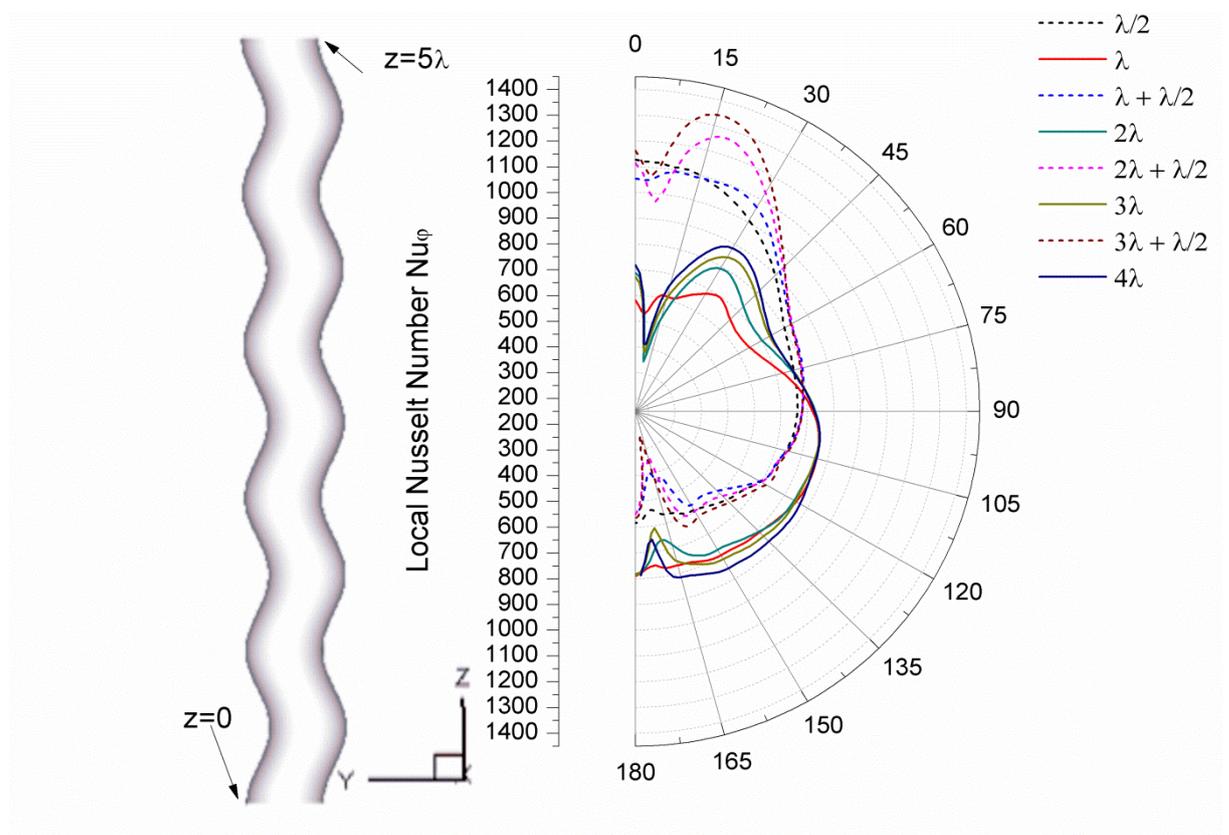

Figure 3.12 : Polar charts of the local Nusselt number at uppermost (solid lines) and bottommost (dashed lines) bends.

As shown too in Figure 3.12, a marginally higher rate of the heat transfer (dashed lines) is observed in the upper region of the bottommost bends. Due to the reversed direction of the centrifugal force, the cells rotate anti-clockwise; thus, the inverse thermal phenomenon is observed. From $\varphi = 180°$ to $\varphi = 0°$, the hot fluid in the lower region (see Figure 3.14(c)) is forced by the vortex against the pipe wall towards the upper region and cooled rapidly. In this direction, the inner wall temperature decreases (see Figure 3.14(b)). Thus, as well as the hot

fluid particles progress against the wall, the dimensionless temperature gradient increases especially the gradient would increase in a vertical asymptote manner from about $\varphi \simeq 75°$ at the limit of the upper surface which, does not receive any more the concentrated radiations from the parabolic reflector and only receives the direct radiation from the sun. The heat flux distribution is in the lowermost level, and so the wall-to-fluid temperature difference.

From Figure 3.14(c), at the lower region of bends, the convective transport promotes the heat transfer within the pipe and distorts the HTF temperature contours in contrast to the regular ones noticed in straight pipes [18] or corrugated pipes [16] where the convective transport in the radial direction is absent.
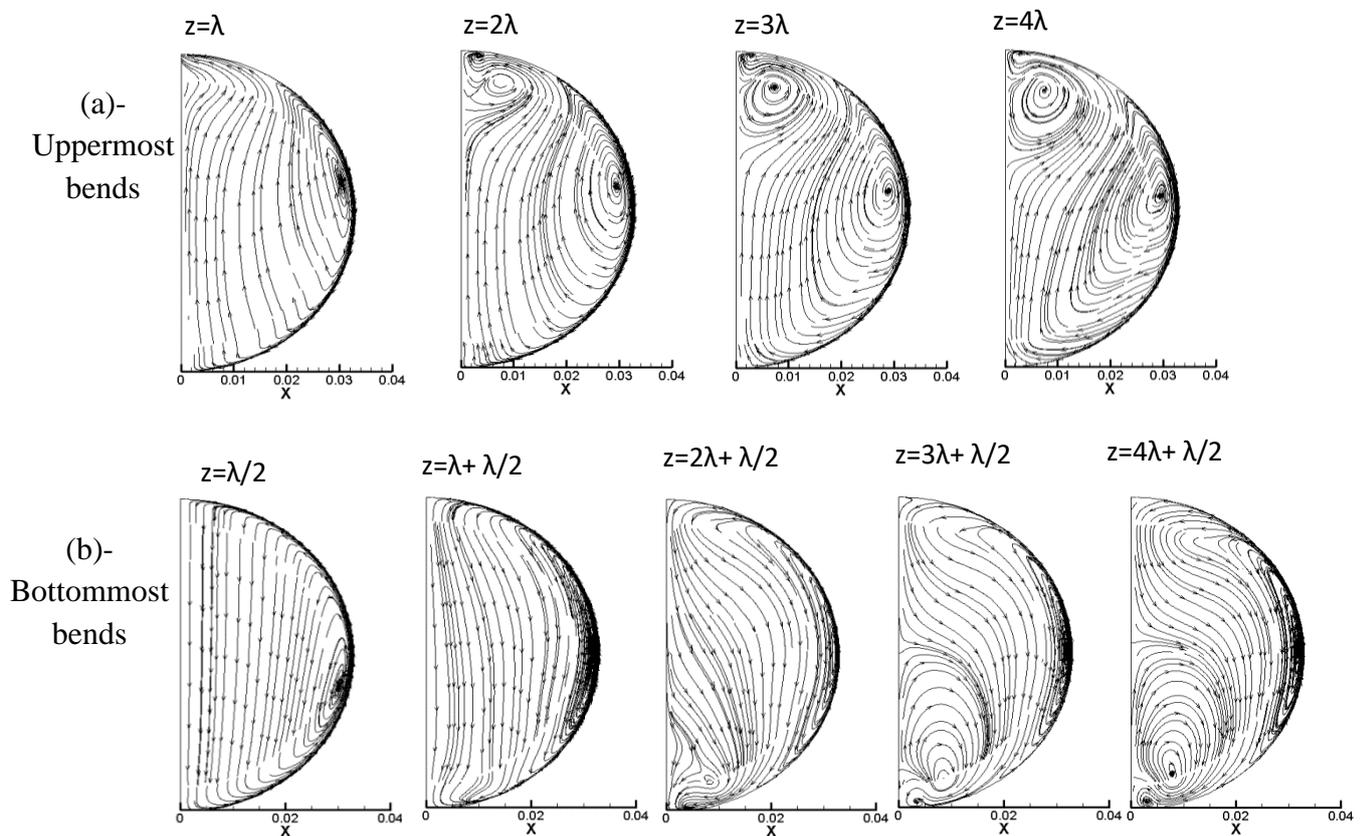

Figure 3.13 : Streamlines at various locations along a segment of the S-curved pipe, $\frac{\lambda}{2} \leq z \leq 4\lambda + \frac{\lambda}{2}$.
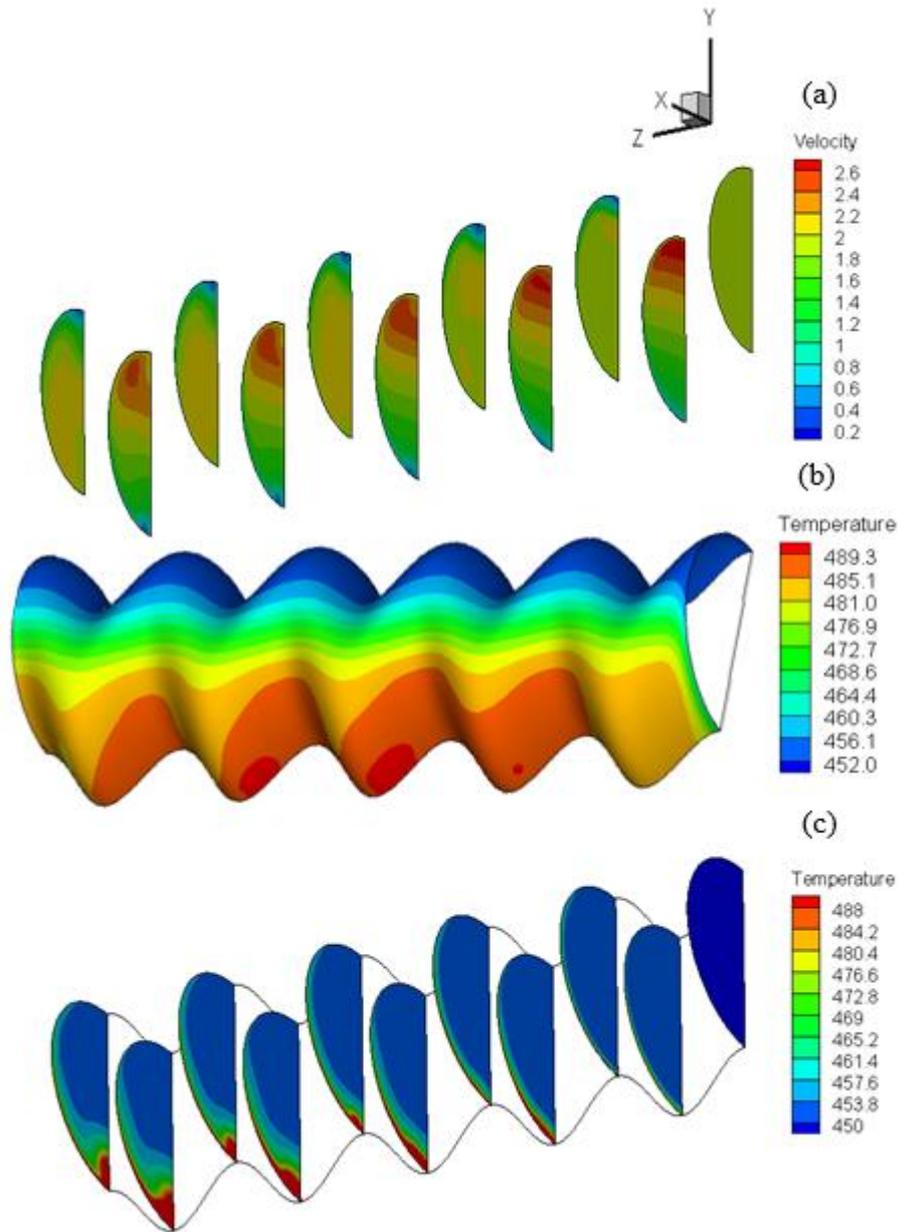
Figure 3.14 : Contours on the novel absorber for $T_{in} = 450\ K$ and $\dot{m}_{in} = 5\ kgs^{-1}$ (a) HTF velocity contours on bends xy-plane, (b) Temperature contours of the pipe inner-wall and (c) HTF temperature contours at bends xy-plane.

To show the longitudinal variation of the local Nusselt number along the absorber pipe, curved generatrices are extracted from the computational domain, as shown in Figure 3.15.

Figure 3.16 presents trends of the local Nusselt number for the same conditions as previously, i.e., $T_{in} = 450\ K$ and $\dot{m}_{in} = 5\ kgs^{-1}$. From Figure 3.16, all curves of the local Nusselt number possess a waved shape with a variable phase shift reaching 180°. To provide clear

explanations, the following comments relate to the first half of a periodic segment; it was noticed that:

- At $\varphi = 0°$, the distribution of **q** is uniform along the generatrix as showed by Figure 3.17, which is another way of representing **q**, it's more illustrative than it's in the Figure 2.6. As the velocity magnitude increases, the heat transfer and the local Nusselt number rise until a location in the vicinity of the uppermost bends where it starts decreasing in the same manner as the velocity magnitude. At $\varphi = 0°$, the location of the generatrix will be near the free streaming, slightly far-off from the vortex.

- At $\varphi = 30°$, the distribution of **q** is also uniform along the generatrix. The effects of the vortex arise and the peak local Nusselt number is observed.

- At $\varphi = 60°$, the same observations as previously, but less important.

- At $\varphi = 90°$, the local Nusselt number keeps the same shape with reduced effectiveness despite the increased of **q** along the generatrix (see Figure 3.17); the dynamic of the fluid predominates the local heat transfer more than the magnitude of **q**. The phase shift is about $\simeq 90°$ with regard to the first one.

- At $\varphi = 120°$, $\varphi = 150°$ and $\varphi = 180°$, the magnitude of **q** decreases along the generatrices. Despite the increased velocity magnitude, the local heat transfer predominated by the decreased **q**, decreases. The shape of Nu_φ is reversed, with the maximum phase shift $\simeq 180°$.
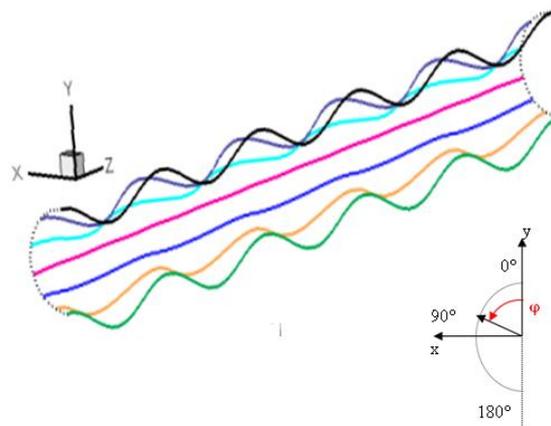

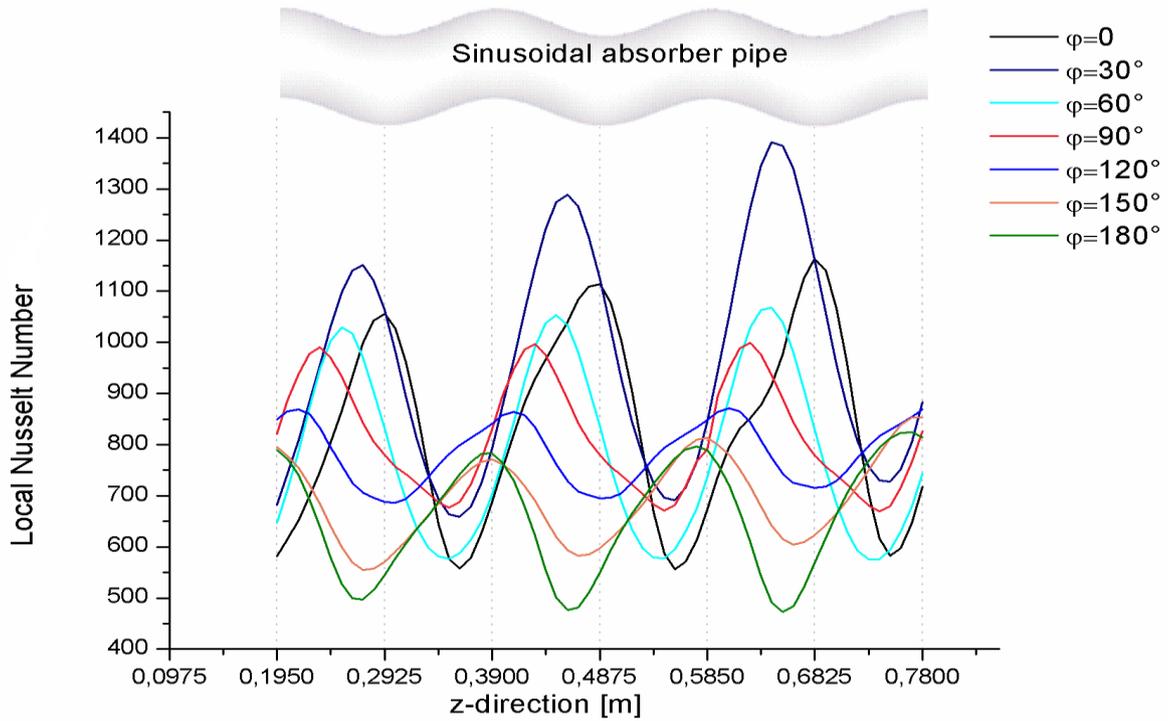Figure 3.15 : Curved shape of the generatrices at various azimuthal angles φ.

Figure 3.16 : Change of the local Nusselt number along generatrix at various azimuthal angles. Colours correspond to those adopted in Figure 3.17 for the curved generatrices.
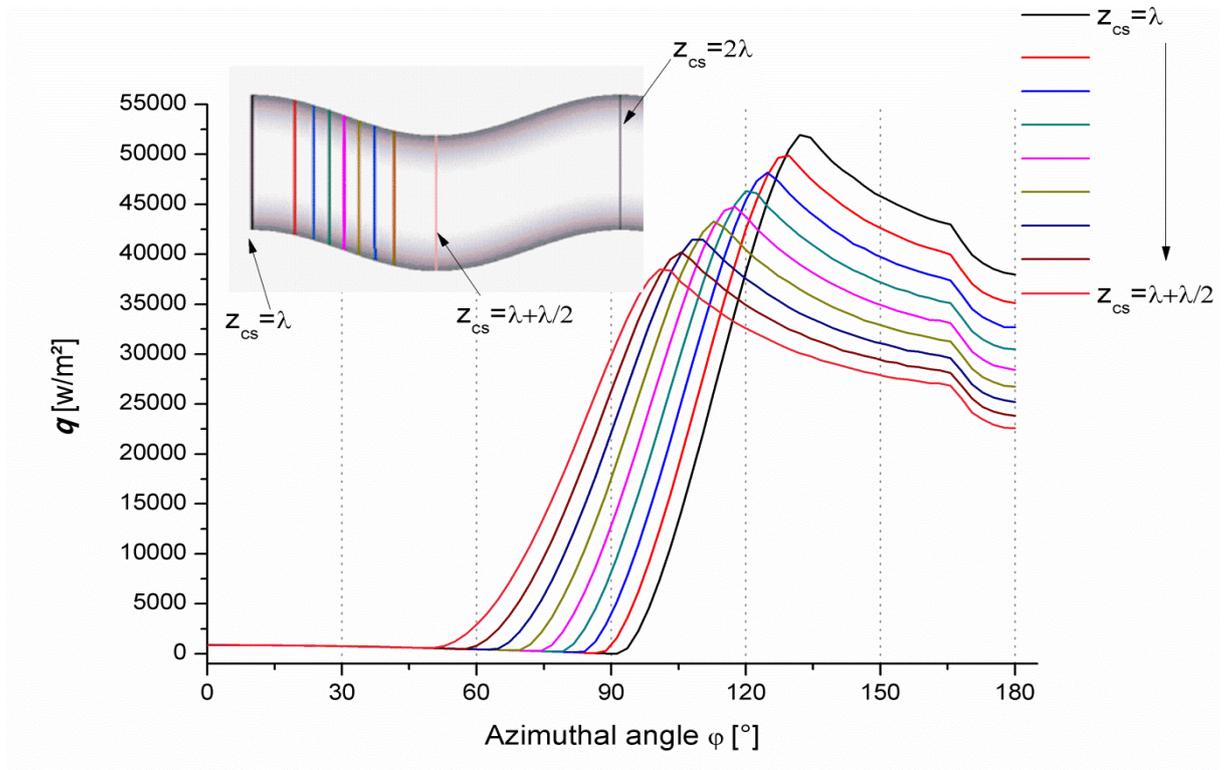

Figure 3.17 : The heat flux distribution against the azimuthal angle of the first half of a periodic segment.

3.5. The normalized mean Nusselt number

The normalised mean Nusselt number Nu^* (see Figure 3.18) was suggested by **Bail et al. [19]** as the ratio of the mean circumferential Nusselt number $\overline{Nu_\varphi}$ to the mean Nusselt number Nu of Figure 3.3 and takes the form,

$$Nu^* = \frac{1}{Nu}\left(\overline{Nu_\varphi}\right) = \frac{1}{Nu}\left(\frac{\int_0^\pi Nu_\varphi d\varphi}{\int_0^\pi d\varphi}\right) \tag{3.7}$$

Bail et al. [19] used the same normalised number in the experimental study of the heat transfer enhancement within a horizontally oriented helical coil, where the mean Nusselt number was estimated by the correlation (3.4) with reference to the work of **Rogers and Mayhew [5]**.
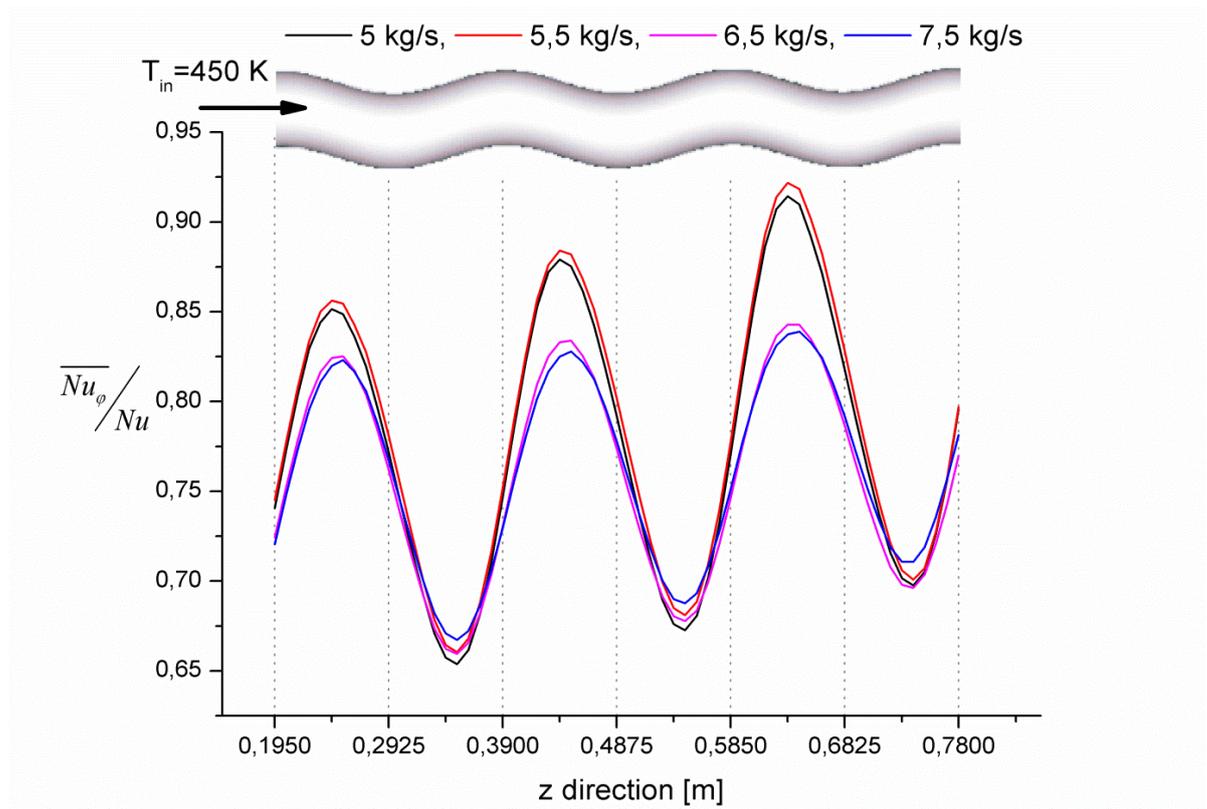

Figure 3.18 : The normalised mean Nusselt number $\overline{Nu_\varphi}\big/Nu$ along the pipe $\left(\lambda \leq z \leq 4\lambda\right)$ for $T_{in} = 450\ K$ and for various mass flow rates, which correspond to $\mathrm{Re} \simeq 64736$, $\mathrm{Re} \simeq 71210$, $\mathrm{Re} \simeq 84160$ and $\mathrm{Re} \simeq 97100$.

As shown in Figure 3.18, the general trend of curves is similar, while varying the mass flow rates, which corresponding to $\mathrm{Re} \simeq 64736$, $\mathrm{Re} \simeq 71210$, $\mathrm{Re} \simeq 84160$ and $\mathrm{Re} \simeq 97100$; nevertheless with regard to their magnitude, curves are separated into two distinct groups, the upper and lower ones. To explain these dissimilarities Figure 3.3 should be reconsidered. It is noticed from Figure 3.3 that the selected mass flow rates (Reynolds number) for illustration in Figure 3.18 are before and after the flow regime where the friction factor f increases suddenly. The jump of f was explained previously in section 3.3 and accounted for the emergence of newly vortices as the flow regime overtakes $\mathrm{Re} \simeq 71210$ (see Figure 3.7). Thus, from $\mathrm{Re} \simeq 84160$ a different flow configuration is characterised by a higher friction factor f (see Figure 3.3) as well as a jump in the normalised mean Nusselt number, despite these facts, the mean Nusselt number keeps the same slope (Figure 3.3).

In the lower branches, somehow, all curves come together while they were separated earlier, regardless the downward (accelerated) or upward (decelerated) flow. As discussed a few lines back, in the lower part of the pipe where the outer heat flux is intensified, the convective heat transfer is predominated by the heat flux density distribution than the fluid dynamics, in spite of the accelerated or decelerated flow. With regard to the local and mean Nusselt number magnitude, more uniform heat flux density distribution is wished.

Conclusions

Over studied range of Reynolds and working temperature, performed models have been successfully validated for both S-curved tube laboratory scale and the novel PTC S-curved collector. In fact, for the global grid of 3,297,000 cells where the Nusselt and the friction were not affected by the refinement, the maximum error between present friction factor and the experimental correlation by **Abou-Arab et al. [3]** is less than 3.9%. Whereas, the obtained Nusselt showed a maximum error of 5.2% against the correlation by **Rogers and Mayhew [5]**.

For the case of an inlet temperature of 450 K, the improvement in the Nusselt number for S-curved absorber compared to conventional straight tube is up to 63% with a pressure penalty of 40.8%, this for Reynolds ranges from 2.5×10^4 to 12.3×10^4 and Syltherm 800 as working fluid with Pr =26.5.

The raise of vortices induced mainly by a secondary flow due to the imbalance between the pressure force and centrifugal force generated by bends of the pipe is well predicted. The inlet temperature does not affect much the density of vortices neither their distribution, they related to the geometry rather than other working parameters except the Reynolds number which affects considerably the pressure drop.

At bends where the vortices are intense, the heat transfer is well stimulated then the HTF bulk temperature increases as a result, the velocity at bends must increase to make up lost velocity at the centre of the stream and ultimately satisfying the conservation of the mass.

The azimuthal temperature difference decreases from 50 K corresponding inlet temperature of 450 K for mass flow rates less than $\dot{m} = 3.5 \ kgs^{-1}$ to less than 35 K as the flow rate goes beyond.

The local Nusselt in the bottommost bends is higher than that in the uppermost bends mainly due to the ani-clockwise rotation of vortices at bottom half of the receiver as well as receiving higher concentrated radiations from the parabola.

The heat flux vs azimuthal angle of studied S-curved tube is constant for angles less than 90° for the uppermost section and angles less than 50° for the bottommost section. The heat flux increases from corresponding azimuthal angles of 50° (for bottommost section) and 90° (for uppermost section) to reach its maximum at almost 100° (for bottommost section) and 130° (for uppermost section), then the heat flux decreases until 165° for both bottommost and uppermost sections, finally the heat flux keeps decreasing until 180°. These cases represent the four regions of azimuthal heat flux distribution including direct radiation zone, heat flux increasing zone, heat flux decreasing zone and the shadow effect zone respectively.

The more the section location is away from the focal line, the more the heat flux density decreases. The uppermost sections located at the focal line intercept more reflected rays thus receiving higher heat flux, whereas the bottommost sections intercept less reflected rays thus receiving lesser heat flux.

References

[1] Syltherm 800 Heat Transfer Fluid, Product Technical Data, the Dow Chemical Company, Midland, MI., DOW, 1997.

[2] Y.L. He, J. Xiao, Z.D. Cheng, Y.B. Tao, A MCRT and FVM coupled simulation method for energy conversion process in parabolic trough solar collector, Renew Energy 36 (2011) 976–985.

[3] T.W. Abou-Arab, T.K. Aldoss, A. Mansour, Pressure drop in alternating curved tubes, Applied Scientific Research 48 (1991) 1-9.

[4] R. Yang, F.P. Chiang, An experimental heat transfer study for periodically varying-curvature curved-pipe, Int. J. Heat Mass Transfer 45 (2002) 3199–3204.

[5] G.F.C. Rogers, Y.R. Mayhew, Heat transfer and pressure loss in helically coiled tubes with turbulent flow, Int. J. Heat Mass Transfer 7 (1964) 1207-1216.

[6] F.P. Incropera, D.P. Dewitt, T.L. Bergman, A.S. Lavine, Fundamentals of Heat and Mass Transfer. Sixth edition, J. Wiley & Sons, Hoboken NJ, 2007 997 pp.

[7] J. Eustice, Experiments of streamline motion in curved pipes, Proc. R. Soc. London A85 (1911) 119–131.

[8] S. Srinivasan, S. Nadapurkar, F.A. Holland, Friction factors for coils, Trans. Inst. Chem. Eng. 48 (1970) 156–161.

[9] H. Ito, Friction factors for turbulent flow in curved pipes, J. Basic Engineering 81 (1959) 123–134.

 [10] S. Vashisth, V. Kumar, and K. D. P. Nigam, A Review on the Potential Applications of Curved Geometries in Process Industry, Ind. Eng. Chem. Res. 47 (2008) 3291-3337.

[11] I. Di Piazza, M. Ciofalo, Numerical prediction of turbulent flow and heat transfer in helically coiled pipes, Int. J. Therm. Sci. 49 (2010) 653–663.

[12] F.R. Menter, Two-equation eddy-viscosity turbulence models for engineering applications, AIAA J. 32 (1994) 269–289.

[13] ANSYS CFX Release 11 User Manual

[14] R. Yang, S.F. Chian, W. Wu, Flow and heat transfer in a curved pipe with periodically varying curvature, Int. Commun. Heat Mass Transfer 27 (2000) 133–143.

[15] N.R. Rosaguti, D.F. Fletcher, B.S. Haynes, Low-Reynolds number heat transfer enhancement in sinusoidal channels, Chemical Engineering Science 62 (2007) 694-702.

[16] W. Fuqiang, L. Qingzhi, H. Huaizhi, T. Jianyu, Parabolic trough receiver with corrugated tube for improving heat transfer and thermal deformation characteristics, Applied Energy 164 (2016) 411–424.

[17] M. Di Liberto, M. Ciofalo, A study of turbulent heat transfer in curved pipes by numerical simulation, Int. J. Heat Mass Transfer 59 (2013) 112–125.

[18] Y. Wang, Q. Liu, J. Lei, H. Jin, Performance analysis of a parabolic trough solar collector with non-uniform solar flux conditions, Int. J. Heat Mass Tran. 82 (2015) 236–249.

[19] B. Bai, L. Guo, Z. Feng, X. Chen, Turbulent heat transfer in a horizontally coiled tube, Heat Transfer-Asian Research 28 (5) (1999) 395–403.

Chapter 4:Parabolic Trough Plant Optimization

Introduction

In this chapter a dimensional analysis and similarity considerations are discussed in order to find out the benefit of the novel PTC S-curved tube in terms of performance compared to conventional straight tube. The constitution of dimensional analysis quantifying the heat transfer rate between the inner wall of the absorber and the HTF to that transported by the HTF as useful heat, it is possible under the same operating condition and for the same useful heat output to estimate the length ratio of the novel S-curved tube. The pressure drop also is estimated for both tubes to establish the in-between relationship.

The combination of the pressure drop penalty and the heat transfer gain of the novel S-curved tube with regard to CSST is evaluated using the Performance Evaluation Criteria (PEC). In addition, Overall remarks on the novel absorber and its advantages are mentioned. Finally, a global comparison between the conventional SEGS LS-2 plant and its future model by replacing the conventional HCE with the novel S-curved HCE in terms of size reduction is highlighted.

4.1. Dimensional analysis and Similarity considerations

It would be very interesting to be able to quantify the benefits and impacts of the newly designed S-curved absorber pipe on the sizes of the solar receiver, the solar module and the solar field; this can be obtained through a dimensional analysis.

The mean heat transfer rate Q throughout the pipe can be defined as,

$$Q = \dot{m}_{in} \bar{c}_p (\bar{T}_{out} - \bar{T}_{in})$$
(4.1)

$\dot{m}_{in} = \rho u_{in} S_{CS}$ Being the mass flow rate through the inlet cross-section $S_{CS} = \pi D_i^2 / 4$

On the other hand, assuming steady-state conditions, the inner convective heat transfer can be expressed as follows,

$$Q = hA(\bar{T}_w - T_{mf})$$
(4.2)

$A = \pi D_i L$ Being the inner exchange area of the pipe where L is its equivalent length.

The ratio of equations resulting from the expression (4.1) when it is applied to the first configuration (subscript 1) and to the second configuration (subscript 2) leads to,

$$\frac{Q_1}{Q_2} = \frac{(\rho u_{in} \bar{c}_P)_1}{(\rho u_{in} \bar{c}_P)_2} \frac{(\bar{T}_{out} - \bar{T}_{in})_1}{(\bar{T}_{out} - \bar{T}_{in})_2} \left(\frac{(D_i)_1}{(D_i)_2} \right)^2$$
(4.3)

Similarly, using the equation (4.2),

$$\frac{Q_1}{Q_2} = \frac{(h)_1}{(h)_2} \frac{(\bar{T}_w - \bar{T}_{mf})_1}{(\bar{T}_w - \bar{T}_{mf})_2} \left(\frac{(D_i)_1}{(D_i)_2} \right) \left(\frac{L_1}{L_2} \right)$$
(4.4)

The expressions (4.3) and (4.4) may be combined to remove the term $\dfrac{Q_1}{Q_2}$; rearranged, we obtain:

$$\left(\frac{L_2}{L_1} \right) = \frac{\left(\rho u_{in} \bar{c}_P \middle/ h \right)_2}{\left(\rho u_{in} \bar{c}_P \middle/ h \right)_1} \frac{(\bar{T}_{out} - \bar{T}_{in})_2}{(\bar{T}_{out} - \bar{T}_{in})_1} \frac{(\bar{T}_w - \bar{T}_{mf})_1}{(\bar{T}_w - \bar{T}_{mf})_2} \frac{(D_i)_2}{(D_i)_1}$$
(4.5)

Assuming $\theta = (\bar{T}_{out} - \bar{T}_{in})$ and $\theta_w = (\bar{T}_w - \bar{T}_{mf})$, it follows that

$$\frac{L_2}{L_1} = \frac{St_1}{St_2} \frac{\theta_2}{\theta_1} \frac{(\theta_w)_1}{(\theta_w)_2} \frac{(D_i)_2}{(D_i)_1}$$
(4.6)

$St = h \middle/ \rho u_{in} \bar{c}_P$ being the Stanton number.

According to the second formula of the Stanton number, $St = Nu \middle/ \text{Re} \, \text{Pr}$, equation (4.6) becomes:

$$\frac{L_2}{L_1} = \frac{(D_i)_2}{(D_i)_1} \frac{\left(Nu \middle/ \text{Re} \, \text{Pr} \right)_1}{\left(Nu \middle/ \text{Re} \, \text{Pr} \right)_2} \frac{\theta_2}{\theta_1} \frac{(\theta_w)_1}{(\theta_w)_2}$$
(4.7)

This result is very useful; it suggests that the proportional heat transfer rate between two different exchangers may be converted to equality by introducing dimensionless groups that are a measure of the phenomena behavior. For many applications, it is convenient to evaluate the HTF properties at the inlet temperature.

Introducing the aspect ratio, defined as $\dfrac{L}{D}$, another useful form of the expression (4.7) can be reached,

$$\left(\frac{L}{D_i}\right)_1 \left(Nu\Big/\mathrm{Re}\,\mathrm{Pr}\right)_1 \left(\frac{\theta_w}{\theta}\right)_1 = \left(\frac{L}{D_i}\right)_2 \left(Nu\Big/\mathrm{Re}\,\mathrm{Pr}\right)_2 \left(\frac{\theta_w}{\theta}\right)_2 \tag{4.8}$$

Such a method will have general utility in developing comparison between exchangers, as well as addressing immediate questions concerning the reduction of sizes, performances and the comparison between various HTF.

4.1.1. The possible reduction of the absorber size

In the focus of the current study, exchangers would be the conventional absorber with a straight pipe and the newly designed with a longitudinally S-curved one, referenced to subscripts 1 and 2 respectively.

The immediate question is what would be the size of the S-curved absorber to reach similar rise of the HTF temperature for both absorbers, i.e. $\left(\dfrac{\theta_{S-curved\ pipe}}{\theta_{straight\ pipe}} = 1\right)$, when considering: similar HTF inlet temperature, i.e. $\left(\dfrac{\mathrm{Pr}_{S-curved\ pipe}}{\mathrm{Pr}_{straight\ pipe}} = 1\right)$ and an even flow regime, i.e. $\left(\dfrac{\mathrm{Re}_{S-curved\ pipe}}{\mathrm{Re}_{straight\ pipe}} = 1\right)$, the equation (4.7) is reduced to,

$$\frac{L_2}{L_1} = \frac{(D_i)_{S-curved\ pipe}}{(D_i)_{straight\ pipe}} \frac{(Nu_i)_{straight\ pipe}}{(Nu_i)_{S-curved\ pipe}} \frac{(\theta_w)_{straight\ pipe}}{(\theta_w)_{S-curved\ pipe}} \tag{4.9}$$

As $Nu = hD_i\Big/\lambda$, equation (4.9) becomes,

$$\frac{L_2}{L_1} = \frac{h_{straight\ pipe}}{h_{S-curved\ pipe}} \frac{(\theta_w)_{straight\ pipe}}{(\theta_w)_{S-curved\ pipe}} \qquad (4.10)$$

Assuming similar wall to fluid temperature difference, i.e. $(\theta_w)_{S-curved\ pipe} = (\theta_w)_{straight\ pipe}$, and as discussed in the previous subsections $h_{S-curved\ pipe}$ should be higher than $h_{straight\ pipe}$ the equation (4.10) becomes,

$$\frac{L_2}{L_1} = \frac{h_{straight\ pipe}}{h_{S-curved\ pipe}} < 1 \qquad (4.11)$$

The equation (4.11) can give a measure of the length that would the novel receiver have to absorb an amount of useful energy similar to that absorbed by the straight receiver under operating conditions mentioned earlier. Using the equation (4.11) and previous results of Figure 3.3 the potential change in the S-curved absorber length, while varying the Reynolds number, at $\overline{T}_{in} = 450K$ is illustrated in Figure 4.1. Until $\mathrm{Re} \simeq 71000$ the trend is increasing from $\frac{L_2}{L_1} \simeq 0.61\ to \simeq 0.705$; from this location it decreases and becomes relatively flat, about 0.69.

To achieve the same HTF temperature increase for the classic straight absorber, the length of the novel absorber (L_2) will be significantly reduced, consequence of the heat transfer improvement. With a mean length of $L_2 \simeq 69\% L_1$, the size of the solar collector field should be reduced about 31%.

Another question could arise from the previous analysis: What would be the diameter of the S-curved pipe assuming the similar HTF temperature rise θ, the same HTF inlet temperature, the similar length and the same mass flow rate.

To answer this question, it is preferable to use the equation (4.5) instead of the equation (4.7). considering previous assumptions, it becomes,

$$\frac{\left(u_{in}/h\right)_{S-curved\ pipe}}{\left(u_{in}/h\right)_{straight\ pipe}}\frac{(\theta_w)_{straight\ pipe}}{(\theta_w)_{S-curved\ pipe}}\frac{(D_i)_{S-curved\ pipe}}{(D_i)_{straight\ pipe}}=1 \tag{4.12}$$

For more convenience, the wall temperature difference is assumed to be similar, thus

$\dfrac{(\theta_w)_{straight\ pipe}}{(\theta_w)_{S-curved\ pipe}}=1$ and the velocity is replaced by $u_{in}=\dfrac{4\dot{m}_{in}}{\rho\pi D_i^2}$. As the mass flow rate $\dot{m}_{in}$

being unchanged, the equation (4.12) is simplified as,

$$\frac{(D_i)_{S-curved\ pipe}}{(D_i)_{straight\ pipe}}=\frac{h_{straight\ pipe}}{h_{S-curved\ pipe}} \tag{4.13}$$
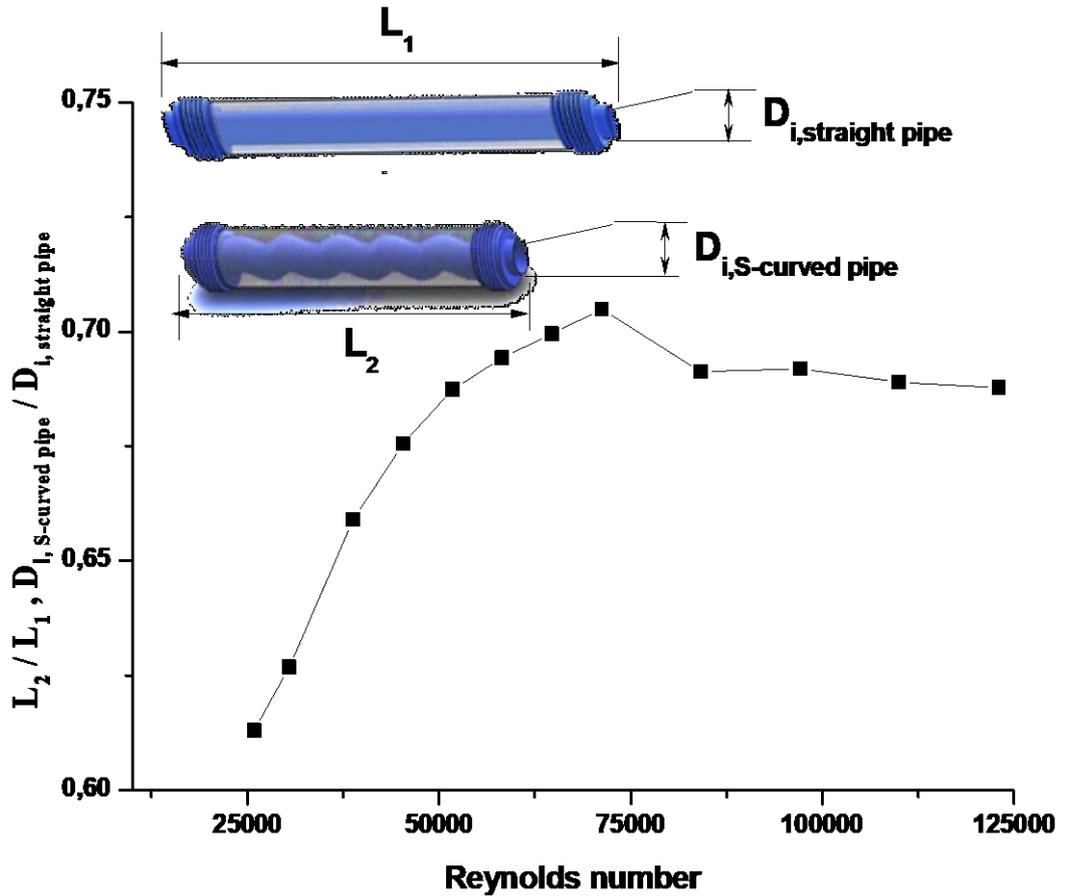

Figure 4.1 : The reduction of the solar absorber size.

The result is similar to equation (4.11) and the trend against the Reynolds number would

be similar, as showing in Figure 4.1. To achieve the same HTF temperature increase of the

classic straight absorber, while taking the same length of the novel absorber, its diameter should be diminished. Under cited assumptions, the mean reduction of the receiver diameter should be about 31%.

It is also important to specify that the S-curved absorber length L_2 is identified as the arc length of the sinusoidal pipe; which means that its equivalent straight length should be slightly lesser due to the curvature.

4.1.2. The re-balancing of the pressure drop

The increase of the pressure drop penalty of the novel solar absorber pipe, discussed in the previous subsections as illustrated in Figure 3.3, should be re-balanced by the reduction of its length. To strengthen this statement, it is better to use the pressure drop $\left(-\Delta P\right)$ rather than the friction factor f. Depending on the Darcy-Moody friction factor [1], the drop of the pressure through the S-curved pipe, considering the friction factor f of Figure 3.3, is written as,

$$\left(-\Delta P\right)^{L_1}_{S-curved} = f \cdot \left(\rho u_{in}^2 \Big/ 2\right)\left(L_1 \Big/ \left(D_i\right)_1\right) \tag{4.14a}$$

As the friction factor is independent to the length, multiplying and dividing the right-hand side of the equation (4.14a) by L_2 it becomes (rearranged form),

$$\left(-\Delta P\right)^{L_1}_{S-curved} = f \cdot \left(\rho u_{in}^2 \Big/ 2\right)\left(L_2 \Big/ \left(D_i\right)_1\right)\left(L_1 \Big/ L_2\right) = \left(-\Delta P\right)^{L_2}_{S-curved}\left(L_1 \Big/ L_2\right) \tag{4.14b}$$

Thus,

$$-\Delta P\big|^{L_1}_{S-curved} = -\Delta P\big|^{L_2}_{S-curved} \cdot \left(L_1 \Big/ L_2\right) \tag{4.15}$$

Taking into account the size reduction of the novel absorber, the pressure drop penalty throughout the S-curved pipe $\left(-\Delta P\big|^{L_1}_{S-curved}\right)$, computed by the equation (4.14a) using data from Figure 3.3 for the length L_1, the pipe should be reconsidered taking into account its reduced length. The pressure drop is re-balanced by the reduction of the size and decreases as shown

in Figure 4.2. As assumed earlier, the pressure drops of the S/curved pipe (with the reduced length L_2) and the straight pipe (with the straight length L_1) are similar.
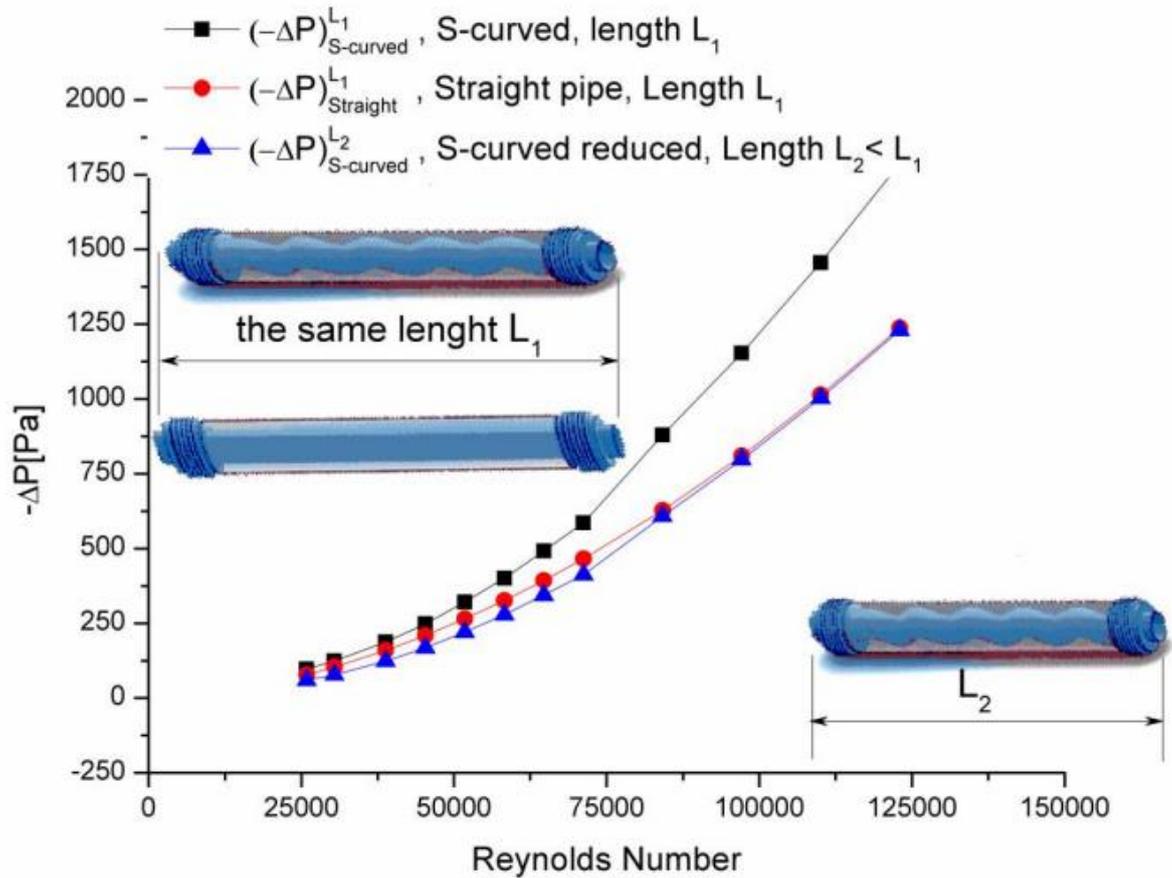

Figure 4.2 : The similitude of the pressure drops through absorbers and the effect of the size reduction on the S-curved absorber.

Although, the preceding discussion and analysis were limited to the particular case of the present study but they can provide ways and means for rapid and exploratory analysis for many other types of exchangers.

4.2. Performance analysis

For a better evaluation of the novel S-curved absorber performances, it is appropriate to evaluate the performance evaluation criteria (PEC) as defined in **[2]**.

The heat transfer enhancement is defined as,

$$E_{Nu} = {Nu_{S-curved}}\Big/{Nu_{straight}}$$
(4.16)

$Nu_{S-curved}$ and $Nu_{straight}$ being the mean Nusselt numbers for the S-curved pipe and the straight pipe, respectively.

The relative pressure-drop penalty incurred for an S-curved pipe, of equal path length and diameter with a straight pipe, is given by,

$$E_f = f_{S-curved} \Big/ f_{straight} \tag{4.17}$$

Combining these two dimensionless numbers as,

$$PEC = \frac{Nu_{S-curved} \Big/ Nu_{straight}}{\left(f_{S-curved} \Big/ f_{straight} \right)^{1/3}} \tag{4.18}$$

Leads to the performance evaluation criteria (PEC) at given pumping power as defined by **Webb [2]**. The mean heat transfer enhancement, the pressure-drop penalty and the PEC plots against the Reynolds numbers are shown in Figure 4.3. The PEC reaches a maximum of 135%, it decreases while Re increases and becomes almost uniform after $\mathrm{Re} \simeq 84160$. This result is consistent with the flow behavior observed at $\mathrm{Re} \simeq 84160$ where the flow becomes established without the apparition of new vortices.
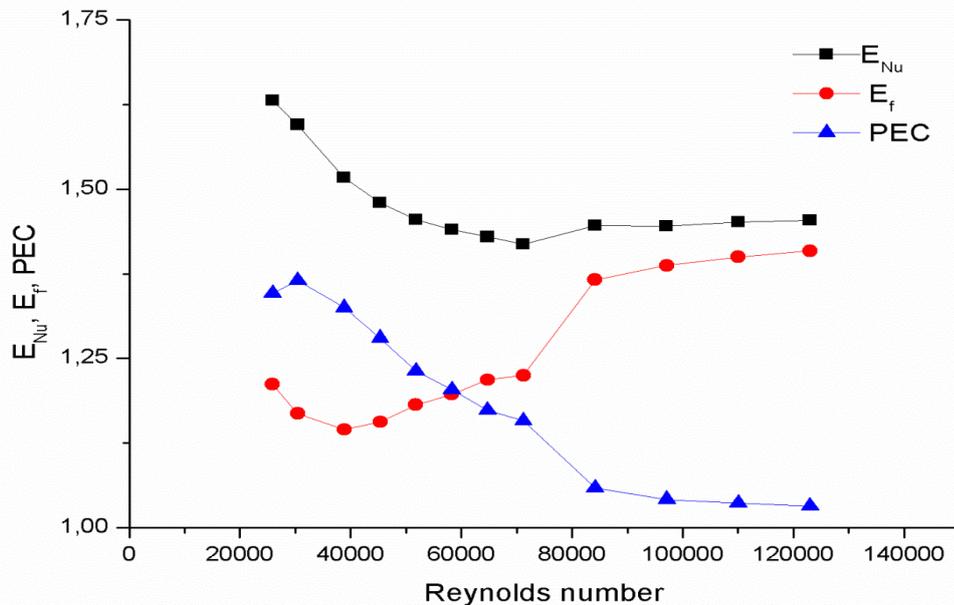

Figure 4.3 : The mean heat transfer enhancement, the pressure-drop penalty and the PEC of PTC S-curved absorber against the Reynolds number at $T_{in} = 450\,K$.

The heat transfer performance factor as defined by **Fuqiang et al. [3]** would be $\left(PEC \right)^3$, and thus, it would be 246% for the S-curved absorber while **[3]** had quoted a value of 148% for the asymmetric outward convex corrugated tube, the difference is obvious.

4.3. Advantages and remarks on the novel PTC sinusoidal absorber tube

- Curved pipes are present in numerous engineering applications and used as a heat exchangers and steam generators in power plants, mainly because of the heat transfer enhancement due to the induced secondary flow. Exploiting these phenomena in the concentrated solar energy, a longitudinally S-curved/sinusoidal pipe is proposed. Contrary to the other heat transfer enhancement techniques, the new absorber does not include any supplemental device such perforated plates or vortex generators or others. At this time, as a consequence of the PTC straight line focus, only straight absorbers are used.

- The S-curved/ sinusoidal pipes could be possibly arranged with straight pipes which would constitute another configuration named by **Demagh [4]** combined "S/straight" absorber.

- The S-curved shapes are characterised by limited peak-to-peak amplitude and a periodic length λ which can vary along the pipe.

- The new receivers are so simply designed that they could replace the classic receivers without bringing any modification on the metallic structure of operational solar collectors.

- Any closed curve shape could constitute a possible cross-section of the pipe, but circular, oval or a portion of these two sections is preferred (example: half-circular, 1/3 circular, 1/2 oval…).

4.4. Parabolic trough plant optimization

A total of 4670 LS-2 SCAs (1.097 x 10^6 m2) are currently installed in several SEGS, each complete SEGS LS-2 solar collector assembly (SCA) module consists of 12 HCE of 4 m length. The size of each module is about 47.1 m x 5 m **[5]**. A thermal strain restrain that would be obtained by installing the novel absorber tube instead of a conventional straight smooth tube

CSST receiver should be quantified to estimate the maintenance cost reduction as well as the lifetime of the HCE. In present study, just the thermal efficiency improvement will be considered to estimate the SEGS plant size reduction.

As discussed in the section 4.1.1, the size of the solar collector field should be reduced about 31%, for cited example, the novel S-curved SEGS LS-2 HCE would be 4 m length and the SCA module size would be 47.1 m x 5 m. The novel SEGS S-curved plant equivalent of 4670 SCA CSST (1.097×10^6 m^2) would have only 3223 S-curved SCAs (773352 m^2) to produce the same thermal output.

Conclusions

Through established similitude relation between the novel S-curved tube and CSST in terms of heat transfer rate, it's found under considered assumptions and operating conditions that the novel S-curved tube length could be reduced by 31%. The heat transfer enhancement of the novel S-curved tube accompanied also by the pressure drop increase relatively to CSST, but in general the PEC showed a great improvement in thermal efficiency for the novel S-curved tube.

The possible reduction of the typical SEGS LS2 plant has been investigated, the absence of detailed study taking into account the thermo-mechanical analysis, although curved tubes can resist better for thermal stress and mechanical deformation basically due to reduced circumferential temperature. The effective cost of the novel PTC S-curved tube and its lifetime as well as the absence of experimental work on the novel PTC S-curved tube, thus, based on these factors and others, made estimation for the plant size reduction by replacing the CSST with the S-curved tube rely only on the thermal efficiency improvement obtained by simulation.

The future PTC S-curved plant with only 3223 S-curved SCAs (773352 m^2) could replace the conventional SEGS LS2 plant with 4670 SCA CSST (1.097×10^6 m^2) and produce the same output thermal energy.

References

[1] F.P. Incropera, D.P. Dewitt, T.L. Bergman, A.S. Lavine, Fundamentals of Heat and Mass Transfer. Sixth edition, J. Wiley & Sons, Hoboken NJ, 2007 997 pp.

[2] R. L. Webb, Performance evaluation criteria for use of enhanced heat transfer surfaces in heat exchanger design, Int. J. Heat Mass Transfer 24 (1981) 715–26.

[3] W. Fuqiang, T. Zhexiang , G. Xiangtao, T. Jianyu, H. Huaizhi, L. Bingxi, Heat transfer performance enhancement and thermal strain restrain of tube receiver for parabolic trough solar collector by using asymmetric outward convex corrugated tube, Energy 114 (2016) 275-292.

[4] Y. Demagh, Absorbeur d'énergie muni d'un tube possédant des formes courbées en "S" à usage dans les collecteurs solaires, https://patentscope.wipo.int. WO/2016/124207. 2016 August 11.

[5] V. Dudley, G. Kolb, M. Sloan, D. Kearney, SEGS LS2 solar collector-test results, Tech. Report of Sandia National Laboratories SANDIA-94-1884, 1994.

Conclusions and further work

This work is carried out to study the thermo-dynamic behavior through the novel PTC S-curved receiver tube. Obtained results are compared to those of CSST and the flowing conclusions may be drawn:

➢ In the range of studied parameters, the improvement in the Nusselt number for the S-curved absorber tube is about 63% with pressure drop of 40.8% relatively to CSST.

➢ The raise of vortices induced mainly by a secondary flow due to the imbalance between the pressure force and centrifugal force generated by bends of the pipe, these vortices are related to the geometry rather than other working parameters.

➢ The vortices improve the heat transfer rate; as a result, HTF bulk temperature in S-curved receiver is higher than that in the CSST.

➢ The circumferential temperature gradient in the novel tube is reduced considerably compared to CSST; in fact, the temperature gradient would be less than 35 K for flow rates beyond $\dot{m} = 5.5\ kgs^{-1}$.

➢ At the bottommost bends of S-curved tube where the flow is reversed against the stream motion and higher concentrated radiations, the Nusselt is higher than that in the uppermost bends.

➢ The azimuthal heat flux distribution is found to vary dramatically with the variation of azimuthal angle; the heat flux distribution presented four different regions.

➢ The local heat flux is decreasing as moving away from the uppermost sections, which are positioned in this study at the focal line.

➢ Under considered assumptions and operating conditions, the novel S-curved tube length could be reduced by 31%.

➢ Based on the above conclusion, the future PTC S-curved plant with only 3223 S-curved SCAs (773352 m^2) could replace the conventional SEGS LS2 plant with 4670 SCA CSST (1.097 x 10^6 m^2) and produce the same output thermal energy.

Further work

Based on the conclusions above, more work should be done on the following subjects:

- An experimental study should be done on the novel S-curved receiver therefore present models would be improved based on realistic data.
- Developing an optical model for PTC S-curved HCE.
- Two-phase model may also be interesting using water as heat transfer fluid.
- Investigate the effect of the focal line, rim angle and tube section form on the overall thermal efficiency of the novel receiver.
- Involve the cost-efficiency parameter for more reliable comparison between CSST and the novel S-curved tube.